10 Twin Screw and Twin Rotor Processing Equipment

We discussed the principles of melting mechanisms of twin screw extruders (TSEs) in Sections 5.1 and 5.9, and melt pumping in Section 6.8, where we also discussed basic TSE configurations and geometry. In this chapter, we discuss, and when possible analyze, the overall processing performance. We do this in a broader family of polymer processing equipment, which utilizes two power-transmitting elements such as screws or rotors[1] operating adjacent to each other and rotating in the same or opposite directions in a common barrel.

Most twin screw-based machines are in fact extruders, and perform the same elementary polymer processing steps as single screw extruders (SSEs). However, because of the unique *time-varying* screw-to-screw interactions that take place in them, which are absent in single screw-based machines, *additional* physical mechanisms emerge that primarily and particularly affect the elementary steps of *melting* and *mixing*. Due to these additional mechanisms, the twin-screw machines offer important advantages over single screw machines, enabling them to carry out the melting and mixing steps more efficiently and uniformly. Specifically, melting can take place in a manner involving the *entire mass* of the compressed particulates, which results in very rapid and uniform melting over a very short (1–2 *L/D*) axial length, and hence narrow residence time distribution (RTD) in the molten state.[2] Consequently, a large amount of mechanical energy is needed in this axial rotor section to provide for the enthalpy of heating and melting. Equally important, mixing in many TSEs benefits from the existence of *three-dimensional*, time-varying, extensional melt ''folding'' chaotic flows, generated by screw-to-screw interactions. The result is very fine and rapid dispersive mixing that, in the case of immiscible blends, is independent of the component viscosity ratio and rapid and uniform distributive mixing, requiring *less twin shaft mechanical energy* input, since extensional flow kinematics are very efficient for distributive mixing.

---

1. Most of these machines are based on two adjacent screws, but some, like the continuous mixers, have a different geometry, which is better defined as consisting of two rotors.

2. Recall that in the SSE, some of the polymer melts early in the extruder and some at the very end, and hence, the RTD in the molten state is rather broad.
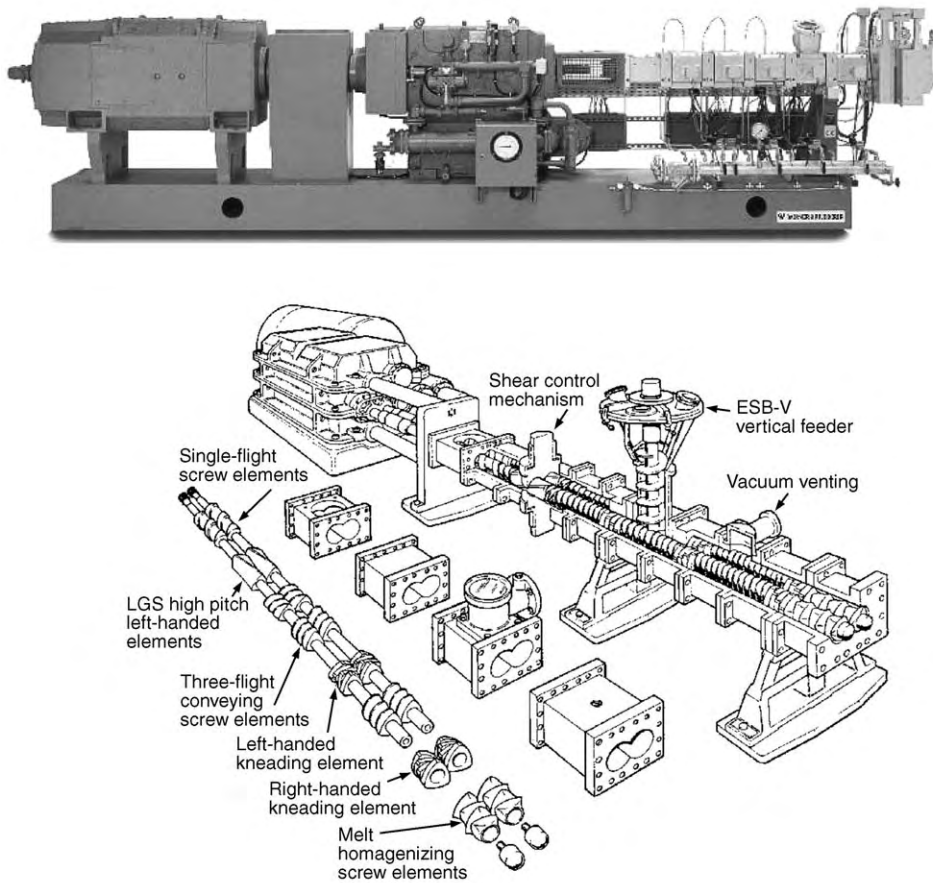

Principles of Polymer Processing, Second Edition, by Zehev Tadmor and Costas G. Gogos
Copyright © 2006 John Wiley & Sons, Inc.

Fig. 10.1 Photograph and schematic representation of the modular screw-element sequences and barrel sections of an intermeshing, co-rotating TSE. [Courtesy of Coperion Werner and Pfleiderer Corp.]

Typically, the TSE is custom designed to fit the process and product requirements by utilizing a wide array of interchangeable screw elements and screw element sequences "skewered" onto polygonal shafts. This capability, together with the wide use of segmented barrel sections, enables twin screw-based machines to specify or fit the location of any of the elementary steps, as well as the downstream introduction of additional component feed streams, or removal of volatiles at the needed locations. The versatility of screw and barrel design in twin screw–based machines is shown schematically in the exploded view of a common variant of such equipment, the intermeshing, co-rotating TSE, in Fig. 10.1

Customized and flexible screw-element and barrel segment designs, and fast and efficient melting and mixing (both dispersive and distributive) in most TSEs make such equipment very well suited and almost exclusively used for the following polymer processing operations:

- Very high rate postpolymerization reactor product melting and mixing with stabilizer additives in postpolymerization reactor "finishing" operations.

- Polymer compounding of multicomponent/two-phase polymer systems.
- Reactive polymer processing.

The first operation was briefly discussed in Chapter 5, and we expand on it in this chapter, while the last two polymer processing operations are discussed in more detail in Chapter 11.

10.1   TYPES OF TWIN SCREW AND TWIN ROTOR–BASED MACHINES

A wide variety of both *co-rotating* and *counterrotating* twin screw and twin rotor-based extruders are commercially available. White (1) described and discussed the historical evolution of the design and function of most of them. Herrmann et al. (2) presented the ''classic'' schematic representation of all the possible variants of co- and counterrotating extruders. Todd (3) presented a concise schematic representation, shown in Fig. 10.2, while Agassant et al. presented both a more complete classification, as well as the different types of flow channels in twin screw-based machines, as shown in Figs. 6.41. As indicated in this figure, the *degree* of intermesh in co-rotating devices can be designed to be *partial* or *full*, the latter leading to the *self-wiping* capability by the screw pair.

Tangential counterrotating machines are available in both matched (shown) and staggered screw flight configurations. Both designs create screw-to-screw interaction flows and material exchanges, and result in very good distributive mixers and polymer modification reactors (4). The *intermeshing, counterrotating TSE* is essentially a ''positive displacement'' device, where the material is conveyed downstream in confined, helical, C-shaped channels (5),
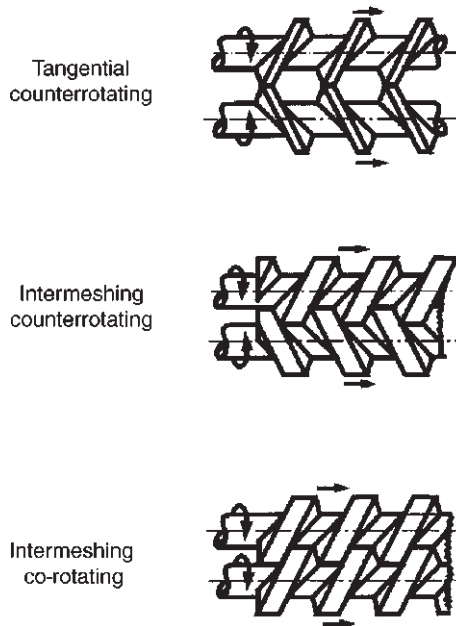

Tangential
counterrotating

Intermeshing
counterrotating

Intermeshing
co-rotating

Fig. 10.2   Classification of TSEs. [Reprinted by permission from D. B. Todd, ''Introduction to Compounding,'' in *Plastics Compounding—Equipment and Processing*, D. B. Todd, Ed., Hanser, Munich, 1998.]
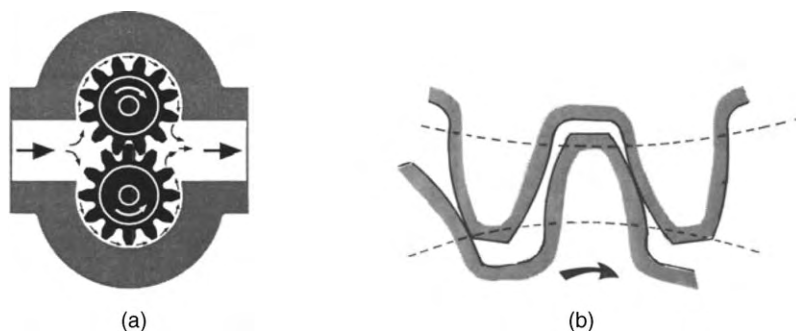
Fig. 10.3 Schematic representation of a gear pump. (a) Cross-sectional view [Reprinted by permission from D. Smith, P. Stoughton, C. Morgan, and G. Hovis, "Auxiliary Equipment" in the *SPE Guide on Extrusion Technology and Troubleshooting*, J. Vlachopoulos and J. R. Wagner, Jr., Eds., SPE, 2001]; and (b) tooth configuration showing the tooth-to-tooth interlock, creating the isolated "pockets" conveying the polymer charge in positive displacement.

shown in Figs. 6.46 and 6.47. Because the twin screws are counterrotating, feeding is facilitated. The volumetric flow rate is proportional to the speed of the counterrotating, intermeshing screws, as in the widely used gear pumps shown in Fig. 10.3(6).

Both positive displacement pumping devices are *rotational speed limited*, in that, at higher speeds, the pressures generated in the calender-like intermesh regions can generate very high shear and extensional rates and pressures, which may cause the melt films diametrically opposite to the intermesh to fail and deprive the machine of the lubrication benefit by the melt. A typical upper rotational speed limit is, for the *classic* intermeshing counterrotating extruders (as well as gear pumps), less than 150 rpm. This compares unfavorably with intermeshing, co-rotating TSEs, which are only torque limited and capable of very high rotational speeds of over 1000 rpm.

There is another limitation of these machines: the only site generating extensional flow, beneficial to both distributive and dispersive mixing, is the intermesh region, which affects only a small fraction of the polymer melt charge. As we will see later, in our introduction to the intermeshing, co-rotating TSEs, twin screw designs which generate extensional flows in more than one region of the cross-sectional area available to the polymer stream are clearly preferable in carrying out the elementary mixing steps. Thus, a *new class* of intermeshing, counterrotating TSEs has been developed that have *multilobal screw elements* to create multisite, elongational flows (7) similar to those generated by kneading elements in co-rotating intermeshing extruders. Such machines make wide use of screw element sequences and barrel sections, which are process and material appropriate. With segmented screw element pairs, such as the hexalobal, counterrotating mixing screw elements shown in Fig. 10.4, and using larger intermesh clearances, counterrotating TSEs can achieve good mixing, and operate at high rotational speeds and throughput rates.

The continuous mixer (CM) is a counterrotating, nonintermeshing *twin-rotor* machine. The Farrel Continuous Mixer (FCM) was the first CM developed (1964) by Ahlefeld et al. (8). It has rotor designs along the principles of the Banbury[3] high-intensity batch mixer.

---

3. "Banbury" is a registered trademark of the Farrel Co., Ansonia, CT.
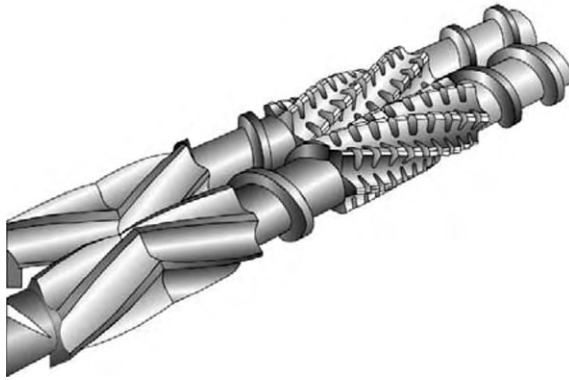
Fig. 10.4 Hexalobal, intermeshing, counterrotating twin-screw mixing screw elements. [Reprinted by permission from W. C. Thiele, ''Counterrotating Intermeshing Twin Screw Extruders,'' in *Plastics Compounding—Equipment and Processing*, D. B. Todd, Ed., Hanser, Munich, 1998.]

The latter, shown in Fig. 10.5, is still used extensively in the rubber compounding industry. The Banbury mixer consists of a figure-eight, cross-sectional–shaped mixing chamber with a spiral-lobed rotor in each chamber. The shape of the rotor is such that it induces axial flow and mixing along the rotors toward the center. The mixture is fed (using a variety of process-appropriate, ingredient-addition protocols) through a vertical chute in which an
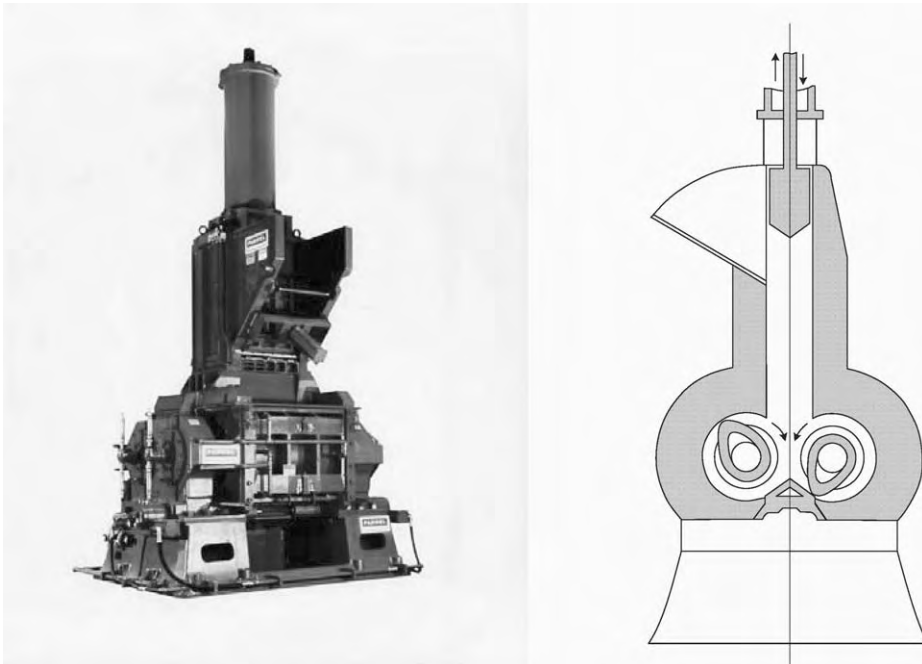

Fig. 10.5 Photograph and cross-sectional schematic representation of a Banbury high-intensity internal batch mixer. The photograph shows the two elements of the drive: the electrical motor and the gear reducer. Their large size is due to the very large power requirements of the mixer. [Photograph courtesy of the Farrel Company, Ansonia, CT.]

air- or hydraulic-driven ram can descend to seal the internal mixing chamber and force the mixture into the space between the rotors. The lower face of the ram is shaped in such a way that it becomes part of the chamber. Chamber sealing is critical to keeping the nanosized carbon black from getting out of the mixer and contaminating the room.[4] Dispersive mixing takes place in the clearances between the rotor and the barrel, and between the two counterrotating rotors in the trailing apex region. Distributive mixing is promoted by the axial twists of the rotor flight tips, as previously noted. The mixers operate about 70% full to enhance distributive mixing. The homogenized charge is discharged through a slide or ''drop door'' at the bottom of the chamber.

Soon after its introduction[5], the CM family of compounders came into widespread use as a rapid and high production rate machine used in thermoplastic compounding operations, because if its ability to both melt and mix at the required compounding production rates of 500–800 kg/h. Larger-size machines (ca. 300 mm · D) were also developed for the thermoplastics ''finishing'' operations as ''mega'' melter/mixers, achieving rates as high as 50 ton/h. For both applications, the rotational speeds are in the range of 400 to 1200 rpm. The CMs do not generate pressure, and therefore are always combined downstream with either a discharge extruder or a gear pump.

The top and cross-sectional views of a single stage FCM are shown in Fig. 10.6 (9). Note that the rotor shafts are supported at both ends. It is worth noting the following CM design characteristics: first, the high shear rate, tight clearance between the rotor-tip land area and the barrel is responsible for consuming much of the shaft mechanical energy by melting compressed polymer particulates, mainly by frictional energy dissipation (FED), and, further downstream, by viscous energy dissipation (VED), and plastic energy dissipation (PED) to eliminate the solids in the melt–solids suspension which *partially* fill the CM mixing chamber; second, the rotor-to-rotor, partial intermesh available cross-sectional area varies a great deal during each of the rapid rotations, creating considerable compressing/expanding extensional flows, both responsible for the CM's capacity to affect very rapid and efficient mixing; third, the two rotor wings, upstream and downstream of the apex, create strong axial flows leading to back mixing and three-dimensional chaotic flows; and finally, CMs have practically no pumping capability, necessitating the use of single screw melt extruders fed at just above atmospheric pressures for compounding applications, and gear pumps for the finishing operation applications. The tandem CM/SSE processing system for compounding applications is shown in Fig. 10.7

The fully intermeshing, co-rotating TSEs shown in Fig. 10.1 are by far the most widely used twin screw–based processing equipment. They were developed in the 1940s by

---

4. Fernley Banbury conceived the ''Banbury Mixer'' to replace the open roll mill mixing of rubber which covered everything, including the operators, with black dust. In fact, he intended to place the rolls in a closed environment. But since it was not possible to ''cut-and-turn'' the rubber in a closed chamber, as is done in two roll mill mixing to create axial mixing, he had to give the rolls a geometry that would induce axial mixing. He did this quite successfully and the Banbury mixers are in wide use to the present day. Perhaps, with the burst of other nanosized additives to the processing scene, the internal mixer may find additional applications.

5. The development of the FCM was undertaken with the intention of replacing the batch Banbury mixing with continuous operation mixing. However, it did not achieve the quality of batch mixing required by the rubber industry, and was not adopted by that industry. Yet just at the time when the development was concluded, high production volume of polypropylene (PP) and high density polyethylene (HDPE) came on board. These polymers emerge from the reactor in powder form and need immediate postreactor melting and compounding to convert them into useful pellets. The FCM, with its high melting and adequate mixing capacity, was readily adopted for this application.
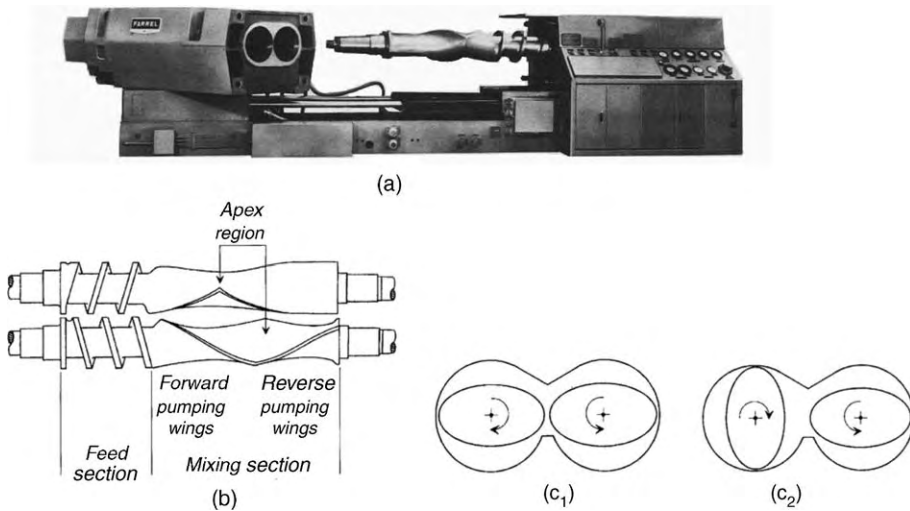
Fig. 10.6 The single-stage FCM. (a) Size 15 FCM with chamber opened and rotated hydrauli-cally; (b) top view of staged apex twin rotors and the axial zones for carrying out the solids feed handling and the melting and mixing elementary steps; (c) cross-sectional view of two rotor orientations, tip-to-tip (c_1) and tip-to-flat (c_2). [Reprinted by permission from E. L. Canedo and L. N. Valsamis, "Farrel Continuous Mixer Systems for Plastics Compounding," in *Plastics Compounding—Equipment and Processing*, D. B. Todd, Ed., Hanser, Munich, 1998.]

Erdmenger at Bayer A.G., who obtained a German patent in 1951 (10). They were further developed, under license, by Werner & Pfleiderer in the 1950s (11). The co-rotating, intermeshing skewered screw elements are self-wiping, which reduces the residence time of barrel wall melt films, and come in two forms: the screw conveying elements and the kneading paddle sequences, staggered to approximate conveying screw segments.
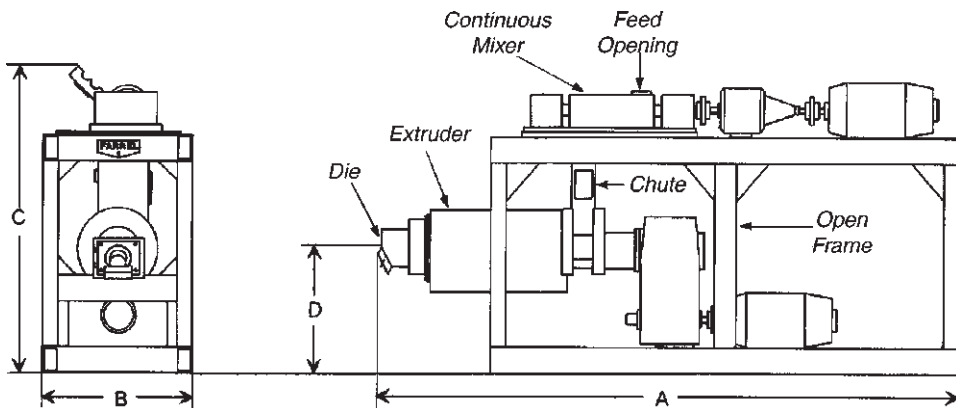

Fig. 10.7 Schematic view of the CM/single screw extruder combination used in polymer compounding operations. The *chute*, connecting the two processing machines, transfers the molten and mixed stream at low pressures to the throat of the melt pump SSE, which generates the pressure needed for pelletization. [Reprinted by permission from E. L. Canedo and L. N. Valsamis, Farrel Continuous Mixer Systems for Plastics Compounding in *Plastics Compounding—Equipment and Processing*, D. B. Todd, Ed., Hanser, Munich, 1998.]
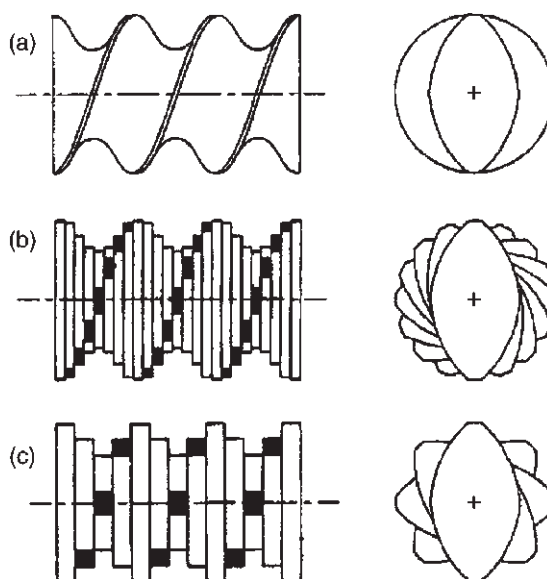
Fig. 10.8 Fully intermeshing, co-rotating elements in configurations matching square-pitch screws. (a) Forward screw conveying elements with different numbers of lobes; (b) forward staggered kneading paddles (a.k.a., disk elements) representing ''leaky'' screw elements, and (c) neutral configuration. [Reprinted by permission from D. B. Todd, ''APV (Baker Perkins) Systems,'' in *Plastics Compounding—Equipment and Processing*, D. B. Todd, Ed., Hanser, Munich, 1998.]

Single, bi-, tri-, and tetralobe screw profiles are shown in Fig. 6.42, and staggered bilobal kneading paddles are shown in Fig. 10.8(b)(3). The thinner each of the staggered paddles, the closer the paddle sequence comes to approximate the function of conveying screw elements, by affording smaller interpaddle spaces for polymer melt to leak backwards in the presence of a positive pressure gradient. Staggered kneading paddle sequences are specified by three numbers in the following order: the stagger angle, the number of paddles, and the total length of the sequence or ''block.''[6]

Both screw and staggered kneading disk sequences (blocks) can be built to convey polymer melts in the forward or reverse (backward) directions. They are shown schematically as forward/reverse (a.k.a., right- and left-handed) pairs in Fig. 10.9 (12). Both configurations provide a *flow barrier* at the axial position, joining the forward and reverse sequences. The physically obvious consequence at this juncture is the following: the pressure drop required to overcome the flow barrier must be provided by the forward drag flow of a specific length of filled forward screw or staggered paddle element sequence. Clearly, screws provide a stronger barrier, one that requires larger drag-induced pressure buildup by a longer filled section than the ''leaky'' kneading element forward/reverse pairs. Even stronger flow barriers, often utilized as ''melt seals'' before devolatilization sections in intermeshing, co-rotating TSEs, are the overlapping full-bore blister rings and a barrel valve (13) used in conjunction with them, as shown in Fig. 10.10. It is noteworthy that radial or axial barrel valves regulate on-line pressure buildup independently of any other process, material, or design variables, so they provide an added

6. For example, the Coperion (formerly-Werner & Pfleiderer) designation ''KB 45/5/40'' denotes a kneading block (KB) 40 mm long, made of five kneading paddles, staggered 45° part.
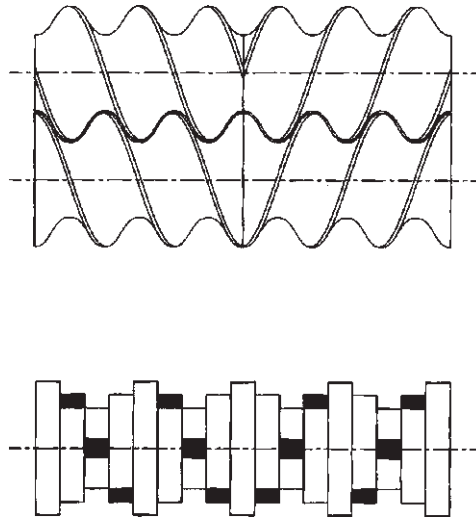
Fig. 10.9 Forward and reverse screw and kneading element sequences, both of which provide holdback capability.

variable for regulating the degree of fill and the mechanical energy dissipated in heating up the melt upstream of the valve (13,14).

We turn now to the most important capability of co-rotating kneading disks when they are full with the polymer stream, first pointed out by Todd (15). Figure 10.11 consists of five snapshots of a pair of co-rotating, bilobe kneading disks. The time-sequence of the snapshots documents the evolution of one of the three cross-sectional area pockets, the one that is shaded, A_s, available to be filled by the polymer charge. Of course, the disks have an axial thickness, H, and, thus, the volume available to the polymer charge is $(A_s H)$. As the pair of kneading disks co-rotate, A_s varies with time: first *expanding* from the minimum
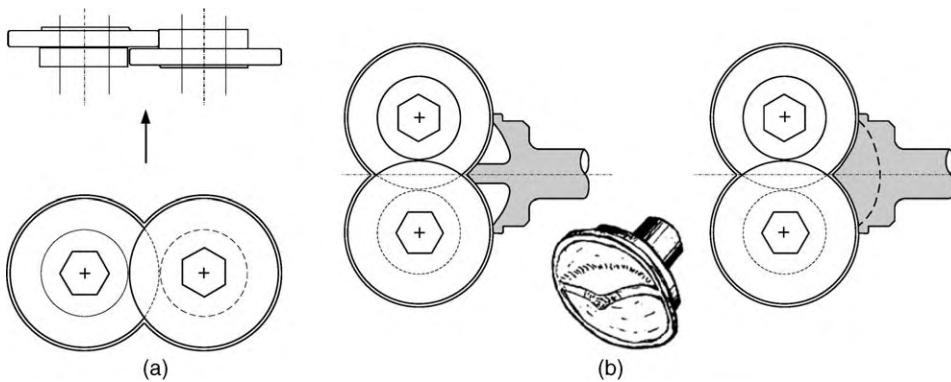

Fig. 10.10 (a) Top and side views of a pair of full-bore blister rings (orifice plugs), and (b) schematic of the Todd barrel valve and barrel cross sections in the fully open and closed positions: there is a bypass channel in the barrel immediately above the intersection of the blister rings and the barrel valve is rotatable in this bypass channel to vary the restriction of flow. [Reprinted by permission from D. B. Todd, "The APV (Baker Perkins) Systems," in *Plastics Compounding— Equipment and Processing*, D. B. Todd, Ed., Hanser, Munich, 1998.]

Fig. 10.11 Snapshots of the repetitive expansion/contraction of each of the cross-sectional area "pockets" between a pair of kneading disks and the barrel of fully intermeshing, co-rotating extruders. The evolution of the expansion/contraction is followed for one of the three "pockets," the one shaded, $A_s(t)$.

cross section it started to the maximum in the third snapshot, and then *contracting* to the minimum, this time in the right lobe of the barrel. If this pair of co-rotating disks is part of full forwarding or reverse kneading disk sequences, then one can see that as A_s expands from the first to the third snapshot, the material from adjacent upstream and downstream disk pairs will keep the pair full since, because of the stagger, the communicating cross-sectional areas of the upstream and downstream neighboring pairs will be contracting. Similarly, when A_s is contracting from the third to the fifth snapshot, our pair of disks will be providing material to the upstream and downstream neighbors. It is important to note that:

1. The *mixing* ramifications of this "repetitive" pairwise and axially staggered expansion/contraction of the cross-sectional area are:
   (a) Time-varying axial flow and back mixing.
   (b) Time-varying extensional and folding chaotic flows and "global" mixing by such flows as discussed in Chapter 7.
2. The *melting* ramifications of the "relentless" compressive deformations on packed particulates filling the kneading elements are that the rapid and volumewise melting mechanisms of FED and in particular, PED are introduced, inducing melting in very short axial distance segments, as discussed in Section 5.8.

It is important to note that similar beneficial mixing flows and solid polymer particulate charge deformations to those discussed earlier also occur in the multilobal variants of the counterrotating, "intermeshing" TSEs, as well as in CMs. We used the co-rotating, fully intermeshing twin screw kneading element pairs, because the relentless expansion/contraction cycles can best be demonstrated with them.

Finally, before embarking on the discussion and analysis of specific types of screw–based machines, we must state that not all of the elementary step mechanisms taking place in twin screw-based machines are completely understood as physical phenomena and, thus, cannot be adequately modeled and simulated, despite the explosive growth in accessible computing power and advances in Computational Fluid Mechanics (CFM). Funatsu et al. (16) correctly pointed out that numerical simulation of some elementary steps in twin screw-based machines is still difficult to carry out with predictive numerical treatment, because their understanding is currently under development and incomplete. This is true for plastic deformation of packed polymer particulates (17,18), melting and phase transition processes (17–21), and interface deformation and evolution (22,23). Therefore, three-dimensional numerical studies of twin screw-based machines are now limited to compositionally homogenized melts in filled mixing and pumping zones.

10.2 COUNTERROTATING TWIN SCREW AND TWIN ROTOR MACHINES

In this section we discuss the following counterrotating, twin rotor-based equipment: the fully intermeshing TSE, the tangential TSE, the multilobal compounders, the CM FCMs, and the Banbury-type batch intensive mixer. We will comment on all the elementary steps taking place in them, and do so quantitatively, when possible.

Flow and Mixing in Counterrotating, Intermeshing Twin Screw Extruders

We mentioned earlier that the classic intermeshing, counterrotating TSEs are essentially positive displacement continuous pumps, delivering the polymer charge at a constant rate, which is independent of the die pressure flow restriction. We also mentioned that the positively displaced material travels in an axial series of confined, *helical, C-shaped* pockets. While the term *confined* is only approximate, as we will see later, the positive displacement nature of melt pumping is both physically correct and amenable to rather simple flow analysis, which we presented in Section 6.8 (assuming, for simplicity, isothermal flow of a Newtonian fluid, Eqs. 6.8-15–6.8-34). Let us now expand this discussion to include particulate solids transport, melting, partially filled chambers, and leakage flows in both partially and filled chambers.

Counterrotating, intermeshing TSEs are typically gravity-fed. Provided that the barrel throat and screw under the hopper are adequately cooled, feeding is facilitated by the counterrotation of the two screws. The particulates fill C-shaped helical chambers in a consecutive fashion. Thus, in contrast to the single-screw *continuous* solid beds, the solid bed here is *divided* by the intermeshing flights of the other screw, and is transported downstream by positive displacement. There is little difference in pressure levels and particulate bulk-density levels between adjacent C-shaped chambers. Limited frictional drag-induced pressurization is possible only within individual isolated chambers. Thus, with constant downstream screw geometry, and taking into consideration that the particulate bulk density is appreciably smaller than the melt density, the C-shaped chambers can only be partially filled upon melting, becoming fully filled further downstream, as we will see later. To obtain better filling, these extruders can be designed with different screw geometries under the hopper, for example, a greater pitch and more screw starts, which are aimed at providing for a constant *mass flow rate* rather than a constant volumetric flow rate, in the downstream direction.

Melting begins and is completed inside each of the C-shaped chambers. The downstream melting length is of the order of one diameter, almost an order of magnitude shorter than that of the typical melting length of SSEs. Janssen (24) conducted screw-pulling experiments similar to those we presented in connection with the SSEs' melting mechanism presented in Chapter 9. He extruded PP powder, of 0.65 g/cc bulk density and 0.72 g/cc melt density, in a double-flighted 47-mm extruder. The melting experiments were carried out at two low rotational speeds of 4.3 and 10.2 rpm, using two dies, one resulting in a 50-psi and the other in 2700-psi die pressure drop. He observed that melting lengths inside the more or less isolated C-shaped chambers were smaller than typical SSE lengths. This is not surprising, since the rotational speeds were very low, resulting in long exposures to conductive heating aided by the internal C-shaped chamber circulatory flow, as discussed in Section 6.8. Furthermore, two melting mechanisms were observed and attributed to the different die pressures used, from the examination of polished C-segment cross sections along the downstream direction, shown schematically in Fig. 10.12.
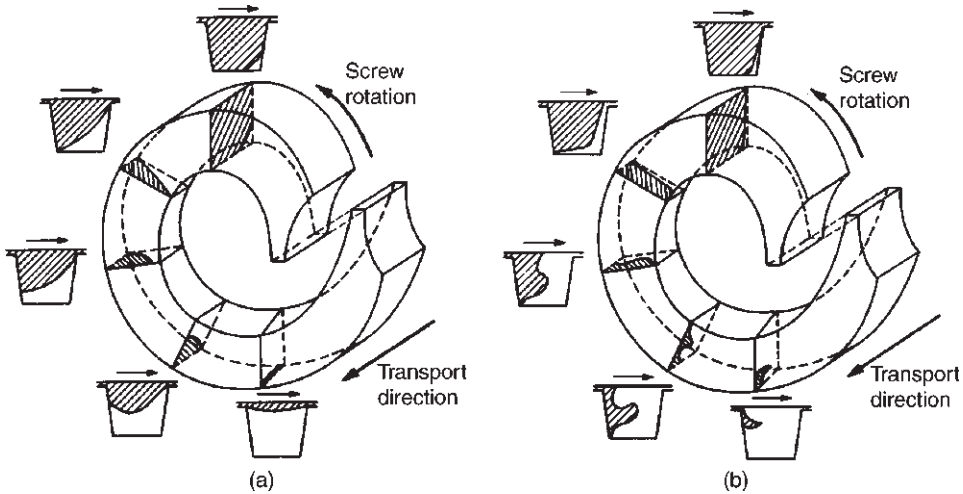
Fig. 10.12   Schematic representation of two melting mechanisms observed by Janssen (24) with PP processed in a double-flighted 47-mm counterrotating TSE operating at low rotational speeds. (a) Melting when the die pressure was set at the low value of 50 psi, where chamber-to-chamber leak pressure backflows are negligible. (b) Melting under the high die pressure of 2700 psi, which enables leak backflows, which result in chamber solid bed compaction and introduce the possibility of dissipative mix melting. [Reprinted by permission from L. P. B. M. Janssen, *Twin Screw Extrusion*, Elsevier Scientific, Amsterdam, 1978.]

The cross-sectional view of melting evolution, starting from the bottom and proceeding clockwise in Fig.10.12, represents the first and last stages of melting in downstream successive chambers during the same experiment. In Fig. 10.12(a) the melting mechanism is indicative of drag-assisted conductive melting provided by the barrel under a low die pressure of 50 psi. Note that no melt pool is created at the pushing-screw flight. Rather, the melt created by the mechanism just discussed penetrates into the incompletely packed particulate bed, creating a well. This 'well', in turn, is deformed toward the pulling flight at later melting stages by the circulatory melt flow to form a melt wedge that grows until the completion of melting. In Fig.10.12(b), melting conducted under a high die pressure of 2700 psi indicates that during the early stages of melting with this mechanism, melt from the downstream chamber *leaks* back into the chamber just upstream, compacting the particulate bed. That is, in this mechanism, the chambers in the melting zone are not isolated, but communicate through chamber-to-chamber leak pressure backflows. We will see later that, at large die pressure drops, these very important leak flows extend to many C-shaped chambers upstream of the die. The melting process continues by long-exposure–conductive, barrel–solid, and melt–solid melting, as well as *mild* dissipative mix melting (DMM), discussed in Chapter 5. This last melting contributor is small because of the two very low rotational speeds employed during the experiments. For this reason, melting under the low die pressure, as in Fig. 10.12(a), started at the fifth chamber from the hopper and ended at the seventh, often resulting in a chamber partially filled with melt, while, at the high die pressure, melting started at the fifth and ended in the ninth chamber. It is expected that at an order-of-magnitude higher screw speed, but still under the operational limits of counterrotating, intermeshing, TSEs DMM mechanisms, play a more dominant and beneficial melting role. Indeed, this appears to be so. White and co-workers (25–27)
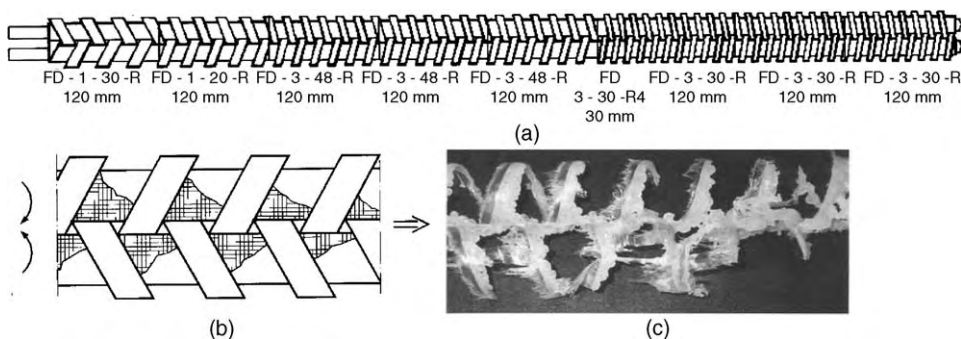
FD - 1 - 30 -R   FD - 1 - 20 -R   FD - 3 - 48 -R   FD - 3 - 48 -R   FD - 3 - 48 -R   FD   FD - 3 - 30 -R   FD - 3 - 30 -R   FD - 3 - 30 -R
120 mm   120 mm   120 mm   120 mm   120 mm   3 - 30 -R4   120 mm   120 mm   120 mm
30 mm

(a)

(b)   (c)

Fig. 10.13   Melting of low density polyethylene (LDPE) (Equistar NA 204-000) in a starve-fed, fully intermeshing, counterrotating Leistritz LMS 30.34 at 200 rpm and 10 kg/h. (a) The screw element sequence used; (b) schematic representation of the melting mechanism involving pellet compressive deformation in the calender gap; (c) the carcass from screw-pulling experiments. [Reprinted by permission from S. Lim and J. L. White, "Flow Mechanisms, Material Distribution and Phase Morphology Development in Modular Intermeshing counterrotating TSE," *Int. Polym. Process.*, **9**, 33 (1994).]

have experimentally examined the melting behavior in *starve-fed*, fully intermeshing (thick-flighted), counterrotating extruders, such as the one shown in Fig. 10.13(a), operating at 100–200 rpm, and found that melting starts a short distance downstream from the hopper, far away from the melt-filled C-shaped chambers, and is complete in less than three diameters. They attribute melting primarily to PED of the pellets in the interscrew "calender-like" gap, where they are dragged by the counterrotation and undergo a compressive/squeezing plastic deformation, as shown schematically in Fig.10.13(b). This pellet-dragging process continues until the entire pellet bed is depleted, Fig. 10.13(c), that is, here PED replaces the mechanism of conductive melting with drag-induced melt removal, which is responsible for melting in SSEs, discussed in Chapter 5.

Following the completion of melting, under low die pressures the chamber will typically be partially filled, while melt will occupy the entire chamber under high die pressures, ΔP_{die}, due to pressure backflows. Assuming that the melt viscosity and screw geometry are constant, the number of fully filled chambers, n_f, is

$$n_f = \frac{\Delta P_{\mathrm{die}}}{\Delta P_c} \qquad (10.2\text{-}1)$$

where the denominator represents each of the equal interchamber pressure drops. Thus, the transition from the partially to the fully filled zone takes placed within one pitch, after the die pressure drop has been "exhausted." Of course, the preceding equation is approximate, since the viscosity will decrease downstream due to increases in temperature, themselves intensifying with increasing operating die pressures (24). Concerning interchamber leak flows, Janssen (24) states that, although the theoretical volumetric pumping capability of the fully filled metering chambers (see Section 6.8) is
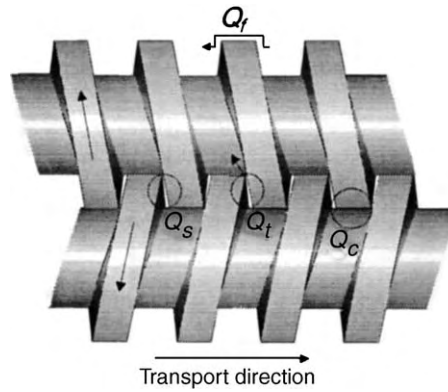
$$Q_{th} = 2mNV_c \qquad (10.2\text{-}2)$$

Fig. 10.14 The location of four gaps in "fully" intermeshing, counterrotating extruders though which leak flows can take place. [Reprinted by permission from A. J. van der Goot, O. Poorter, and L. P. B. M. Janssen, "Determination of the Degree of Fill in a Counterrotating TSE," *Polym. Eng. Sci.*, **38**, 1193 (1998).]

where m is the number of screw starts, N the rotational speed, and V_c the chamber volume, the real pumping capacity is

$$Q = Q_{th} - Q_l \tag{10.2-3}$$

where Q_l represents the sum total of all the leakage flows over a cross section of the extruder. Four different leakage flows were identified by Janssen et al. (24,28) and van der Goot et al. (29) in fully intermeshing, counterrotating extruders, as shown in Fig. 10.14: over the flight gap, Q_f; the tetrahedron gap, Q_t; the calender gap, Q_c; and the side gap, Q_s. They are caused by the drag of the moving surfaces and the interchamber pressure differences, ΔP_{c_i}, which, at first approximation, are taken to be the same in every filled chamber. Thus, they have the familiar generic form

$$Q_l = AN + B\frac{\Delta P_c}{\eta} \tag{10.2-4}$$

in which A and B are constants of the equipment geometric (design) variables, specific for each type of leak flow. They can be calculated approximately for isothermal flows, and using effective viscosities, η, from equations derived by Janssen (24,28).

The degree of fill in the partially filled zone, α_f, is (26)

$$\alpha_f = \frac{Q}{Q_{th}} \tag{10.2-5}$$

and, since ΔP_c in partially filled chambers is zero, the effective leak flow volumetric rate $Q_{l,pfz}$ is

$$Q_{l,pfz} = AN \tag{10.2-6}$$

and

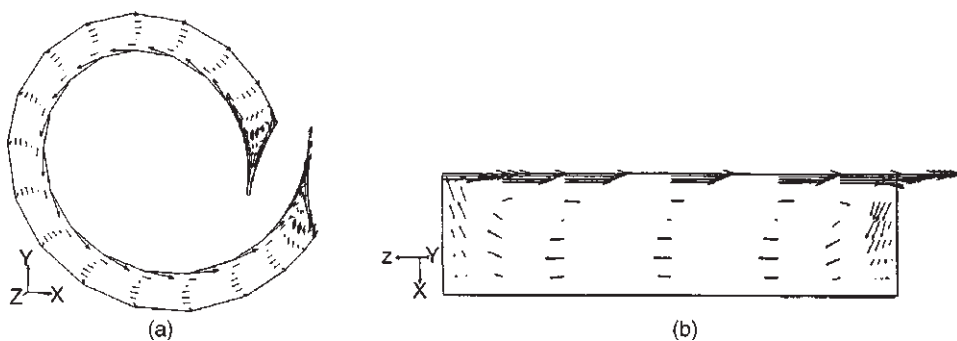$$\alpha_f = \frac{Q + Q_{l,pfz}}{Q_{th}} \tag{10.2-7}$$

Fig. 10.15 (a) Velocity profile in the down-channel direction on a helically wound plane in the middle of the C-shaped chamber; (b) projection of the velocity field on a plane perpendicular to the helical plane of the C-shaped chamber. [Reprinted by permission from T. Li and I. Manas-Zloczower, "A Study of Distributive Mixing in Counterrotating TSEs," *Int. Polym. Process.*, **10**, 314 (1995).]

The preceding expressions are approximate and based on the assumption of isothermal one-dimensional flow of a Newtonian fluid. Speur et al. (30) studied the full calender gap, two-dimensional flows using finite element methods (FEM), and concluded that the presence of vortices depends on the magnitude of the calender-gap leak flow.

Li and Manas-Zloczower (31) used the CFM commercial "FIDAP" FEM package to simulate the three-dimensional isothermal flow patterns and distributive mixing in three consecutive filled, closed C-shaped chambers of fully intermeshing, counterrotating extruders, having the dimensions of Leistritz 30.34 (30 denotes the centerline distance and 34 the barrel diameter in mm units). An equal pressure drop per C-shaped chamber was applied for the calculations. The melt was assumed to be Power Law above $\dot{\gamma}_0$ and Newtonian below it. The design, process, and material variables are given by the authors.

The velocity in the down-channel direction, Fig. 10.15(a), indicates that most of the fluid undergoes circulatory flow, as expected. A circulatory flow is also generated in the plane perpendicular to the helical surface of the C-shaped chambers, Fig. 10.15(b). Velocity vectors indicating calender-gap leakage flows, Q_c, are shown, without using them to obtain leakage flow rates. The interaction between the two circulatory flows eliminates the possibility of a stagnant layer at $y/H = 2/3$.

Li and Manas-Zloczower also studied numerically the dynamics of distributive mixing by tracking the evolution of particle positions, originally gathered as randomly placed clusters, as shown in Fig. 10.16. The evolution of particle position distribution just discussed indicated a fast initial distributive mixing, which levels off but at reasonably high values. This is also borne out through the computation of distributive mixing efficiency measures, such as the length stretch, λ, used by the authors.

Comparison of Flow and Mixing in Open C-Shaped Channels of Counterrotating and Co-rotating Twin Screws   Katziguara et al. (32) conducted three-dimensional FEM numerical studies in fully filled, melt conveying, thin-flighted, that is, open C-shaped channels of both counterrotating and, for comparison, co-rotating TSEs. The two screw configurations studied are shown in Fig. 10.17. In the first of a series of systematic numerical studies made by the group, they calculated the velocity field and, from this, the spatial distribution of tracer particles and the residence time distribution. They also
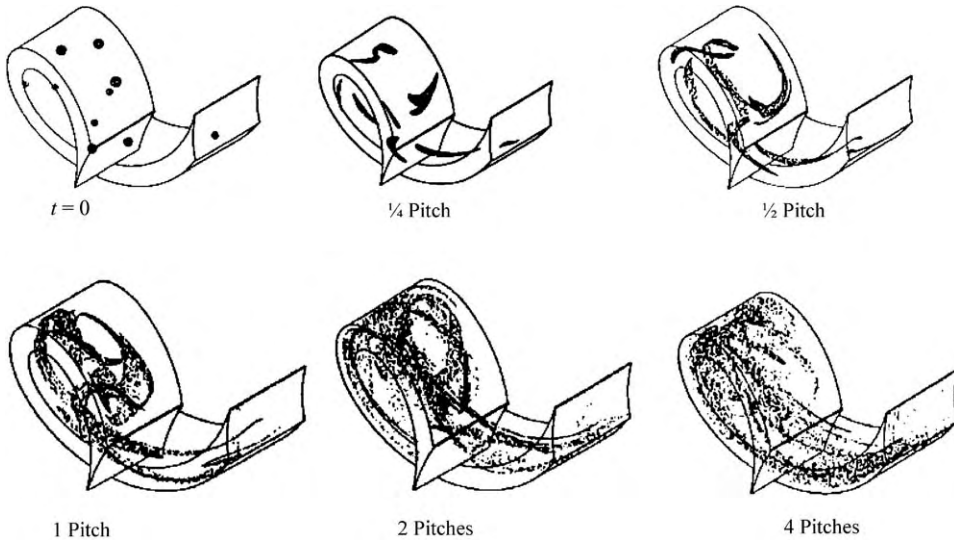
t = 0   ¼ Pitch   ½ Pitch

1 Pitch   2 Pitches   4 Pitches

Fig. 10.16   The evolution of the spatial distribution of 10,000 particles initially clustered in 10 randomly placed clusters in the C-shaped chamber. The fraction or number of pitches denotes the axial advance of the material in the chamber due to the counterrotation. [Reprinted by permission from T. Li and Ica Manas-Zloczower, "A Study of Distributive Mixing in Counterrotating TSEs," *Int. Polym. Process.*, **10**, 314 (1995).]
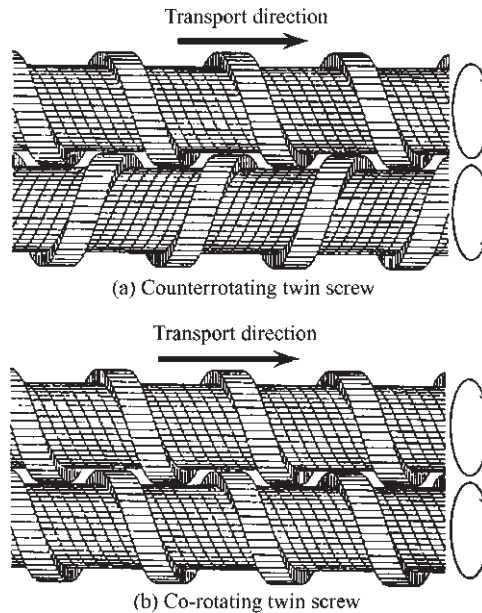

Transport direction

(a) Counterrotating twin screw

Transport direction

(b) Co-rotating twin screw

Fig. 10.17   The counter- and co-rotating thin-flight, open C-shaped channels used in the three-dimensional FEM study of Katziguara et al. (32). The two-screw configurations are identical except for the sense of rotation. [Reprinted by permission from T. Katziguara, Y. Nagashima, Y. Nakano, and K. Funatsu, "A Numerical Study of TSEs by 3-D Flow Analysis – Development of Analysis Technique and Evaluation of Mixing Performance for Full Flight Screws," *Polym. Eng. Sci.*, **36**, 2142 (1996).]

obtained the stress field responsible for dispersive mixing. The numerical simulation was conducted assuming isothermal, steady, incompressible, non-Newtonian, Carreau-type fluid flow, in fully filled channels, with no slip at the walls, neglecting inertia and gravitational forces, and assuming fully developed flow far away from the nip region.

The fully filled channel and the isothermal assumptions are not realistic in that, in practice, channels are partially filled and the flow is nonisothermal. The constitutive equation and the equations of change used are:

$$\tau = 2\eta\dot{\gamma} \tag{10.2-8}$$

$$\eta = \eta_0 \left[1 + \left(\lambda\text{II}_{\dot{\gamma}}\right)^2\right]^{(n-1)/2} \tag{10.2-9}$$

$$\boldsymbol{\nabla} \cdot \mathbf{v} = 0 \tag{10.2-10}$$

$$-\boldsymbol{\nabla} P + \boldsymbol{\nabla} \cdot \boldsymbol{\tau} = 0 \tag{10.2-11}$$

A low density polyethylene was used with Carreau model parameters: $\eta_0 = 19,500 \,\text{Pa} \cdot \text{s}$; $\lambda = 5.5 \,\text{s}; n = 0.52$. The screw speed was 100 rpm and the pertinent geometric parameters appear in Fig. 10.18 with their numerical values are listed in Table 10.1

The numerical analysis domain can be reduced to the one-pitch segment shown in Fig. 10.19 and further reduced to the midregion containing the intermesh zone, based on the assumption that the flow is fully developed far from the intermeshing zone. In other words, the channel flow region, which is far from the nip region, is omitted. The boundary conditions used were: the flow at cross sections A and B are fully developed and obtained
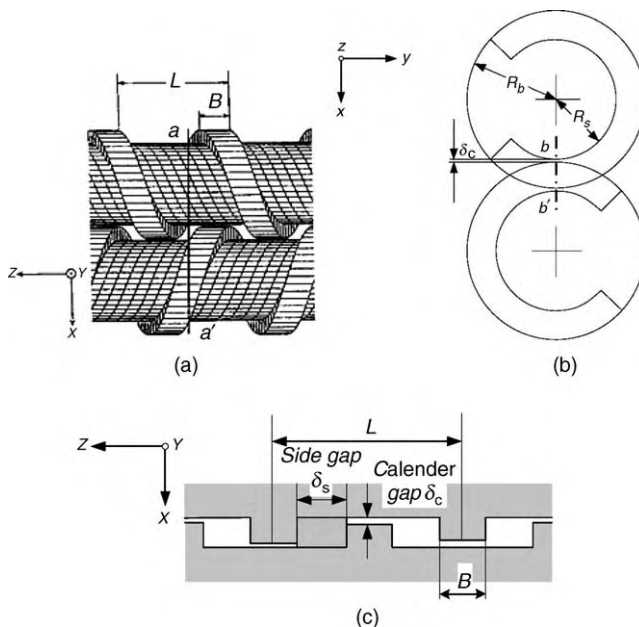

Fig. 10.18 Definition of the geometric parameters. (a) Screw configuration; (b) a–a' (x–y) plane; (c) b–b' (x–z) plane. [Reprinted by permission from T. Katziguara, Y. Nagashima, Y. Nakano, and K. Funatsu, "Numerical Study of Twin Screw Extruders by 3-D Flow Analysis – Development of Analysis Technique and Evaluation of Mixing Performance for Full Flight Screws," *Polym. Eng. Sci.*, **36**, 2142 (1996).]

TABLE 10.1   Values of the Geometric Parameters in Fig. 10.18

Pitch	L (mm)	40
Flight width	B (mm)	10
Barrel radius	R_b (mm)	20
Screw radius	R_s (mm)	15
Side gap	δ_s (mm)	10
Calender gap	δ_C (mm)	0.5
Helix angle	θ (deg)	17.65

the same way as in a SSE; and the flows in the domain boundaries C and D are the same as that in the central crosssection of the C-shaped channel in the opposite screw, cross section E, because of the steady periodic condition. The computational scheme used was as follows: An initial guess was made for cross sections C and D, and the whole domain field was calculated using this guess. The obtained flow for cross section E was then used for C and D for a second iterative step, and iterations continued until convergence.

The coordinate system employed moves in the axial direction with the apparent forward velocity of the screw, that is, 40 mm/s, ensuring that the analysis domain will be time invariant. In this coordinate system, a given point can be observed to move in the direction parallel to the flight. It should be noted that in this coordinate system, down-channel velocity components may appear as having negative values. Velocity fields for the counterrotating channels were obtained at two planes perpendicular to the screw axes: plane (I) at the midpoint of the side gap, and plane (II) at the midpoint of the calender gap. They are shown in Fig. 10.20. The axial velocity contour and velocity vectors at plane (I) are shown in Fig. 10.21. The corresponding axial velocity contours and vector at the calender gap, plane (II), are shown in Fig. 10.22. Half of the cross section is shown since symmetry exists. At the calender gap, plane (II), the tight clearance decreases the axial velocity field over the entire cross section, as compared to those at plane (I). The contours at plane (II) are y-axis symmetric (closed C-shaped chambers) with negligible axial velocities at the gap, while for the side gap, the symmetry axis for the contours is different, involving both lobes of the barrel. All axial velocities are downstream positive at both planes of the counterrotating screws.

Turning, for comparison, to the co-rotating screws with identical geometrical parameters, let us examine once again the axial velocity contours and velocity vectors
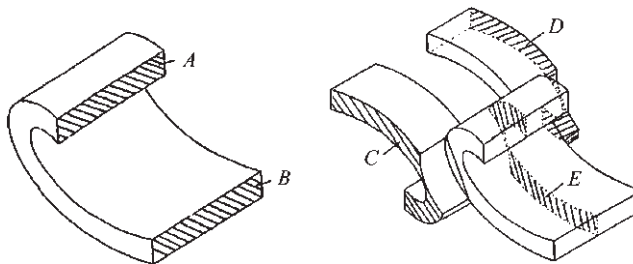

Fig. 10.19   The analysis domain and identification of the cross sections used in the discussion on boundary conditions below. [Reprinted by permission from T. Katziguara, Y. Nagashima, Y. Nakano, and K. Funatsu, "Numerical Study of Twin Screw Extruders by 3-D Flow Analysis – Development of Analysis Technique and Evaluation of Mixing Performance for Full Flight Screws," *Polym. Eng. Sci.*, **36**, 2142 (1996).]
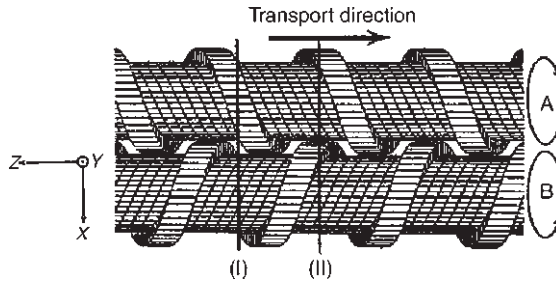
Fig. 10.20 Axial location of the two planes perpendicular to the counterrotating screws, where velocity fields were calculated. Plane (I) is at the middle of the side, and plane (II) at the middle of the calender gaps. [Reprinted by permission from T. Katziguara, Y. Nagashima, Y. Nakano, and K. Funatsu, "Numerical Study of Twin Screw Extruders by 3-D Flow Analysis – Development of Analysis Technique and Evaluation of Mixing Performance for Full Flight Screws," *Polym. Eng. Sci.*, **36**, 2142 (1996).]

at plane (I), midway to the co-rotating side gap, and at plane (II), midway to the co-rotating calender gap. They are shown in Fig. 10.23. We note that negative upstream velocities exist at both planes, and at plane (I) in the side gap region, a very high axial velocity gradient contributes to axial mixing. The velocity vectors at plane (I) also indicate that there is material transfer from lobe to lobe at the side-gap plane (II).
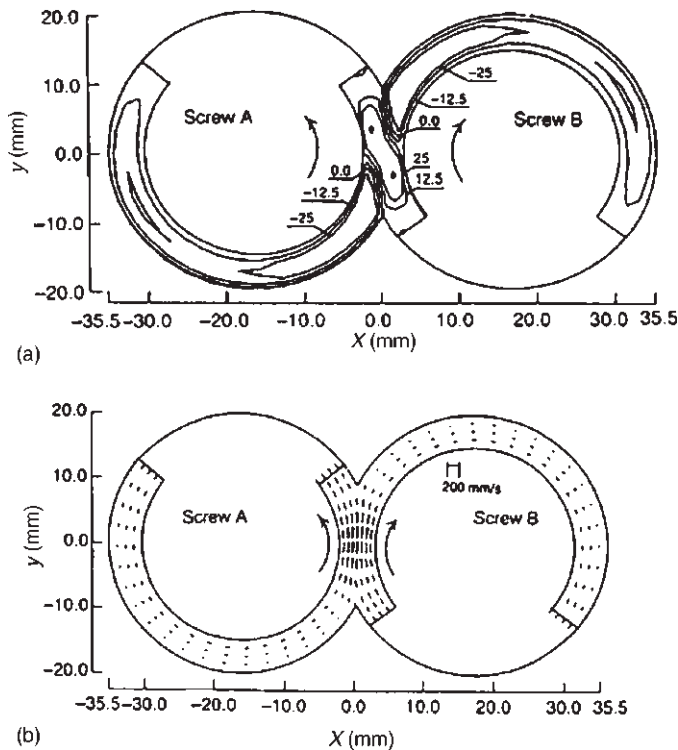

Fig. 10.21 Plane (I): (a) Contours of the axial velocity; (b) velocity vectors at the side gap region, in (mm/s). [Reprinted by permission from T. Katziguara, Y. Nagashima, Y. Nakano, and K. Funatsu, "Numerical Study of Twin Screw Extruders by 3-D Flow Analysis – Development of Analysis Technique and Evaluation of Mixing Performance for Full Flight Screws," *Polym. Eng. Sci.*, **36**, 2142 (1996).]

Fig. 10.22 Plane (II) at the calender gap: (a) contours of axial velocity; (b) velocity vectors, in (mm/s). [Reprinted by permission from T. Katziguara, Y. Nagashima, Y. Nakano, and K. Funatsu, "Numerical Study of Twin Screw Extruders by 3-D Flow Analysis – Development of Analysis Technique and Evaluation of Mixing Performance for Full Flight Screws," *Polym. Eng. Sci.*, **36**, 2142 (1996).]
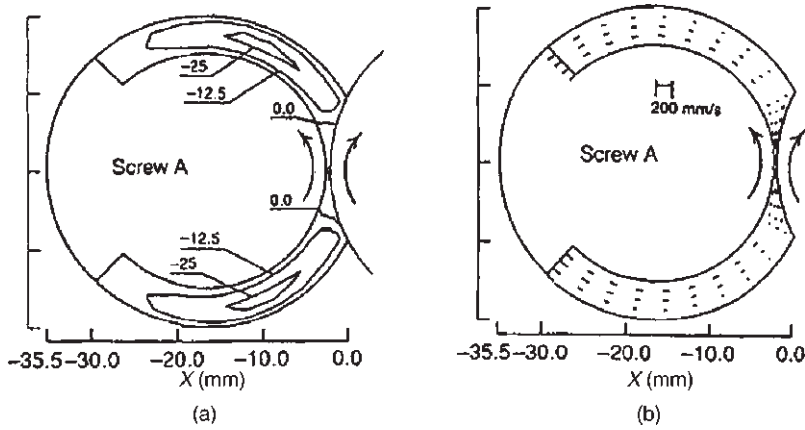
The flow rates, Q, for the counter- and co-rotating screw pumps in Fig. 10.17, the two leak flow, Q_C and Q_S, shown in Fig. 10.24, as well as the flow from screw A to screw B, Q_{AB}. Flows Q, Q_{AB}, Q_C, and Q_s are listed in Tables 10.2 and 10.3.

The pumping ability of the thin-flighted, filled co-rotating screw is about 1.4 times that of the counterrotating screw. The side-gap flow with the counterrotating screw is 90% of the
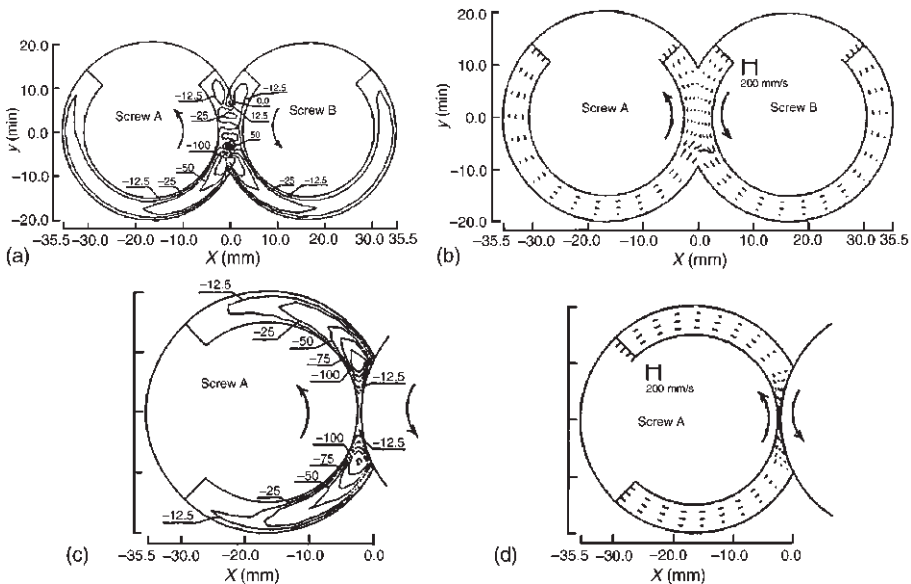

Fig. 10.23 Co-rotating channels. (a) Contours of axial velocity at plane (I); (b) velocity vector at plane (I); (c) contours of axial velocity at plane (I); (d) velocity vectors at plane (II), in (mm/s). [Reprinted by permission from T. Katziguara, Y. Nagashima, Y. Nakano, and K. Funatsu, "Numerical Study of Twin Screw Extruders by 3-D Flow Analysis – Development of Analysis Technique and Evaluation of Mixing Performance for Full Flight Screws," *Polym. Eng. Sci.*, **36**, 2142 (1996).]

Fig. 10.24 Identification of the calender and side-gap cross sections and leak flows Q_S and Q_C. [Reprinted by permission from T. Katziguara, Y. Nagashima, Y. Nakano, and K. Funatsu, "Numerical Study of Twin Screw Extruders by 3-D Flow Analysis – Development of Analysis Technique and Evaluation of Mixing Performance for Full Flight Screws," *Polym. Eng. Sci.*, **36**, 2142 (1996).]
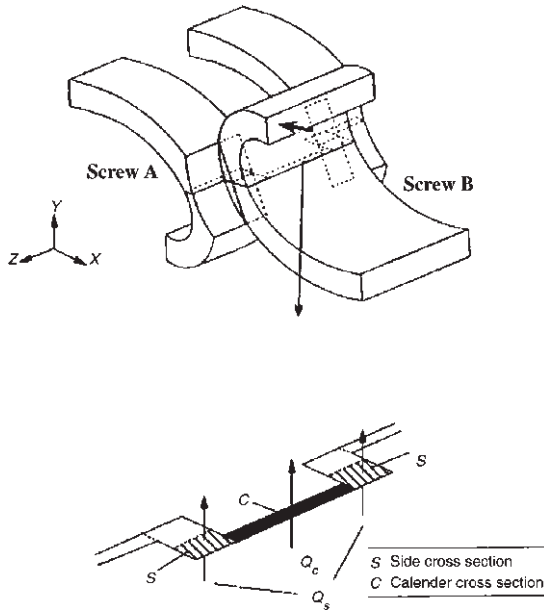
TABLE 10.2 Flow Rate and Average Velocity in the Transport Direction

	Flow Rate (cm^3/s)	Average Velocity (cm/s)
Counterrotating	10.84	1.408
Co-rotating	15.14	1.670

total flow, the calender gap flow is 5%, and the cross-screw flow around 1%, that is, there is no material transfer from screw to screw. By contrast and for comparison, with the co-rotating screws, the calender-gap leak flow is around 1% of the total, and the side-gap leak flow is 20%, both less than in the counterrotating screws, but the cross-screw flow is 83%, denoting very effective screw-to-screw distributive mixing. The contrast in the magnitude of Q_{AB} is supported by the numerical determination of the evolution of spatial distribution of tracers in the rotational direction in both counter- and co-rotating filled channels. Figure 10.25 presents such results for tracer particles aligned in 15 lines along the channel-width

TABLE 10.3 Flow Rates of Various Kinds of Leakage Flows

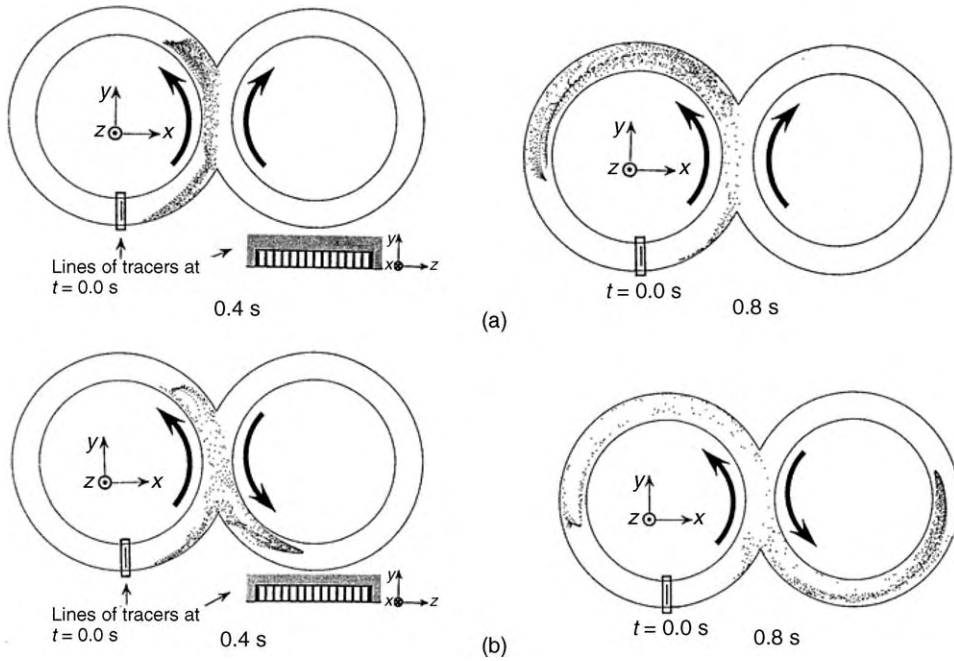|	Q_C/Q	Q_S/Q	Q_{AB}/Q
Counterrotating	0.058	0.910	0.016
Co-rotating	0.015	0.194	0.831

Fig. 10.25   Evolution of the spatial distribution of tracer particles initially placed at the location of the left lobe, as shown for (a) counterrotating, and (b) co-rotating filled channels. [Reprinted by permission from T. Katziguara, Y. Nagashima, Y. Nakano, and K. Funatsu, "Numerical Study of TSEs by 3-D How Analysis-Development of Analysis Technique and Evaluation of Mixing Performance for Full Flight Screws" *Polym. Eng. Sci.*, **36**, 2142 (1996).]

direction, as shown, each line having 80 particles in the y direction. All particles are projected on the cross section perpendicular to the screw axes and are also distributed in the axial direction. We find that most, if not all, of the particles stay in the initial lobe with counterrotating screws, while a considerable number of them are transferred to the other screw. These results suggest that the co-rotating screws can achieve effective distributive mixing from screw to screw, and from Fig. 10.23, also better axial mixing. This attribute is important to reactive extrusion, which requires distributive mixing of miscible components.

Finally, Katziguara et al. calculated the isothermal flow stress field, whose strength, locally, is the driving force of dispersive mixing of agglomerates. The invariant stress measured used is

$$\sigma = \sqrt{(\tau_{\max})_{xy}^2 + (\tau_{\max})_{yz}^2 + (\tau_{\max})_{zx}^2} \qquad (10.2\text{-}12)$$

where $(\tau_{\max})_{xy}$ denotes the maximum shear stress in the x-y plane and can be obtained as

$$(\tau_{\max})_{xy} = \sqrt{4\tau_{xy}^2 + (\tau_{xx} - \tau_{yy})^2} \qquad (10.2\text{-}13)$$

therefore

$$\sigma = \sqrt{4(\tau_{xy}^2 + \tau_{yz}^2 + \tau_{zx}^2) + (\tau_{xx} - \tau_{yy})^2 + (\tau_{yy} - \tau_{zz})^2 + (\tau_{zz} - \tau_{xx})^2} \qquad (10.2\text{-}14)$$
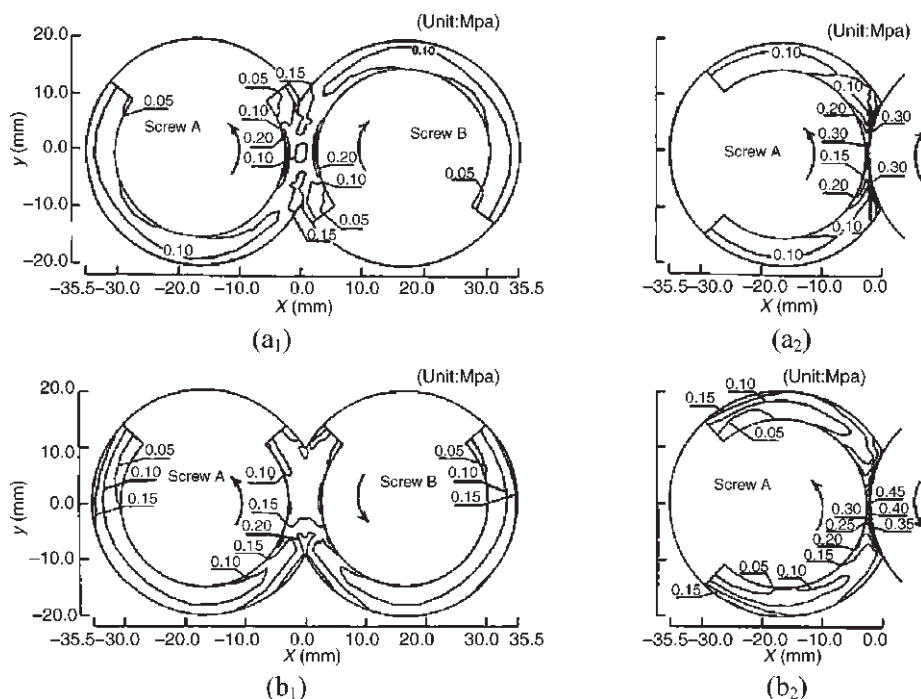
Fig. 10.26 The stress measure, σ, contours. (a_1) Counter-, side gap, plane (I). (a_2) Counter calender gap, plane (II). (b_1) Co-plane (I) and (b_2) Co-plane (II). [Reprinted by permission from T. Katziguara, Y. Nagashima, Y. Nakano, and K. Funatsu, "Numerical Study of Twin Screw Extruders by 3-D Flow Analysis – Development of Analysis Technique and Evaluation of Mixing Performance for Full Flight Screws," *Polym. Eng. Sci.*, **36**, 2142 (1996).]

Figure 10.26 shows the contours of the stress measure, σ, in Mpa in the two planes used in the numerical evaluation of the velocity fields: plane (I) in the side gap and plane (II) in the calender gap in both the counter- and co-rotating filled screw channels. Higher stress contours are found on the flight in the calender gap region in both counter- and co-rotating screws. Additionally, the stresses at plane (I) for both counter- and co-rotating channels are very similar. Thus, from a dispersive stress field point of view, both are the same, while from their distributive mixing abilities, the co-rotating screws are clearly superior.

Devolatilization in Counterrotating Twin Screw Extruders

Sakai and Hashimoto (33) presented experimental results on devolatilization of a mixture of octane/hexane in linear low density polyethylene (LLDPE) from 10% to 0.01%, as well as a rubber slurry of 42% chloroprene and of 58% slurry in carbon tetrachloride in a JSW TEX 65 counterrotating, intermeshing, TSE. The LLDPE mixture was prepared in SSE upstream, where the octane/hexane was added to the melt with a plunger pump, which maintained constant concentration and was fed directly under pressure into the feed throat of the counterrotating, vented, TSE.

Venting takes place in these devices without the risk of vent-port fouling. The counterrotation of the screws forces the bubble-rich melt to remain inside the extruder and away from the vent port. On the other hand, in fully intermeshing extruders, because
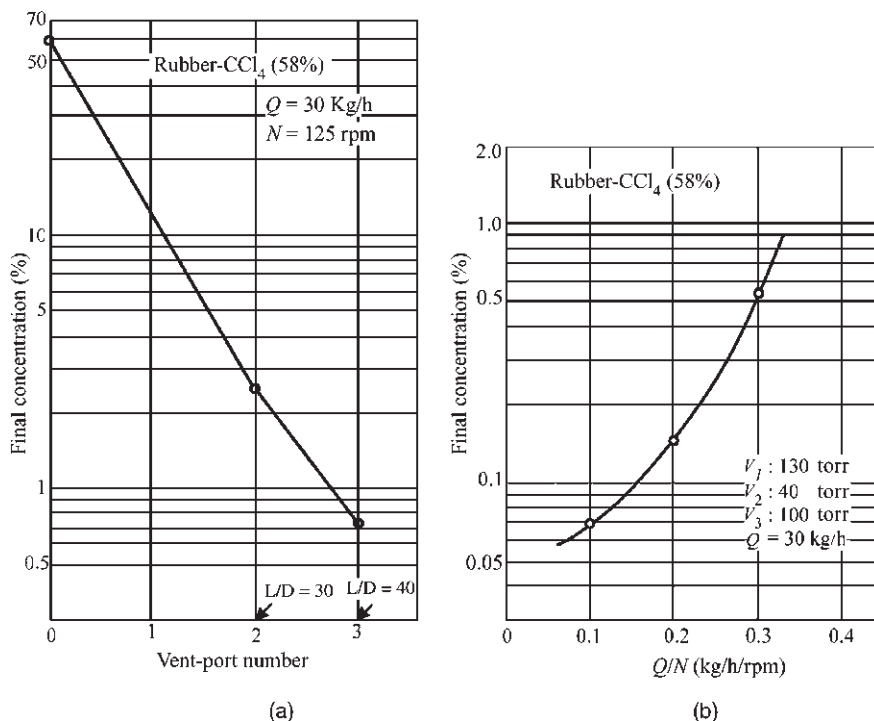
Fig. 10.27   Devolatilization of a 42% polychloroprene–58% CCl₄ in a JSW TEX 65 counter rotating, intermeshing TSE. (a) The effect of increasing the number of vent ports at $Q = 30 \, kg/h$ and $N = 125$ rpm. (b) The effect of decreasing Q/N ratio, at constant Q. [Reprinted by permission from T. Sakai and N. Hashimoto, "Application of Novel Counter-rotating Intermeshed Twin Extruder for a Degasing Operation." *SPE ANTEC Tech Papers*, **32**, 860 (1986).]

the C-shaped chambers are more or less isolated, devolatilization can take place only below the vent port itself (12). For this reason Sakai used two and three vent ports in the experiments, in order to increase the number of stages (see Chapter 8), thus decreasing the final solvent concentration. Figure 10.27(a) shows the beneficial effects of multiple vent ports for the rubber slurry. Additionally, since the surface of a single C-shaped chamber is limited, compared to that in a co-rotating, intermeshing vent section between two melt seals, increasing the screw rotational speed N at constant flow rate Q will be beneficial, since the rate of melt/solvent rate renewal will be increased. This is shown in Fig. 10.27, again for the rubber slurry.

Reactive Processing in Counterrotating Twin Screw Extruders

Dey and Biesenberger (34) have reported results of reactive extrusion of methyl methacrylate in a counterrotating, fully intermeshing, Leistritz 30.34 TSE. Five single-flighted, 6-mm pitch, 120-mm-long screw elements followed by two triple-flighted, 30-mm pitch, 120-mm-long screw elements were used, with barrel temperature and screw rotational speed as the processing variables. Benzoyl peroxide was used as the initiator and the feed was a polymethyl-methacrylate prepolymer, to reduce the quantity of heat to be removed due to the polymerization exotherm, which is significant. Isothermal differential

scanning calorimetry (DSC) experiments were conducted to obtain the temperature-dependent polymerization rate constants. The molecular weight was determined by solution viscometry after obtaining the Mark–Howink constants from Water Associates, $\alpha = 0.69$ and $k = 1.04 \times 10^{-4}$dl/g. They treated each of the C-shaped chambers as a batch reactor, which is approximate in that chambers "communicate" through gap pressure and drag flows, as discussed earlier. Although Dey and Biesenberger obtained high levels of conversion and high MW reactive extrusion products with some experiments, there were instances of unplanned and unexpected runaway reactions, as well as results that indicated that the rate of the heat generated by the polymerization was appreciably larger than that which can be removed by convective cooling at the barrel surface (see Section 11.2, where, for thematly stable processes, $t_G/t_r < 10^{-1}$). The 34-mm extruder used was air cooled, providing a poor heat-transfer coefficient. Larger extruders would tend to behave more "adiabatically" because of the smaller surface-to-volume ratio, creating more adverse conditions for thermal uniformity and stability inside the reactor vessels that are the C-shaped channels.

Gadzenveld and Janssen (35–38) and Gadzenveld et al. (39) have modeled the fully intermeshing, counterrotating extruder as a reactor, and used it for a number of polymerizing systems with both free radical and condensation-type reactions. Their model considers two extruder reactor zones: partially filled C-shaped chambers upstream, and completely filled chambers downstream, composing the metering zone where pressure is built up against the die pressure. All four leakage flows through the screw-to-screw and screw-to-barrel gaps allow for communication between chambers, and contribute to mixing of reactants. That is, in this zone, the volumetric displacement of the screws is greater than the actual output volume rate, the difference being the backward leakage mixing flows, which affect the chamber flow profiles and, thus, mixing and residence time distribution in each chamber (40). The numerical model of Gadzenveld and Janssen considers all the C-shaped chambers as a series of perfectly mixed continuous stirred tank reactors (CSTRs) "moving on a conveyor belt." The partially filled ones communicate only through drag-induced gap flows. The mass balance in the jth chamber is

$$\frac{dM_j}{dt} = \frac{d(\rho_j \varepsilon V_j)}{dt} = \left\{ Q_{t,i}\rho_{j+1} + 2Q_{f,i}\rho_{j+2} + 2m(Q_{t,i} + Q_{s,i})\rho_{j+2m} \right\} \\ - \left\{ Q_{t,o} + 2Q_{f,o} + 2m(Q_{c,o} + Q_{s,o}) \right\}\rho_j \tag{10.2-15}$$

where V_j is the volume of the jth chamber; ε is the filling degree of the chamber; ρ_j is the density of the material in the jth chamber; and Q_t, Q_f, Q_C, and Q_S are the leakage flows, where subscripts i and o denote inflow or outflow. In the balance, the variation of density during the polymerization reaction can be incorporated. In the model, however, this variation is neglected.

This simple model is schematically represented for single flighted screws in Fig. 10.28. The model is based on the overall balances for enthalpy, mass, and concentration that can be derived for each individual chamber moving through the extruder. Assuming constant density, the preceding equation reduces to

$$\frac{d(\varepsilon V_j)}{dt} = \left\{ Q_{t,i} + 2Q_{f,i} + 2mQ_{c,i} + 2mQ_{s,i} \right\} - \left\{ Q_{t,o} + 2Q_{f,o} + 2m(Q_{c,o} + Q_{s,o}) \right\} \tag{10.2-16}$$
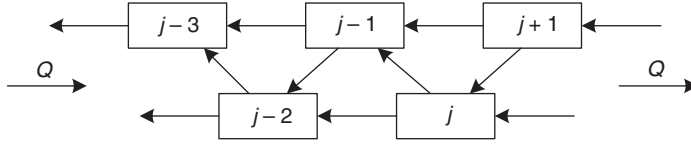
Fig. 10.28 Flow diagram representation of the reaction model of Gadzenveld et al. (39). Each box represents a C-shaped chamber, and the arrows represent the total leak flows from chamber to chamber.

Considering a free radical polymerization, the second relevant balance to the model is that of the monomer concentration over the jth chamber

$$
\begin{aligned}
V_j\varepsilon\frac{dc_j}{dt} = &-\varepsilon V_j\dot{r} + \left\{Q_{t,i}c_{j+1} + 2(Q_{f,i}c_{j+2}) + 2m(Q_{t,i} + Q_{s,i})c_{j+2m}\right\} \\
&-\left\{Q_{t,o} + 2Q_{f,o} + 2m(Q_{c,o} + Q_{s,o})\right\}
\end{aligned}
\tag{10.2-17}
$$

where $\dot{r}$ is the reaction rate and c_j is the concentration of monomer in the jth chamber.

The energy balance is coupled to the monomer concentration balance by the reaction term, as this depends on the monomer concentration and the temperature. The energy balance equals

$$
\begin{aligned}
V_j\varepsilon\rho C_p\frac{dT_j}{dt} = &-\varepsilon V_j\dot{r}\Delta H_r + \rho C_p\Big[\left\{Q_{t,i}T_{j+1} + 2(Q_{f,i}T_{j+2}) + 2m(Q_{t,i} + Q_{s,i})T_{j+2m}\right\} \\
&-\left\{Q_{t,o} + 2Q_{f,o} + 2m(Q_{c,o} + Q_{s,o})\right\}T_j\Big] + hA(T_w - T_j)
\end{aligned}
\tag{10.2-18}
$$

where c_p is the specific heat, ΔH_r the reaction enthalpy, T_j the temperature in the chamber observed, h the heat transfer coefficient, A the heat exchanging surface of the chamber, and T_w the temperature of the wall at the position of the chamber.

The coordinate system is attached to the moving chamber whose velocity, V_c, is the product of the rotational speed, N, and the pitch axial length, L

$$
V_c = NL(x)
\tag{10.2-19}
$$

Thus, the position of the chamber in the extruder is at any time, t

$$
x(t) = N\int_0^t L(x)\,dt
\tag{10.2-20}
$$

and for constant pitch

$$
x(t) = NLt
\tag{10.2-21}
$$

The fully filled length is determined by the die pressure, the viscosity of the reacting material, and the leakage flows. The die pressure is a model input parameter. Speur (41) arrived at an empirical model for the heat transfer coefficient, h, based on an energy balance over a single chamber interacting with its neighbors. Experimental results fitted well with the following relation,

$$
h = 410\left(\frac{N}{0.174}\right)^{1.65-2.3\alpha_r}
\tag{10.2-22}
$$

where h is in watt/cm$^2 \cdot$ K and α_r is the relative throughput, the ratio of the process to the theoretical volumetric rates.

The rheological model used for the reacting stream is that of Stuber (42), based on known empirical generic behavior of polymer solutions. The basis of the model is

$$\eta_0(c, \bar{M}_w, T) = F\xi \qquad (10.2\text{-}23)$$

in which

$$F = K\left[1 + a_1(c\bar{M}_w)^{0.5} + a_2(c\bar{M}_w)\right]^{3.4} \qquad (10.2\text{-}24)$$

and

$$\xi = \exp\left[(b_0 + b_1 c + b_2 c^2)\left(\frac{1}{T} - \frac{1}{T_{\text{ref}}}\right) + b_3 c^3\right] \qquad (10.2\text{-}25)$$

where c is the polymer concentration in weight percent, $\bar{M}_w$ is the weight average molecular weight of the polymer in thousands, K, a_1, a_2, b_0, b_1, b_2, and b_3 are constants, and T and T_{ref} are temperatures in degrees kelvin. The parameter T_{ref} adjusts the concentration dependence of the viscosity model at low concentrations. As T_{ref} decreases, the concentration dependence for low concentrations decreases.

The preceding model is for the zero shear viscosity, η_0. The model does not include the shear rate dependence of viscosity. This is actually not a limiting assumption, since the viscosity changes (increases) with increasing polymer concentration are much greater than those due to shear thinning. The reaction studied was the free radical polymerization of *n*-butyl methacrylate. In the early stages, where a dilute polymer solution represents the reacting material, the polymerization is first order in the monomer concentration. At higher polymer concentrations, the polymer chain mobility becomes limited and the termination steps become *diffusion controlled*, resulting in a reduced combined termination rate constant, k_t. This leads to an increase of free radicals and, thus, loss of steady state due to the increase of the number of propagating chains, which, due to the propagation exotherm, increases the propagation rate constants, leading to the "gel" or Trommsdorff effect (43), where the weight average $\bar{M}_w$ increases to a critical value, $\bar{M}_{\text{wcr}}$. Marten and Hamielec (44) developed an empirical kinetic model based on the free volume theory, leading to the following expression for k_t:

$$\frac{k_t}{k_{t0}} = \left(\frac{\bar{M}_{\text{wcr}}}{\bar{M}_w}\right)^a \exp\left[-A\left(\frac{1}{V_F} - \frac{1}{V_{F_{cr}}}\right)\right] \qquad (10.2\text{-}26)$$

where a is a concentration dependent constant, A is a constant, and V_F is the free volume, which can be calculated by the following equation:

$$V_F = \left[0.025 + \alpha_p(T - T_{gp})\right]\frac{V_P}{V_T} + \left[0.025 + \alpha_m(T - T_{gm})\right]\frac{V_M}{V_T} \qquad (10.2\text{-}27)$$

where the subscripts p and m denote polymer and monomer, and $\alpha = \alpha_l - \alpha_g$, α_l is the expansion coefficient for the liquid state, α_g the expansion coefficient for the

glassy state, T_g the glass transition temperature, V the volume, and V_r the total volume.

The critical free volume is determined by

$$K_3 = \bar{M}_{\mathrm{mer1}}^m \exp(A/V_{Fcr}) \tag{10.2-28}$$

where K_3 is a constant that is dependent on temperature and determined empirically, m is arbitrarily set equal to 0.5, and A is a constant.

The combination of the equations leads, for a bulk polymerization above the glass transition temperature, to a general rate expression:

$$\frac{dx}{dt} = k_p \left(\frac{f_{kd}}{k_{t0}}\right)^{0.5} \frac{(1-x)}{(1-\varepsilon x)} I_0^{0.5} \exp(-k_d t/2) \times \left(\frac{\bar{M}_{\mathrm{w}}}{M_{\mathrm{wcr}}}\right)^a \exp\left(\frac{A}{2}\left(\frac{1}{V_F} - \frac{1}{V_{Fcr}}\right)\right) \tag{10.2-29}$$

where k_d is the reaction constant for the decomposition of the initiator, f is the efficiency factor of the initiator, k_{t0} is the initial termination constant, x is the degree of conversion, ε is the volume contraction factor $(d_p - d_m)/d_p$, d_p is the density of the polymer, d_m is the density of the monomer, I_0 is the initial initiator concentration, and t is the time.

The relationship between the molecular weight and conversion for this polymerization was arrived at empirically, and is approximate, but functional (45)

$$\bar{M}_{\mathrm{w}} = 781 \cdot \text{conversion} - 6500 \tag{10.2-30}$$

The previous two equations enable the solution of the reaction kinetics for the polymerization of n-butyl methacrylate, together with the reaction-specific constants given by the authors (39). The agreement between experimental data and model predictions of this rather simplified CSTR-based model is good, as shown in Fig.10.29(a)–10.29(d).

Counterrotating, Tangential, Nonintermeshing Twin Screw Extruders

Counterrotating, tangential, nonintermeshing (CRNI) TSEs were developed by the Welding Engineers Company (46,47). Their designs were expanded and modified in order to take advantage of their inherent capabilities in the areas of compounding, devolatilization, and reactive extrusion (48–50). Common currently used designs, such as the one shown schematically in Fig. 10.30, exhibit capabilities that have both similarities and differences when compared to single screw and *intermeshing* TSEs (12). Note that one screw is longer than the other, the extra length serving as a single screw melt pump. Also note that, in Fig. 10.30, the flights of the two counterrotating screws are in a *matched*-screw configuration. Figure 10.31 shows the matched-, as well as the staggered-screw configuration, also commonly used because it imparts different process capabilities, as we discuss later. The elementary steps of particulate solids feeding and pressurization, melting, mixing, and devolatilization are all carried out in the twin screw segment of the extruder. Those of melt pressurization and pumping, together with additional laminar shear mixing, are carried out in the downstream, single screw section. The longer screw is equipped on the drive side with a stronger thrust bearing to support the single screw pressure generation used to force the melt through the (pelletizing) die.
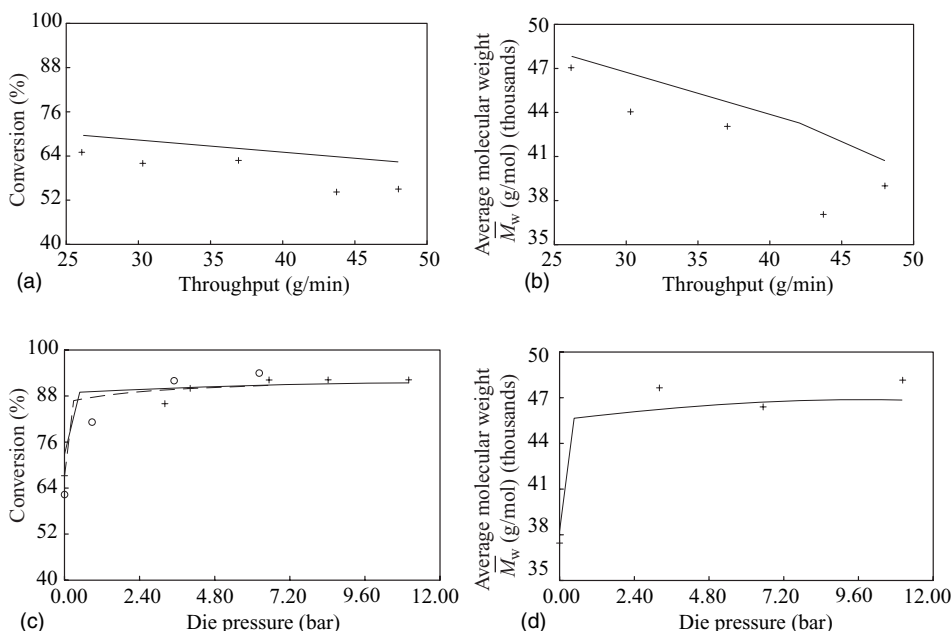
Fig. 10.29   Comparison between the experimental data on the reactive extrusion product of *n*-butyl methacrylate in a counterrotating, fully intermeshing extruder. (a, b) The dependence of conversion and $\bar{M}_w$ on throughput; (c, d) the dependence of conversion and $\bar{M}_w$ on die pressure. (+, O) experimental point, (−) model prediction. [Reprinted by permission from K. J. Gadzenveld et al., "The Modeling of Counterrotating TSEs as Reactors for Single-component Reactions," *Chem. Eng. Sci.*, **49**, 1639 (1994).]

Since the counterrotating screws do not intermesh, axial screw-to-screw tolerance is not critical. This allows CRNI TSEs to be built with very long screws ($L/D \sim 100$), a design feature particularly useful for reactive processing, since the residence time increases, without undue viscous dissipation-generated-melt temperature increase, because the screws are not intermeshing. Relative screw-to-screw timing is also not critical. Thus, the longer screw, which twists, because of the extra shearing forces on the surface of its single-screw portion, more at any given axial position than the shorter, is acceptable. From a screw design
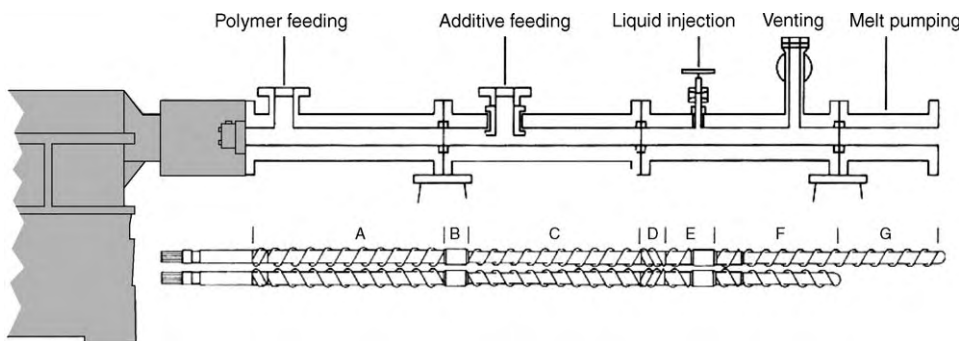

Fig. 10.30   Counterrotating, tangential, nonintermeshing TSE. (Schematic, Courtesy of Welding Engineers.)
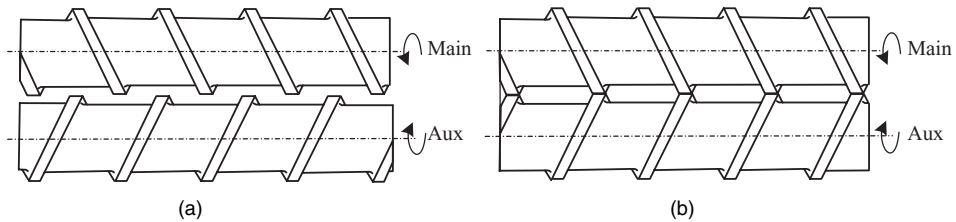
Fig. 10.31 (a) Staggered- and (b) matched-screw flights in a counterrotating, nonintermeshing TSE. The axial offset of staggered is a design variable.

point of view, screw versatility can be obtained by replacing complete shaft segments, connected to others with triple-start threaded screws, rather than individual elements, keyed on polygonal shafts, as in the case with intermeshing, co-rotating TSEs; see Fig. 10.1.

The two apexes, where the two barrel lobes meet, are commonly truncated to promote axial mixing. The truncation ability eliminates some common fabrication and mechanical problems in twin-screw equipment. Finally, tight melt sealing is difficult to achieve, because of the ''open'' design features of the tangential TSEs.

We now discuss the elementary steps of processing as they occur in the twin screw segment of the CRNI tangential extruders; melt pumping in the single screw segment was covered in Chapter 9.

CRNI TSEs are almost always starve-fed to allow for the long lengths needed for mixing, reactive extrusion, and devolatilization. Starve feeding also decouples the feed rate from the screw speed. The needs of multiple feed ports are easy to accommodate because of sufficient equipment length; see Fig. 10.30. The volume available for feeding is quite large because of the tangential positioning of the screws. It is determined by the barrel and screw root diameter and the screw pitch, and, as shown in Fig. 10.32, is greater than that of intermeshing extruders, where it is determined by the centerline-to-diameter ratio, which is less than unity.

The partially filled counterrotating screws advance the free-flowing particulates against the region of the pushing flights by metal–particulate frictional forces. The
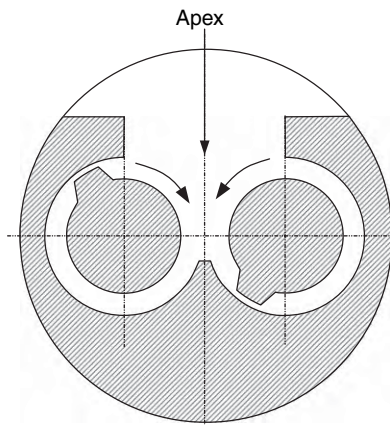

Fig. 10.32 Cross-sectional view of the feed throat region of a CRNI TSE.
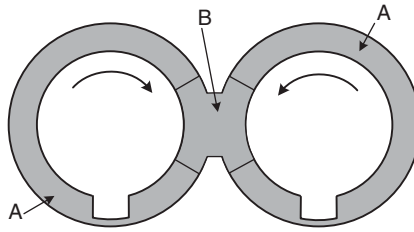
Fig. 10.33   Cross-sectional view of regions in the melting zone of CRNI TSEs where melting mechanisms may be different. [Reprinted by permission from R. J. Nichols and F. Kher-adi, ''Melting in CRT Twin Screw Extruders,'' *Mod. Plast.*, **61**(2), 70 (1984).]

barrel–particulate kinematic friction coefficient, as in the feed zone of SSEs, has to be larger than that between the screw and particulates. There is interchange of particulates at the tangential interscrew plane, which is larger for the staggered than for the matched screw arrays. In both cases, the net flux of such particulates interchange is zero.

The elementary step of melting cannot take place in this partially filled transport zone. These screw segments, which represent flow restrictors, or ''dams''—a pair of cylinders (B), or a pair of reverse screws (D)—are provided in Fig. 10.30. They create a compacted particulate solid bed that can now undergo melting utilizing mechanisms that depend on whether the screw arrays are matched or staggered. The similarity between the single and CRNI TSEs with matched screw arrays in the melting zone is shown schematically in Fig. 10.33 (51). Away from the tangent plane between the two counterrotating screws (regions (A) in Fig. 10.33), the dominant or prevailing melting mechanism is *conductive melting with drag-induced melt removal*, taking place at a molten thin film in the packed-bed barrel region and forming a melt pool, as in SSEs. This is indicated schematically in Fig. 10.34, by the ''herring-bone,'' side-by-side melt pool and packed-bed regions, for the *matched* screw array. On the other hand, in the screw-to-screw tangent region (B) in Fig. 10.33, both the melt and the packed solid beds from the two screws meet, allowing for the possibility of intermixing between the otherwise segregated solid particulates and melt, to form a solids-rich or, further downstream, a melt-rich suspension. If this takes place, then the melting mechanism is *dissipative mix-melting*.
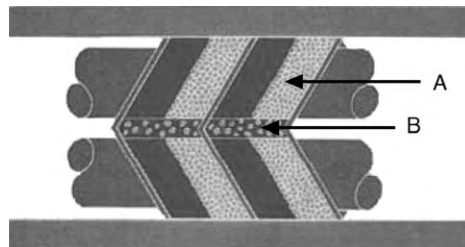

Fig. 10.34   Schematic representation of the two regions in the melting zone of CRNI TSEs with matched screw arrays. In the two regions (A), away from the tangent interscrew plane, the melting mechanism is that of SSEs. In the interscrew plane, a melt–particulates suspension undergoes dissipative mix-melting. [Reprinted by permission from R J Nichols and F. Kher-adi, ''Melting in CRT Twin Screw Extruders,'' *Mod. Plast.*, **61**, 70 (1984).]
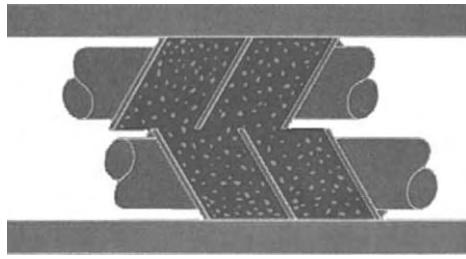
Fig. 10.35 Idealized representation of the solid–melt suspension formed in the melting zone of CRNI twin extruders with staggered screw arrays. The mechanism of melting will be dissipative mix-melting. [Reprinted by permission from R. J. Nichols and F. Kher-adi, "Melting in CRT Twin Screw Extruders," *Mod. Plastics*, **61**(2), 70 (1984).]

Nichols and Kher-adi (51), conducting screw-pushing carcass analysis melting experiments, observed that the dominant mechanism in a matched-screw array, CRNI extruders resulted in a segregated melt pool and packed particulate beds, as is the case in SSEs. They, however, observed shorter melting lengths than in single screws with the same design and processing conditions. They attributed this to the contributions of the mix-melting mechanism in region (B). When examining the carcasses obtained from the melting zone with *staggered* screw arrays, they found that no coherent and segregated melt pool was formed. Rather, they observed interspersed regions of melt and particulates, represented in an idealized fashion in Fig. 10.35. It is reasonable that such a suspension forms with staggered screw arrays. The mechanism may be as follows: initially, melting of the compacted particulate beds in both screws occurs by conductive heating with drag-induced melt removal. This results in a molten film and the formation of a small melt pool in each screw by the scraping of the pushing flights. These pools meet the packed bed of the opposite screw, setting conditions for the formation of a solids-rich suspension in both flights, leading to dissipative mix-melting. This mechanism is driven by the viscous energy dissipation of the molten phase and deformation of solids, as well as conductive heating of solids. These are all due to the flow in the filled-channel regions (A) and (B), with material transferred from screw to screw because of the stagger, and leakage flow in the truncated barrel apex. Satija and Tucker (52) also observed dissipative mix-melting over a range of processing conditions.

Kaplan and Tadmor (53) (see Section 6.8) were the first to develop a theoretical model for melt conveying in the tangential, nonintermeshing twin screw pump. Their simplified "three parallel plate" model has two continuous plates representing the two stationary screws (since the observer is on them), on either side of a series of moving, slitted mid plates, as shown in Fig. 6.56. The slits represent region (B) and the interrupted plates, region (A) in Fig. 10.33. Nichols (54) conducted melt-conveying experiments with matched and staggered screw arrays, in a 2-in CRNI extruder using dimethylsiloxane, and found that the three parallel plate model overestimates the throughput rates of both staggered and matched arrays. He attributed this to the truncated barrel apexes, which allow back-leakage flows. Figure 10.36 shows the screw characteristic operating lines for staggered and matched arrays and for two different channel depths and two different values of f, the fraction of closed barrel, that is, a measure of the degree of apex truncation. Staggered arrays with open transverse and down-channel, screw-to-screw configuration have limited pressurization capabilities compared to the matched screw characteristics.
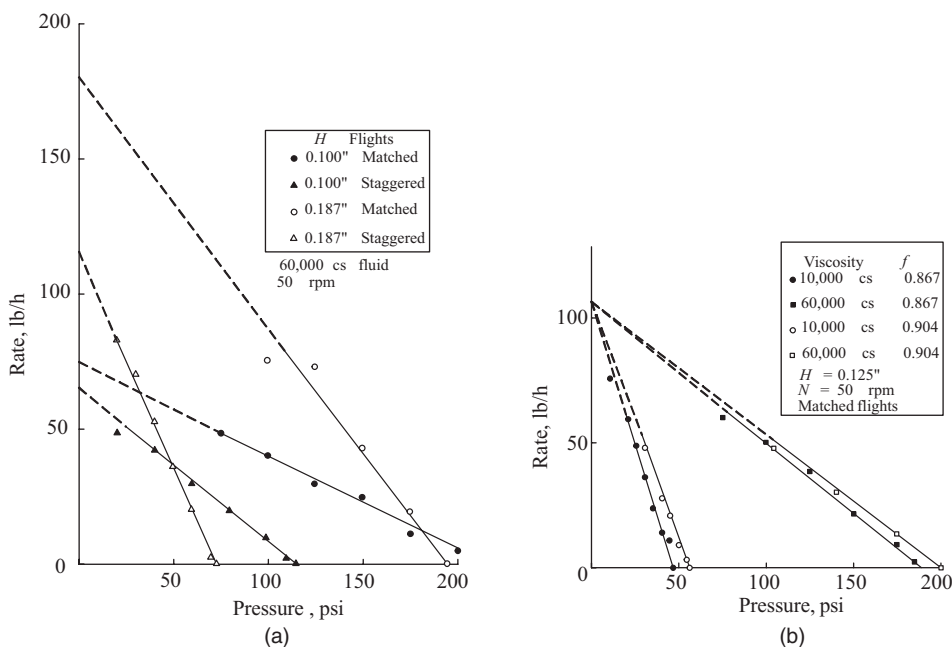
Fig. 10.36 Experimental screw-characteristic operating lines for a 2-in CRNI staggered and matched-screw array at room temperature using polydimethlsiloxane. (a) Comparison of the pumping capabilities of staggered and matched arrays at two different channel depths, *H*. (b) The effect of the fraction of closed barrel, *f*, on the matched-array screw characteristics for two fluid viscosities. [Reprinted by permission from R. J. Nichols, ''Pumping Characteristics of Counter-rotating TSEs,'' *SPE ANTEC Tech. Papers*, **29**, 130 (1983).]

Both staggered and matched screw characteristics show increased sensitivity with increasing channel depth, as expected. Figure 10.36(b) demonstrates the significance of the barrel apex truncation in allowing leakage backflows in this region.

Improved fluid mechanical models to better fit the experimental data were proposed by Nichols (55) and by Nguyen and Lindt (56), the latter being an FEM two- and three-dimensional model, achieving good fit with experimental results. More recently, Bang et al. (57) and, as previously referred to, Li and Manas-Zloczower (31) as well as Katziguara et al. (32) have developed three-dimensional FEM solutions of fully filled CRNI flight channels. As in the fully intermeshing full channels discussed earlier, Li and Manas-Zloczower tracked the evolution of particles fed continuously and steadily in the hopper of melt filled, thin-flighted, matched CRNI screw-array channels. They found that distributive mixing is efficient, resulting in uniform quasi-steady state particle distributions, such as the one shown in Fig. 10.37 at an axial cross section.

Bang et al. (57) conducted experiments with a 34-mm Leistritz LSM tangential CRNI extruder using LDPE with Power Law constants $m = 3200 \text{Pa} \cdot \text{s}^n$ and $n = 0.45$ at 180°C. The extruder was outfitted with several pressure transducers. Additionally, screw-pulling experiments were carried out to determine the filled length upstream of the die, and three-dimenasional FEM isothermal flow simulations were carried out. In general, the agreement between computational and experimental results was good. The screw melt conveying segments shown in Fig. 10.38 were studied. The screw characteristic curves for
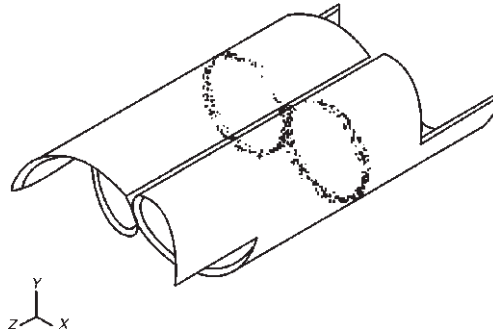
Fig. 10.37   Cross-sectional view of a quasi-steady state distribution of particles in thin-flighted tangential CRNI channels. From such distributions, several measures of distributive mixing can be computed. [Reprinted by permission from T. Li and I. Manas-Zloczower, "A Study of Distributive Mixing in Counterrotating TSEs," *Int. Polym. Process.*, **10**, 314 (1995).]

these elements were plotted in terms of the dimensionless flow rate, Q^*, and channel pressure gradient $(\Delta P/L)^*$, where

$$Q^* = \frac{Q}{(2\pi N R_b) R_b^2} \tag{10.2-31}$$

$$(\Delta P/L)^* = \frac{(\Delta P/L) R_b}{m(2\pi N)^n} \tag{10.2-32}$$

Figure 10.39 depicts the dimensionless screw-characteristic curves for the thin and thick, forward conveying screw array channels. Included, for comparison, are the simulated curves, which indicate good predictive agreement with the experimental results. The pressurization capability of the matched arrays is about three times that of the staggered arrays for the thin-flighted, and about twice for the "tighter," thick-flighted arrays. Furthermore, as expected from the existence of restricted flow paths, the melt-conveying pressure sensitivity of the thick-flighted channels is appreciably smaller than that in the thin-flighted channels.

As mentioned in Section 10.1, the counterrotating, the fully intermeshing, the thin-flighted intermeshing, and the nonintermeshing TSEs are all low-energy input devices. The first, because the calendering gap tightness limits the rotational speed to the range of 100–150 rpm, and the second and third because of the existence of open channels, which
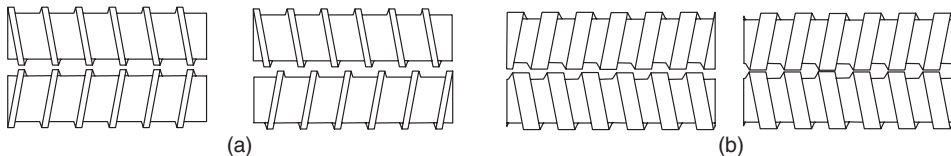

Fig. 10.38   The examples of Leistritz melt conveying, modular CRNI screw elements studied by White and associates. (a) Thin flighted forward matched and staggered; (b) thick-flighted, reverse matched and staggered. [Reprinted by permission from D. S. Bang, M. H. Hong, and J. L. White, "Modular Tangential Counterrotating TSEs: Determination of Screw Pumping Chararacteristics and Composite Machine Behaviour," *Polym. Eng. Sci.*, **38** 485 (1998).]
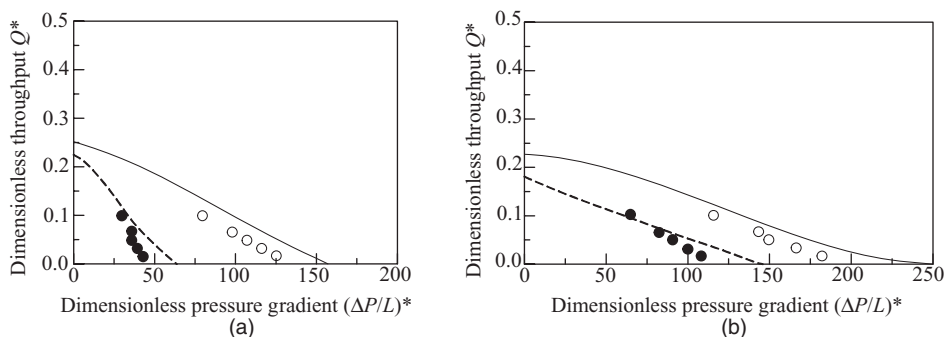
Fig. 10.39 Dimensionless screw-characteristic curves for forward melt-conveying, tangential CRNI modular segments in matched and staggered configurations. (a) Thin-flighted screws; (b) thick-flighted screws; (●) for staggered; (○) for matched. [Reprinted by permission from D. S. Bang, M. H. Hong, and J. L. White, "Modular Tangential Counterrotating TSEs: Determination of Screw Pumping Chararacteristics and Composite Machine Behaviour," *Polym. Eng. Sci.*, **38**, 485 (1998).]

result in weak stress fields, even at high rotational speeds, but strong distributive flow fields.

Thiele (7) and Martin (58) discuss a new class of counterflight melting and mixing elements which impart mechanical energy at levels which are comparable to the kneading elements in co-rotating, intermeshing, self-wiping TSEs. In 'counterflight' elements, energy is dissipated by deforming or forcing squeezing flows in lobes, whose cross-sectional areas are in constant periodic change because of the counterrotation. Figure 10.40 demonstrates this point. The bilobal kneading element pair shown in Fig. 10.11 is functional only with co-rotating shafts. On the other hand, the modified bilobal pair in Fig.10.40 can operate in both co- and counterrotating modes. If the number of lobes is increased, as shown schematically by the cross-sectional view of a hexalobal pair of mixing elements, it can operate only in counterrotation.

To allow for high speeds of 300–500 rpm, open-flighted elements are utilized to drag polymer melts over their flights. Thus, the number of interlobal mixing events taking place in hexalobal elements, which is the product of the number of lobes and the rotational speed, is very large. Indeed, versatile hexalobal designs, such as that shown in Fig. 10.41, make excellent distributive and dispersive mixing elements. Such counterflight elements can be used in conjunction with traditional counterrotating segments, but with wider calender gap clearances to allow for higher rotational speeds (58). There are no reported FEM simulations in the literature to describe the flow in fully filled counterflight multilobal element channels.

The Continuous Mixer

The principal characteristics of the CM were discussed briefly in Section 10.1, and discussed in detail by Valsamis and Canedo (59). The CM is a counterrotating, nonintermeshing twin rotor device that affects rapid and efficient melting and mixing of single- or multicomponent polymer systems. The rotors are supported at both ends by conventional bearings. At the feed end, the bearing is isolated from the particulate charge
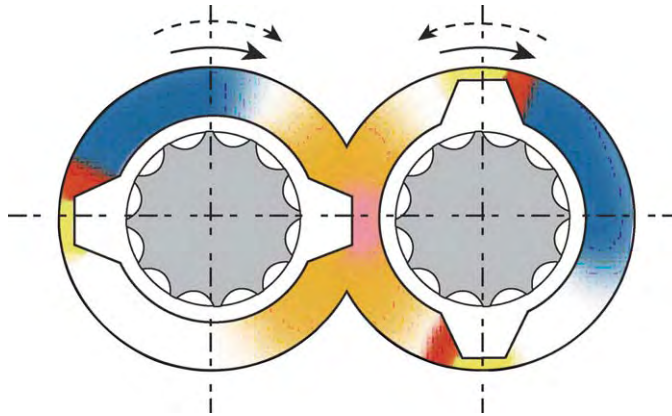
Fig. 10.40   A pair of bilobal elements that operate either in co- or counterrotation and impart mechanical energy in deforming solids or forcing flow in melts filling the available interelement volume. The shear intensity is depicted by the color code going from white to red with increasing intensity. [Courtesy of C. Martin, American Leistritz Extrusion Corp.]
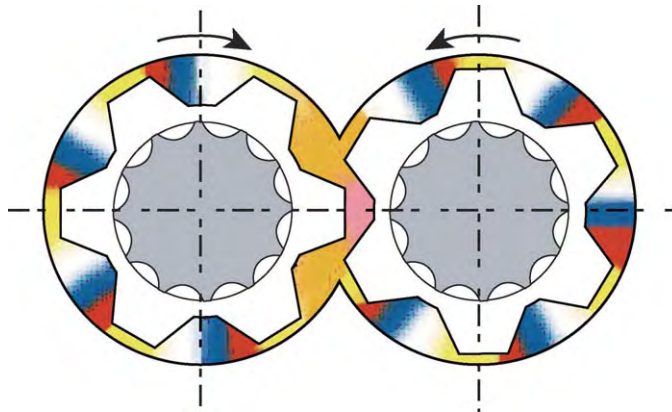

Fig. 10.41   Cross-sectional view of a pair of hexalobal mixing elements of counterrotating, intermeshing TSEs. [Courtesy of C. Martin, American Leistritz Extrusion Corp.]

with a powder (labyrinth) seal, and at the discharge end with a dynamic melt seal.[7] Rotors are drilled for circulating cooling fluid. Short single-flighted or double-flighted screws, which extend upstream from the hopper opening, deliver the material in starve–fed, controlled mass-flow rate fashion to the mixing chamber. The rotors, shown in Fig. 10.6, are made of two helically twisted wings, approximately 180° apart, with the wings of each rotor twisted in opposite directions. Each wing has a forward and a backward (reverse) pumping section, the reverse being shorter and often twisted by a slightly different angle, in order to provide for forward net pumping. The apex of a wing is offset from the apex of the complementary wing of the same rotor and from the wings of the other rotor. The rotors are housed in cylindrical enclosures, the chamber halves, which communicate with

7. The dynamic seal is a reverse extruder created by machining small multiple-screw channels onto the rotor end rotating in the closed housing. Because of the helix angle, they will pump melt back into the mixing chamber.

each other along the entire mixing chamber. Feed and melt discharge openings are located at the intersection of the chamber halves.

Solids conveying is carried out by the two counterrotating, short starve–fed screws, which are double-flighted in large-size melters/mixers to accommodate high feed rates, often of low bulk density feeds. Particulates are in a moderately fluidized state and are dragged forward by barrel–particulate frictional forces. Screw cooling is important to avoid increased frictional (adhesive) forces between the screw walls and particulates. CMs are effective melters, yet there is only limited published research on the melting mechanisms in these machines. However, based on their high rates of melting, one can surmise that they must employ one or more high mechanical energy dissipating mechanisms of frictional, plastic, and viscous energy dissipation (FED, PED, and VED, respectively), as discussed in Section 5.8. This conclusion is qualitatively substantiated by Valsamis and Canedo (59), who presented the only experimental melting investigation in a full mixing-chamber 2-in-diameter FCM, by carrying out carcass analysis of a 50:50 LDPE/PE immiscible blend.

Example 10.1   Elements of a Plausible Melting Mechanism in Continuous Mixers
The Valsamis–Canedo experiments (60) revealed that extensive melting occurs rather early in the mixing section. Clearly, the energy dissipated at the entrance region of the mixing section is large enough to fuse and partly melt the particulates. This can only be accomplished by the two melting mechanisms that involve polymer particulates, namely FED and PED. It appears, therefore, that the solids are dragged by the rotors toward the converging entrance regions of the "leading faces" of the rotors, the rolling pool regions of Fig. E10.1, where they get compressed and sheared. When they reach the rotor wing-tip clearance region, these compressed particulates are forced to undergo shear deformation at a high rate of the order of $\dot{\gamma}_{app} \sim \pi D_{max}/h$, where h is the wing tip–barrel clearance and D_{max} is the wing tip rotor diameter.

Next we assume that the particulate solids at the beginning of the mixing chamber fill the "rolling pool" until the point of the minimum rotor diameter. The maximum degree of particulate bed densification and compaction, as it is forced through
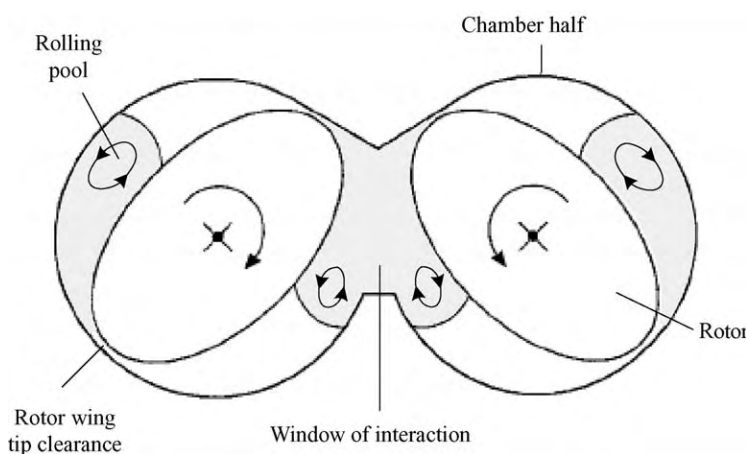

Fig. E10.1   Cross section of the mixing chamber of an FCM, identifying the regions of deformation and flow that are responsible for melting and mixing.

the converging region, is h/H_0, where H_0 is the maximum and h is the minimum clearance between the barrel and the rotors. Typically, $h/H_0 \sim 10^{-1}$, while the ratio of the particulate solid bulk density to the density of the monolithic solid polymer, the densification measure, is $\rho_b/\rho_s \sim 0.5$. Thus, it is reasonable to assume that a rather significant compressive, squeezing particulate deformation may occur in this region. It follows, then, that PED may at least be operative in deforming and softening the contact regions from particulate to particulate throughout the bed, thus increasing their effective friction coefficient.

In addition, shear deformation is imposed on the particulate bed in the converging rolling pool region. Shear deformation of compressed particulates will result in the creation of velocity differences between adjacent particles. For simplicity, let us consider the shear deformation at the rotor wing tip clearance region. Each particle is subjected to a normal force by its neighbors, F_N, due to the bed compression. The velocity difference between the moving rotor wing-tip surface and the stationary barrel is $\pi D_{max}N$. Assuming a linear circumferential velocity profile, the difference in velocity of one circumferential layer of particles to the next one in the radial direction is

$$\Delta v = \pi D_{max} N \left(d_p / h \right) \tag{E10.1-1}$$

where d_p is the average particulate diameter, and $d_p/h \sim 10^{-2}$.

Thus, the power dissipated locally by FED is of the order of

$$\dot{W}_{FED} \sim \pi D_{max} N \left(d_p / h \right) f F_N \tag{E10.1-2}$$

where f is the interparticle friction coefficient. No investigation has yet been made of the roles of PED and FED in the initiation of the rapid volumewise melting in CMs. We believe, based on the physical arguments previously presented, that both PED and FED contribute to the melting mechanisms operating at the beginning of the mixing chamber; of the two, FED will most likely be the dominant one. Together, they apparently produce enough melt to create a solids-rich suspension immediately downstream, which undergoes vigorous dissipative mix-melting in the ''window of interaction'' region, where complex circumferential, radial rotor-to-rotor, and axial flows, due to the opposing wing-tip twists, take place. In this region, however, not only does dissipative mix-melting take place, but also effective distributive mixing due to the prevailing chaotic flows.

At this juncture it is important to note the rather profound difference between an SSE with L/D values of 22–36, and those continuous mixers with L/D values of 5–10. In the former, which operates at lower frequencies of rotation, the elementary steps of processing occur in a more sequential fashion, with only partial overlap, while in continuous mixers, which operate at higher frequencies of rotation, there is significant overlap and concurrence of elementary steps along most of the axial length. This attribute enables CMs to be rapid and efficient melting and mixing twin rotor devices, but renders the development of theoretical models for their functioning more difficult.

Another difference between the extruders and continuous mixers, pointed out by Valsamis and Canedo, is that, in the former, channel solids and melt flow dominate, and flow over screw flights is a secondary effect (except for power calculations). In contrast, the circumferential flow in CMs (and internal mixers) over the wing tips is the *major* flow component. Thus, while wing tips and screw flights appear to be equivalent machine elements, their role and function are quite different. The wing tips provide high shear
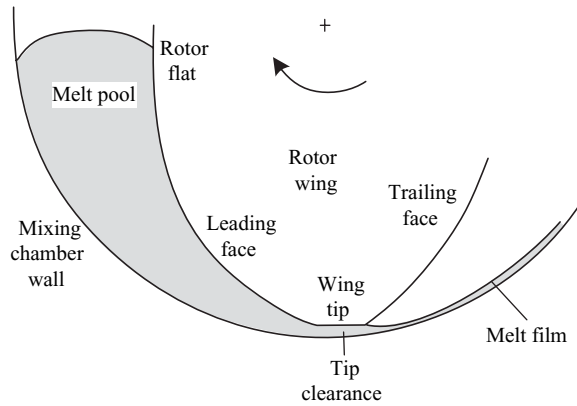
Fig. 10.42   Cross-sectional view of the CM mixing chamber near one of the rotor-wing sections, identifying relevant flow regions and mixer design parameters.

stress regions for the melt to repeatedly pass over circumferentially and, because of their helical twists, force axial circulation. On the other hand, continuous mixers, with their "window of interaction" region promoting rotor-to-rotor interaction and material interchange, are similar to most of the other TSEs, whether co- or counterrotating, as pointed out in Section 10.1.

Wedge Flow Analysis

Considerable research attention has been focused on circumferential flow simulation in narrowing gap wedge-type geometries characteristic to batch and continuous mixers, as well as to mixing regions of TSEs, shown schematically in Fig. 10.42. Bolen and Colwell (61) and Bergen (62) presented early analyses, and Meissner, et al. (63,64) and Wagenknecht et al. (65), were the first to use the lubrication approximation for the calender-like wedge-dynamic pressurization flows involved for non-Newtonian melts in nonisothermal flows. Kim and White used a modified flow-analysis network (FAN) (66) and Cheng and Manas-Zloczower (67,68) and Wong and Manas-Zloczower (69), a two-dimensional FEM model, which, for computational necessity, can only describe *full* mixing chambers.

In this section, we present a simple, one-dimensional lubrication approximation analysis, assuming isothermal conditions and Newtonian melts, along the lines of Section 6.4, dealing with non-parallel plate dynamic pressurization applications with knife coating, calendering, and two roll-mill flows (59). Such analysis, in spite of its simplicity, gives good insight and provides analytical results. Moreover, the lubrication approximation with common CM rotor-design approach angles of 10–20° results in relatively minor errors (5–10%), and the effect of shear thinning can be estimated and taken into account.

The cross-sectional view of the CM mixing chamber in the rotor-wing section is shown schematically in Fig. 10.42. The gap between the rotor and the chamber wall varies from the minimum gap, h, to the maximum gap, H_0, given, respectively, by

$$h = \frac{1}{2}(D_0 - D_{\max}) \qquad (10.2\text{-}33)$$

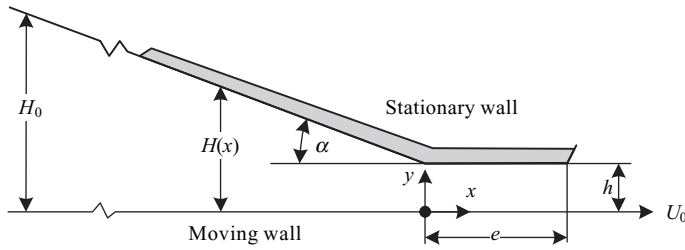$$H_0 = \frac{1}{2}(D_0 - D_{\min}) \qquad (10.2\text{-}34)$$

Fig. 10.43   Linear wedge model of the mixing chamber near a wing tip.

where D_0 is the mixer-section barrel diameter, D_{max} the rotor diameter at the wing tip, and D_{min} the diameter at the rotor flat. In the wing tip vicinity, the flow field geometry can be approximated by a wedge at an angle α, the leading face wedge angle, and a parallel plate wing tip clearance, as shown in Fig.10.43. The wedge spacing H, with the stationary coordinate system placed at the entrance to the wing tip, is given by

$$H = \begin{cases} h - x\tan\alpha & -E_0 < x < 0 \\ h & 0 < x < e \end{cases} \tag{10.2-35}$$

where

$$|E_0| = \frac{H_0 - h}{\tan\alpha} \tag{10.2-36}$$

The drag of the moving wall in the wedge section builds up pressure, which is then lost over the parallel plate section. We now derive expressions for the flow rate in the tip region and its dependence on wedge geometry and the velocity fields in the wedge region.

For incompressible isothermal flow of a Newtonian fluid, making the lubrication approximation and the no-slip condition, the equations of continuity and motion become

$$\frac{dv_x}{dx} + \frac{dv_y}{dy} = 0 \tag{10.2-37}$$

$$\frac{dP}{dx} = \mu \frac{\partial^2 v_x}{\partial y^2} \tag{10.2-38}$$

with the boundary conditions $v_x(0) = \pi N D_0 = U_0$ and $v_y(0) = 0$ for all x, and $v_x(H) = v_y(H) = 0$ for $-E_0 < x < 0$ and $v_x(h) = v_y(h) = 0$ for $0 < x < e$. Pressure at planes $x \le -E_0$ and $x \ge e$ is zero (atmospheric).

In the parallel plate wing tip region, in terms of the pressure and drag flows per unit width, we obtain (see Example 2.5 and Section 6.3)

$$q = \int_0^h v_x(0, y)\, dy = (q_d + q_p) \tag{10.2-39}$$

where q_d and q_p are the drag and pressure flows per unit width, respectively. The drag flow is given by

$$q_d = \frac{1}{2} U_0 h \tag{10.2-40}$$

and by defining $G_N = q_p/q_d$, we can write Eq. 10.2-39 as

$$q = \frac{1}{2} U_0 h (1 + G_N) \tag{10.2-41}$$

Solving for the velocity components in the wedge region, we obtain

$$v_x = \left[1 - 3 \left(1 - (1 + G_N) \frac{h}{H} \right) \frac{y}{H} \right] \left(1 - \frac{y}{H} \right) U_0 \tag{10.2-42}$$

and by using the equation of continuity, given in Eq. 10.2-37, we can derive the following expression for the v_y component:

$$v_y = \tan \alpha \left[2 - 3(1 + G_N) \frac{h}{H} \right] \left(1 - \frac{y}{H} \right) \left(\frac{y}{H} \right)^2 U_0 \tag{10.2-43}$$

By inserting Eq. 10.2-42 into Eq. 10.2-38, we obtain the pressure fields in the wedge region

$$P(x) = \frac{3\mu U_0}{h} \cot \alpha \left[2 - (1 + G_N) \left(\frac{h}{H(x)} + \frac{h}{H_0} \right) \right] \left(\frac{h}{H(x)} - \frac{h}{H_0} \right) \tag{10.2-44}$$

and, in the tip region (see Example 2.5) we obtain

$$P(x) = \frac{6\mu U_0 G_N}{h^2} (e - x) \tag{10.2-45}$$

Equations 10.2-44 and 10.2-45 are equal at $x = 0$, where $H(x) = h$, which yields

$$G_N = \frac{(1 - h/H_0)^2}{1 + 2(e/h) \tan \alpha - (h/H_0)^2} \tag{10.2-46}$$

Thus, we find that, for Newtonian fluid, the pressure-to-drag-flow ratio in the tip region is dependent only on geometric variables. Valsamis and Canedo (59) point out that, for most of the practical designs, $0.25 < G_N < 0.50$, that is, the wedge dynamic pressurization increases the flow rate over the wing tip by 25–50%.

Turning to the velocity fields, we can find from Eq. 10.2-42 that v_x is zero at

$$\frac{y}{H(x)} = \frac{1}{3 \left[1 + (1 + G_N) \frac{h}{H(x)} \right]} \tag{10.2-47}$$

From this equation, by setting $h = H(x) = H_S$ we obtain the stagnation point

$$H_s = \frac{3}{2} (1 + G_N) h \tag{10.2-48}$$

shown in Fig. 10.44. Thus, for $H < H_s$, we find that in both Regions I and II, the melt moves forward in the positive x direction. However, for $H > H_s$, we find Region III near
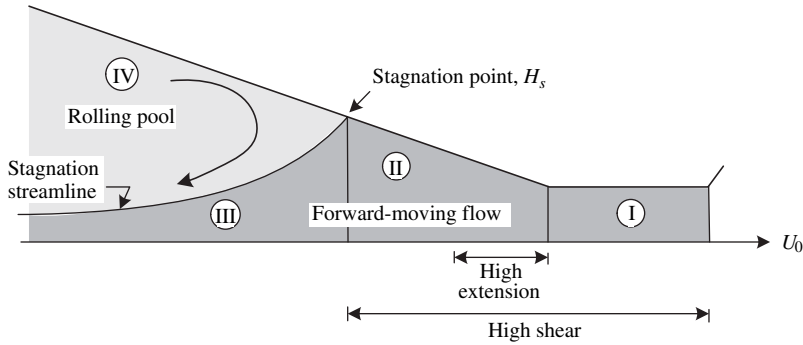
Fig. 10.44 Flow regions in the model wedge.

the moving wall, in which the melt also moves forward, and above it we find Region IV with a rolling, circulating melt pool. Thus, a stagnation streamline exists, as indicated in Fig. 10.44, $y = y_s(x)$, which can be evaluated by recognizing that the flow rate in Region III must equal q, the flow rate over the wing tip parallel plate Region I. Thus, the *net* flow in the rolling pool is zero, and thus

$$\int_{ys(x)}^{H(x)} v_x \, dy = 0 \tag{10.2-49}$$

Substituting Eq. 10.2-42 into Eq. 10.2-49 yields

$$y_s(x) = \frac{\frac{1}{2}(1 + G_N)h}{1 - (1 + G_N)[h/H(x)]} \tag{10.2-50}$$

The v_x component of the velocity field along the streamline can be obtained by substituting Eq. 10.2-50 into 10.2-42, to give

$$v_s = v_x|_s = \frac{1 - \frac{3}{2}(1 + G_N)(h/H)^2}{1 - (1 + G_N)(h/H)} \tag{10.2-51}$$

The $v_x(y)$ velocity profiles for Regions III and IV are shown in Fig. 10.45. Using Eq. 10.2-43, we can compute the whole velocity field and plot the velocity vector field. However, we must recall that the model assumed the lubrication approximation and neglected all acceleration and inertia effects.

Turning to the pressure profile $P(x)$ given in Eq. 10.2-44, we note that it reaches a maximum value of

$$P(x)|_M = \frac{3\mu U_0}{(1 + G_N)h} \cot \alpha \left[1 - (1 + G_N)\frac{h}{H_0}\right]^2 \tag{10.2-52}$$

at the axial location corresponding to H_M, where
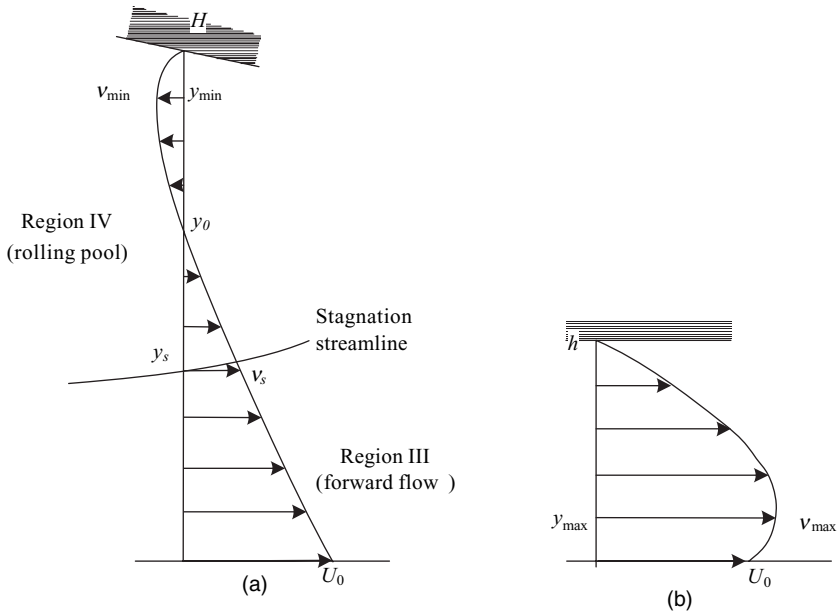
$$H_M = (1 + G_N)h \tag{10.2-53}$$

Fig. 10.45 The velocity profiles $v_x(y)$. (a) For Regions III and IV; (b) for Region I.

The dimensionless pressure profile is plotted against the dimensionless x direction in Fig. 10.46. Note that the maximum value is attained upstream of the parallel tip section, and $P(x)$ is the only parameter that can be measured with relative ease in an FCM by placing a transducer at the mixer section of the barrel wall. Valsamis and Canedo (59), working with HDPE and a non-Newtonian melt being processed in 4-in-diameter FCM, reported qualitative agreement with the predictions, and the same order of magnitude of the maximum pressure given by Eq. 10.2-52.
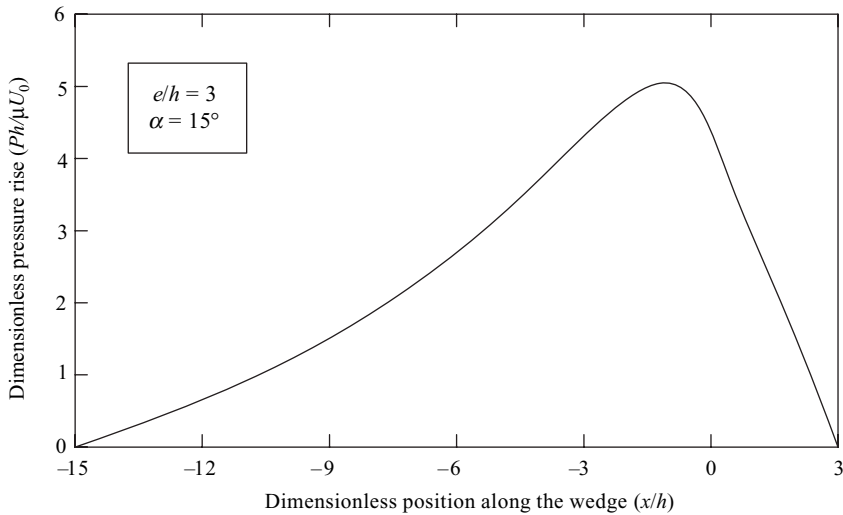

Fig. 10.46 The dimensionless pressure profile developed in Regions I–IV by dynamic drag pressurization.

In addition to the Newtonian fluid, Valsamis and Canedo (70) also used the Carreau constitutive equation to solve the continuity equation (Eq. 10.2-37) together with the following form of the equation of motion

$$\frac{dP}{dx} = \frac{\partial}{\partial y} \left(\frac{\eta_0}{\left[1 + (\lambda \dot{\gamma}^*)^2 \right]^{\frac{1-n}{2}}} \right) \tag{10.2-54}$$

where, for computational simplicity, they used the Newtonian shear rate $\dot{\gamma}^*$ obtained by differentiating v_x with respect to y, Eq. 10.2-42,

$$\dot{\gamma}^* = \left| 1 - 3\left[1 - (1 + G_N)\frac{h}{H} \right]\left(1 - \frac{2h}{H} \right) \right| \frac{U_0}{H} \tag{10.2-55}$$

obtained the numerical solution and non-Newtonian $G = q_p/q_d$ values shown in Fig. 10.47. Valsamis and Canedo found that the non-Newtonian $G = q_p/q_d$ parameters, when used with the Newtonian expressions for the pressure, $P(x)$. Equations 10.2-44 and 10.2-45, give results that agree more closely with experimentally obtained $P(x)$ data.

The preceding computational model was extended to allow for nonisothermicities, through the use of the Carreau–Yasoda model (71)

$$\eta = \frac{\eta_0 e^{-\beta(T - T_R)}}{\left[1 + (\lambda \dot{\gamma})^2 \right]^{(1-n)/2}} \tag{10.2-56}$$

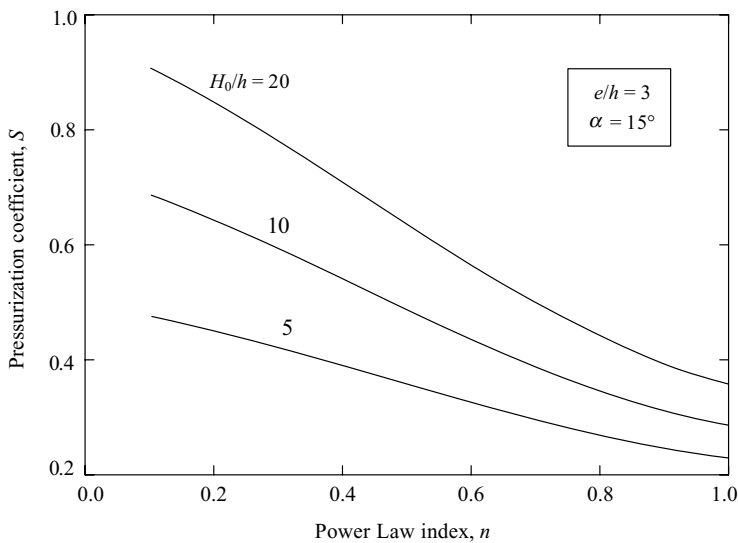**Fig. 10.47**   The effect of the Power Law index in the Carreau model, and the melt-pool size for a characteristic model wedge with $e/h = 3$ and $\alpha = 15°$ on the non-Newtonian q_p/q_d parameters. [Reprinted by permission from L. N. Valsamis and E. L. Canedo, "Mixing in the Farrel Continuous Mixer" in *Mixing and Compounding of Polymers*, I. Manas-Zloczower and Z. Tadmor, Eds., Hanser, Munich, 1994.]
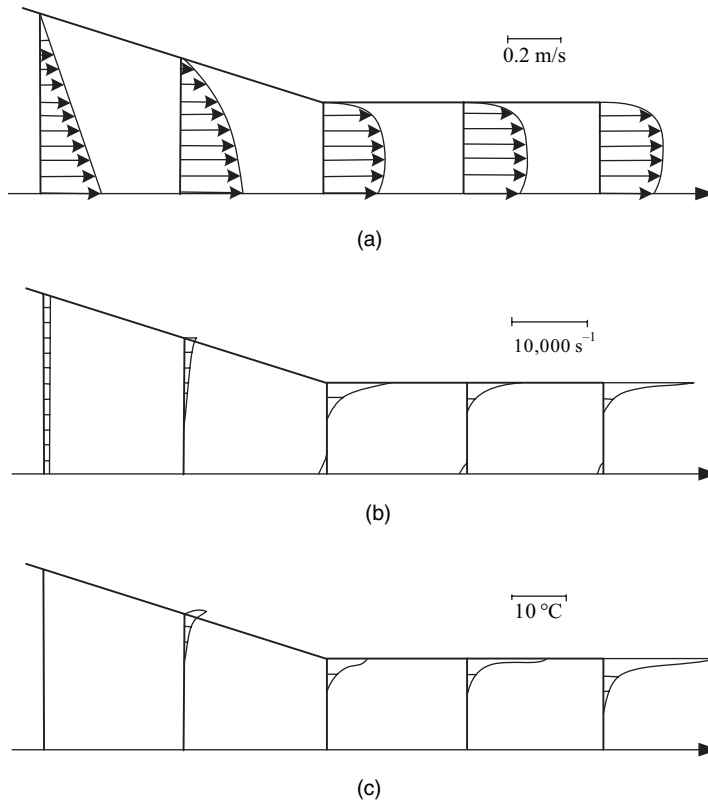
(a)

(b)

(c)

Fig. 10.48 Numerical simulation results of nonisothermal flow of HDPE, Melt Flow Index MFI = 0.1 melt obeying the Carreau–Yagoda model for a typical FCM model wedge of $e/h = 3$ and = 15. (a) Velocity; (b) shear rate; and (c) temperature profiles [Reprinted by permission from E. L. Canedo and L. N. Valsamis, ''Non Newtonian and Non-isothermal Flow between Non-parallel Plate – Applications to Mixer Design,'' *SPE ANTEC Tech. Papers*, **36**, 164 (1990).]

The equations of continuity, motion, and energy, using the constitutive equation (Eq. 10.2-56), were solved numerically only for Regions I and II, where most heat is generated, invoking the lubrication approximation, and assuming that conduction takes place only in the y (radial) direction and that there is no convective heat transfer. The boundary conditions used were an adiabatic rotor and constant chamber temperature. Calculated results are shown in Fig. 10.48. The results indicate very large shear rates, but a moderate temperature rise, due to VED in the melt layer occupying one-third of the tip clearance closest to the rotors, because of the short residence time. Such results are important for the estimation of the total shaft energy converted into heat in the axial section of the mixing chamber, which is partially filled with polymer melt, and not the first upstream part, where melting occurs.

The original CM was extended by a number of polymer processing equipment manufacturers to include in-line, axial, two single screw pressurization and melt pumping elements feeding a gear pump. The advantage of the axial discharge continuous mixer over CMs is, of course, pressurization capability, while the drawbacks are the loss of the discharge bearing and the ability to cool the rotors. The loss of the discharge support

bearing can become limiting, especially for large size, high capacity, postreactor finishing applications.

The two counterrotating rotors in the mixing chambers are under dynamic forces which are due, on the one hand, to the hydrodynamic separating forces generated in the region of the window of interaction, which are largest in the transition region from the feed screws to the mixing chamber, and, on the other hand, the lubrication hydrodynamic lift forces generated at the wedge and tip clearance regions, which oppose the separating forces to degrees that depend on the rotor orientation and the wing tip helical twist. Under these two opposing forces, as well as their own weight, the two rotor shafts respond in a dynamic deflection mode, which may become the cause of metal-to-metal contact and wear, especially between the screws and barrels in the dual, single screw discharge pumps.

The dynamic analysis of the shaft deformation problem requires the simultaneous solution of the real fluid mechanical problem, that is, a partially filled mixing chamber with an axially changing solids content, and the solid mechanics problem of deformation of the variable cross-section, counterrotating shafts. This is not feasible at this time, because of the inability of FEM CFM schemes to handle these partially filled chamber flows. Although not examined, this problem can be addressed by combining the full mixing chamber fluid mechanical simulations, such as by Manas-Zloczower (67–69,72) and Ishikawa et al. (73), with the solid mechanics shaft deformation CAD packages. On the other hand, Ishikawa et al., as part of the series of three-dimensional FEM investigations, obtained numerical results on the velocity, temperature, and pressure fields of the second stage of the LCM 100G, a 100-mm barrel diameter CM, developed by Kobe Steel. The LCM 100G and the second-stage rotors are shown schematically in Fig. 10.49. Since the second stage is usually operated *almost filled*, the FEM simulation results, which hold only for filled mixer chambers, are quite relevant. For this reason, they compare them with experimentally obtained pressure and temperature results on the actual mixing chamber barrel at positions shown in Fig. 10.50.
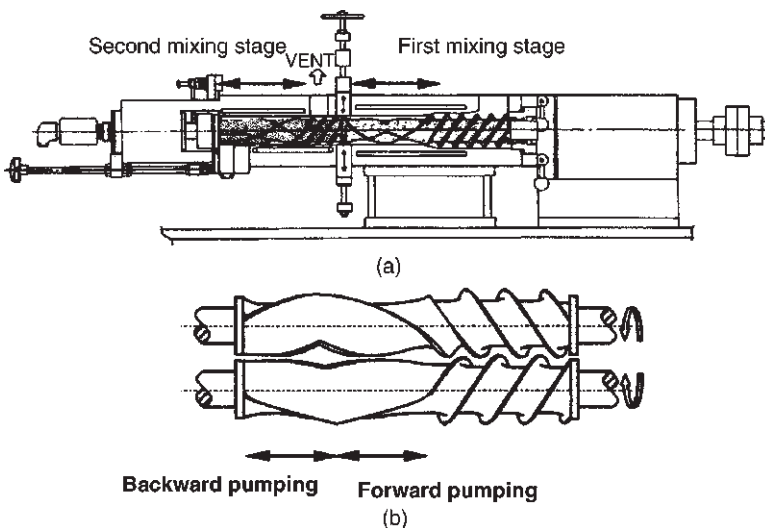

Fig. 10.49   The LCM 100G CM. (a) Schematic representation; (b) the second stage LCM rotors.
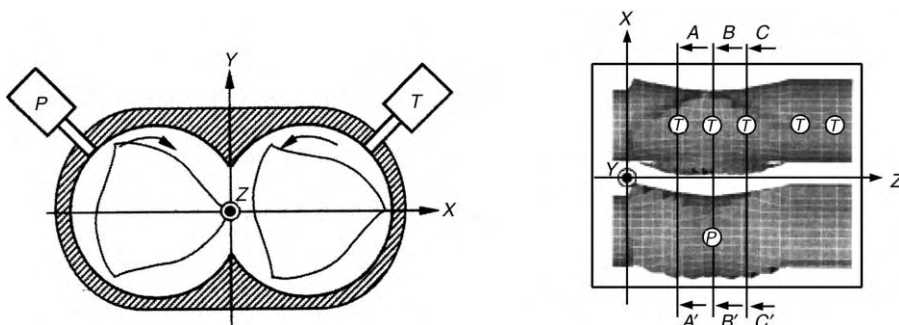
Fig. 10.50   Location of the pressure gauge (P) and the thermocouples (T) at the five axial barrel positions. The three cross sections A–A′, B–B′ and C–C′ are used for contour plots of the numerical results. [Reprinted by permission from T. Ishikawa, S. Kihara, K. Funatsu, T. Amaiwa, and K. Yano, "Numerical Simulation and Experimental Verification of Nonisothermal Flow in Counterrotating Nonintermeshing Continuous Mixers," *Polym. Eng. Sci.*, **40**, 365 (2000).]

The simulation is for a shear thinning fluid and nonisothermal flow. The equations of change are

$$\nabla \cdot \mathbf{v} = 0 \tag{10.2-57}$$

$$-\nabla P + \nabla \cdot \boldsymbol{\tau} = 0 \tag{10.2-58}$$

$$\rho C_p \mathbf{v} \cdot \nabla T = k\nabla^2 T + \boldsymbol{\tau} : \nabla \mathbf{v} \tag{10.2-59}$$

The constitutive equation is

$$\boldsymbol{\tau} = 2\eta \dot{\boldsymbol{\gamma}} \tag{10.2-60}$$

where

$$\eta = H(T)F(\dot{\gamma}H(T)), \qquad II\dot{\gamma} = \sqrt{2II_{\dot{\gamma}}} \tag{10.2-61}$$

$$F = \eta_0 \left[1 + \lambda_c^2 (2II_{\dot{\gamma}})\right]^{(n-1)/2} \tag{10.2-62}$$

$$H(T) = \exp[-\beta(T - T_a)] \tag{10.2-63}$$

The HDPE melt used has the rheological and thermomechanical parameters listed in Table 10.4. The boundary conditions employed are listed in Table 10.5. There was no

TABLE 10.4   Material Data of High Density Polyethylene

Carreau model parameter	λ	1.360
Carreau model parameter	n	0.296
Zero shear rate viscosity	$\eta_0[\text{Pa} \cdot \text{s}]$	52,930
Arrhenius' law parameter	$\beta[1/\text{K}]$	0.01
Reference temperature	T_a [K]	503.0
Density	$\rho[\text{kg/m}^3]$	752.0
Specific heat	C_p [J/(kg · K)]	1,900
Thermal conductivity	$\kappa[\text{W/(m} \cdot \text{K)}]$	0.225

TABLE 10.5 Boundary Conditions

Inlet cross section	Constant flow rate (375, 455, 500 kg/h)
Barrel inner surface	No slip
Rotor surface	Tangential velocity by screw rotation
Outlet cross section	Outflow

mixing-chamber barrel temperature control, the rotational speed was 420 rpm, and the three flow rates used were 375, 455, and 500 kg/h. The calculated average temperatures and their measured counterparts at the five axial thermocouple positions are shown in Fig. 10.51. As expected, decreasing the flow rate at constant rpm increases the temperature rise. The computed values, although in general agreement with the experimentally measured ones, are, however, less sensitive to flow rate. Figure 10.52 plots the temperature contours at cross section B–B′ for 500 kg/h. The difference between the maximum and minimum temperatures is 17°C. The temperatures are highest at the adiabatic rotor surfaces, and lowest at the cooling chamber barrel wall. Figure 10.53 plots the velocity vectors at plane (B–B′) and the axial velocity contours at cross-sections (B–B′) and (C–C′) at 500 kg/h.

High velocity vectors are obtained everywhere, and in particular at the window of interaction region. As expected, positive $dP/d\theta$ vales are calculated behind each of the wing tip gap regions. Small axial positive and negative velocities, due to small axial pressure drops, are calculated at (B–B′) the transition between the forward- and backward-pumping rotor sections. However, at (C–C′), while axial velocities are only about 5–15% of the circumferential, negative values are calculated in the large gap areas due to the backward-pumping mechanism of the helically twisted wings in this section.

The opposite occurs at the forward-pumping section (A–A′). However, axial velocities, although still beneficial for distributive mixing, are an order of magnitude of the

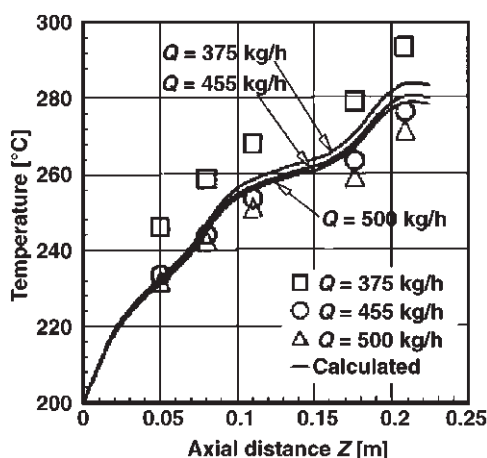**Fig. 10.51** Comparison between the calculated (average) and experimental temperatures at five axial positions. The entrance melt temperature was assumed to be 200°C. [Reprinted by permission from T. Ishikawa, S. Kihara, K. Funatsu, T. Amaiwa, and K. Yano, "Numerical Simulation and Experimental Verification of Nonisothermal Flow in Counterrotating Nonintermeshing Continuous Mixers," *Polym. Eng. Sci.*, **40**, 365 (2000).]
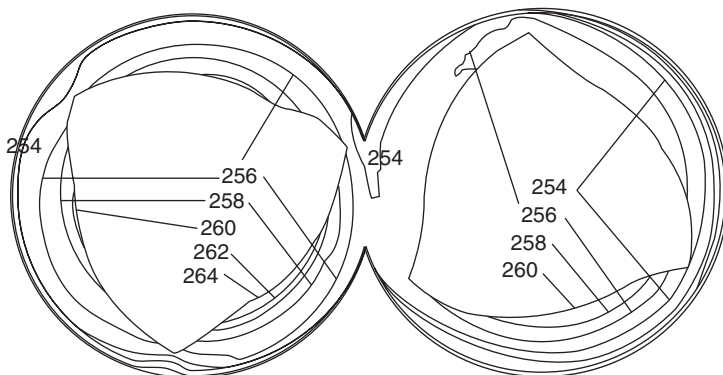
Fig. 10.52 Calculated temperature contours at cross section (B–B′) at 500 kg/h. [Reprinted by permission from T. Ishikawa, S. Kihara, K. Funatsu, T. Amaiwa, and K. Yano, ''Numerical Simulation and Experimental Verification of Nonisothermal Flow in Counterrotating Noninter-meshing Continuous Mixers,'' *Polym. Eng. Sci.*, **40**, 365 (2000).]

circumferential velocities, which are responsible for melting, heating, and dispersive mixing. Finally, Ishikawa et al. calculated the pressure as a function of the circumferential angle, and compared it with the experimentally obtained pressure transducer trace at (B–B′). The results are shown in Fig. 10.54.

Calculated results show a repetitive peak at 0° (120°), while the pressure transducer trace registers three peaks. Since the wing tip passes in front of the gauge every 120°, the
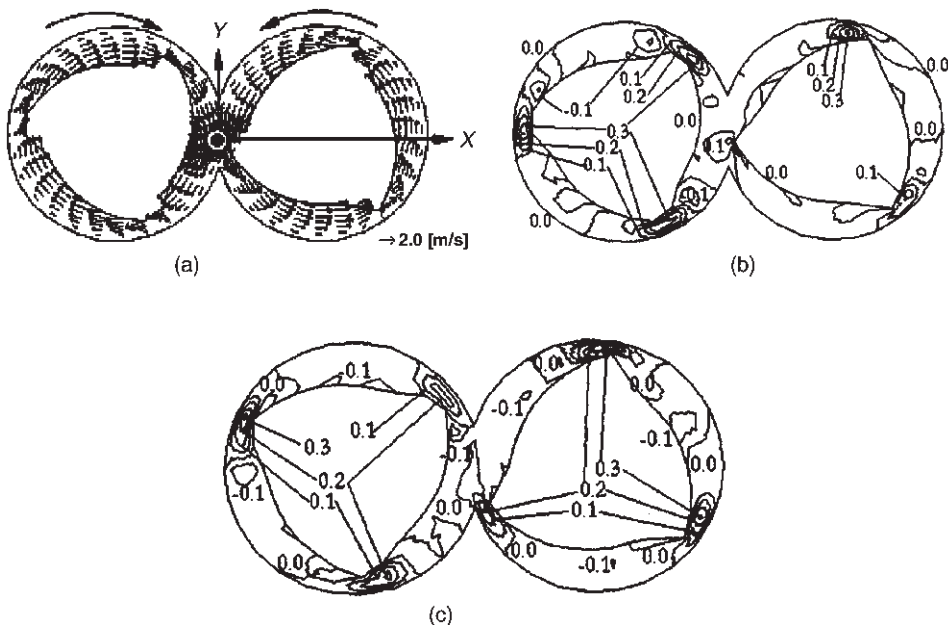
Fig. 10.53 Mixing-chamber melt velocities at cross sections (B–B′) and (C–C′). (a) Velocity vectors at (B–B′); (b) axial velocity contours at (C–C′); (c) axial velocity contours at (C–C′); all at 500 kg/h. [Reprinted by permission from T. Ishikawa, S. Kihara, K. Funatsu, T. Amaiwa, and K. Yano, ''Numerical Simulation and Experimental Verification of Nonisothermal Flow in Counter-rotating Nonintermeshing Continuous Mixers,'' *Polym. Eng. Sci.*, **40**, 365 (2000).]

Fig. 10.54   Comparison between calculated and experimental values of $P(\theta)$ at (B–B′) and 500 kg/h. [Reprinted by permission from T. Ishikawa, S. Kihara, K. Funatsu, T. Amaiwa, and K. Yano, "Numerical Simulation and Experimental Verification of Nonisothermal Flow in Counterrotating Nonintermeshing Continuous Mixers," *Polym. Eng. Sci.*, **40**, 365 (2000).]
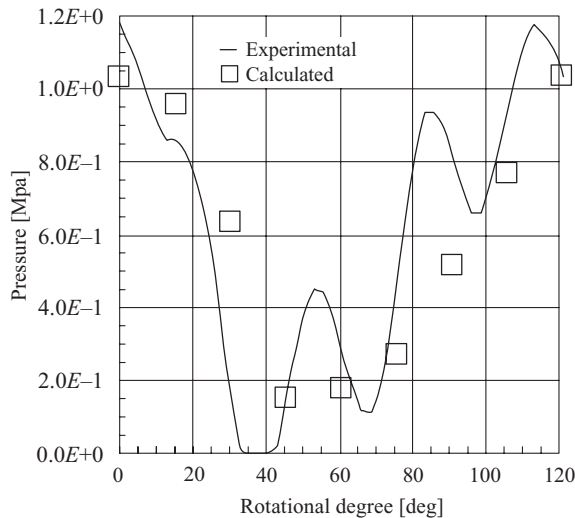
two extra local maxima are most probably due to small unfilled regions in the chamber. Other than that, there seems to be good agreement between calculated and measured pressure values. In summary, simulating an almost fully filled second-stage LCM mixer chamber with the robust three-dimensional FEM scheme of the Funatsu group, which assumes full chambers, proves to be useful to engineering practice. Yet for predicting total energy consumption and for answering scale-up questions, we need a better understanding of the melting step.

10.3   CO-ROTATING, FULLY INTERMESHING TWIN SCREW EXTRUDERS

We have introduced some of the main design features and attributes of the Co-TSEs in Section 10.1. We devote this section to the discussion of the elementary steps of processing as they occur in these devices. We note the following references, chapters in edited texts that provide detailed information on the design features and capabilities of equipment provided by the major Co-TSE manufacturers: Andersen of Coperion Werner and Pfleiderer (74,75), Sakai of Japan Steel Works (76,77), Todd of APV-Baker Perkins (12,78), and Mack of Berstorff (79). Anderson (75), in an overview of Co-TSE design and functions, points out that the two most important equipment parameters are (a) the outer-to-inner diameter ratio (OD/ID), shown for bilobal screws and kneading elements in Fig. 10.55, and (b) the specific torque, defined as the ratio of the torque, M, to the cube of the screw-to-screw centerline distance, C_L. The gap between adjacent screw elements is the minimum required for mechanical safety. Thus, it is assumed to be zero in evaluating C_L. Since the crest of one screw (kneading disk) traces the root and flank of the mating screw, one screw wipes its associated mate.
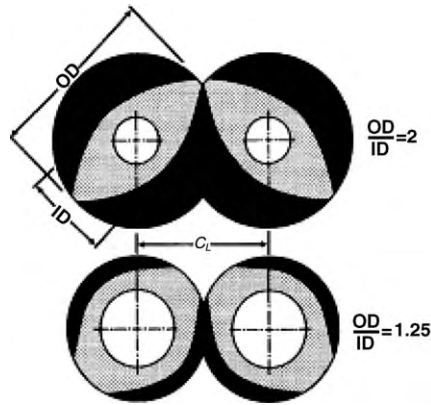
Fig. 10.55 Two extremes of OD/ID ratios for two-lobe machines.

The OD/ID ratio defines the free volume, which can be filled by the polymer, Thus, the larger the OD/ID, the larger the equipment capacity, but as can be seen in Fig. 10.55, the smaller the available shaft diameter for torque transmission, the lower the applied average shear rate. Thus, the design challenge for building a high rate Co-TSE, that is, one with high OD/ID, is to be able to supply it with high specific torque, which relates to the power provided to the free volume. If this is achieved, then the Co-TSE can operate at higher degrees of fill, high rates, and lower rpm, resulting in lower discharge temperatures. This trend has been developing over the last 30 years or so, as can be seen in Table 10.6, which lists the evolution of Coperion Werner and Pfleiderer Co-TSEs with both increased OD/ID and specific torque, $M(C_L)^3$.

The Megacompounder, developed in 1995 by Heidemeyer (80), achieved the highest specific torque and OD/ID ratio (for the entire spectrum of available machine sizes and barrel diameter, 32–380 mm) by utilizing 24 shaft splines to transmit the shaft energy to the screw/kneading elements, instead of the usual one-to-six keys. The 30% increase in specific torque from the Super- to the Megacompounder required gear box redesign for delivering greater power and this, together with specific screw configurations, allowed for rotational speeds of up to 1200 rpm. Finally, it is desirable to have the two important parameters of OD/ID and $M/(C_L)^3$ constant over the available size range of any given type

TABLE 10.6   Comparison of the Six Generations of ZSK Machines

	Z	OD/ID	$M/(C_L)^3$
1. ZSK–standard	3	1.22	3.7–3.9
2. ZSK–variable	3	1.22	4.7–5.5
1. ZSK–standard	3	1.22	3.7–3.9
3. ZSK–variable	2	1.44	4.7–5.5
4. ZSK–compact	2 or 3	1.22 or 1.44	7.2–8.0
5. ZSK supercompounder	2	1.55	8.7
6. ZSK megacompounder	2	1.55	11.3
7. ZSK mega plus	2	1.55	13.6

Note: OD = screw outer diameter; ID = screw inner diameter; α = centerline distance; M = torque/shaft; Z = number of flights (75).
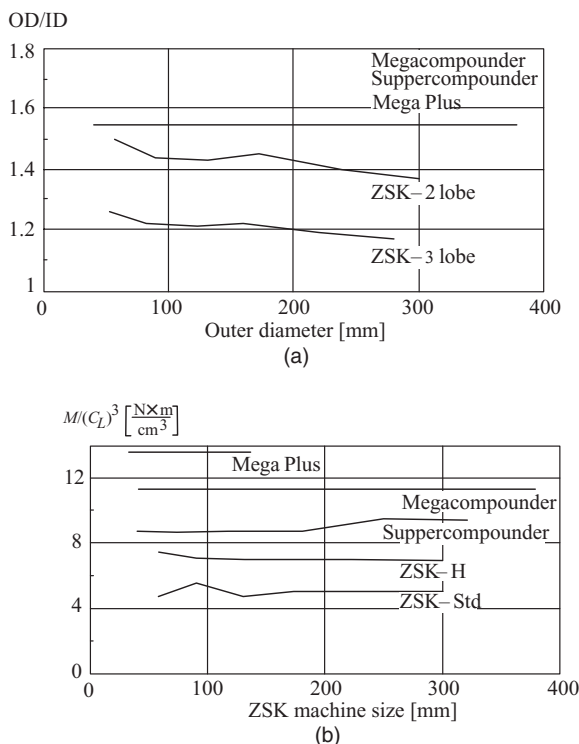
Fig. 10.56 Different ZSK generations over a range of barrel diameters. (a) Values of OD/ID; (b) values of the specific torque available. [Reprinted by permission from P. G. Andersen, "The Werner and Pfleiderer Twin Screw Co-rotating Extruder System," in *Plastics Compounding*, D. B. Todd, Ed., Hanser, Munich (1998); P. G. Andersen, private communication.]

of equipment, for example, supercompounders. The reason being that scale-up become easier because both the feed intake capabilities and power acquirement do not change.

The latest ZSK Mega Plus generation, developed with further gear box improvements, achieves a 13.6 specific torque value maintaining OD/ID at 1.55. Currently, the largest size Mega Plus ZSK is 133 mm. Figure 10.56 provides data on the values of these two parameters for several generations of Coperion ZSK Co-TSEs.

As mentioned in the introduction to this chapter, Co-TSEs are modular in barrel components, with individual rotating shaft elements and element sequences associated with each of the barrel segments in order to achieve a specific primary process goal, such as affecting melting. Typical types of barrel segments are shown in Fig. 10.57. Each barrel segment is 4 *L/D* long, and typical total machine lengths are in the range of 24–40 *L/D* for compounding; for large-size postreactor finishing operations, long *L/D* are necessary. Co-TSEs are used to carry out reactive processing to provide enough time to the dispersed and/or mixed reactant so that $t_{react}/t_{res} \sim 10^{-1}$ (see Section 11.2). One of 'Todd's rules'[8] is that "each elementary step in co-rotating, intermeshing TSEs takes 4 *L/D* (one barrel section) to be completed." Thus, for solids transport, melting, additives feeding, mixing,

---

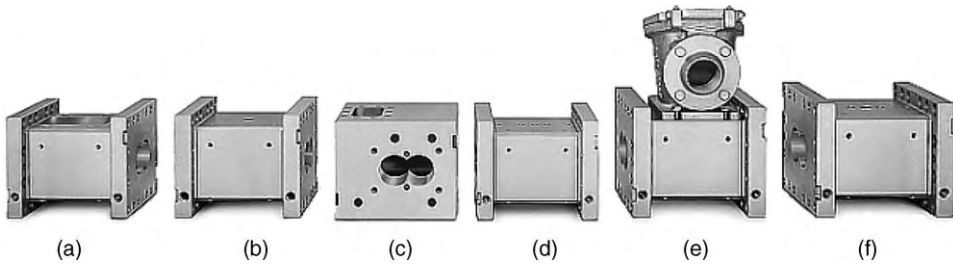8. D. B. Todd, private communication.

Fig. 10.57 Typical 4 *L/D* Co-TSE barrel segments. (a) Feed throat; (b) melting; (c) downstream feed section; (d) mixing; (e) devolatilization; (f) pumping and limited pressurization. [Courtesy of P. Andersen Coperion Werner and Pfleiderer, Ramsey, NJ.]

devolatilization, and pumping, we need a minimum of 24 *L/D* length. For large postreactor extruders, which primarily melt and pelletize powders, $L/D \sim 20$.

Feeding and Transport of Particulates and Additives in Co-rotating, Twin Screw Extruders

As is common with twin screw equipment, Co-TSEs are starve-fed by metering feeders, that is, their solids conveying capacity exceeds that of the downstream requirements, making feed rate independent of the *screw speed*. This makes screw speed an *independent variable*, and permits the control of residence time, degree of fill, and specific energy input (kw-h/kg). This, of course, at the expense of having to use feed metering equipment. Optimal equipment capability utilization is reached when all of the available power is fully utilized at the feed intake upper limit. Feeders must be capable of adjusting the operating feed-rate setting to within 1–2% over a 10-s period. This is because the typical residence time within a process section, where an elementary step takes place, is about 10 s. With feeders having such capabilities, there is no need for preblending. The feed-throat diameters are usually 1.5 D, allowing for the accommodation of very low bulk-density powders. Only with the very large-capacity finishing line extruders can feeding of powders at rates of 50–100 t/h be troublesome, because the stream of excluded air exiting the feed throat causes feed fluidization.

Todd (3) notes that (1) in *single-stage* compounding processes and extruders, all dry feed components are metered in a single feed throat; liquid additives may be injected through downstream ports. Non-abrasive additives at low concentrations (e.g., pigments) can be co-fed with the polymers. (2) In *multi-stage* compounding processes and extruders, feed ingredients, such as the preceding, are fed and melted in the first melting section (zone). Downstream this zone, a section of feed screws, running starved, passes by the second feed part, where ingredients such as the following are introduced, typically through a side-entering feeder: long fibers to be mixed with the melted polymer(s), thus minimizing (not avoiding) fiber length attrition and machine wear; polymers with much lower viscosities than those fed in the feed stage. If large concentrations of such low-viscosity polymers are required by the blend application, more than one port can be used for sequential addition of such low viscosity polymer to avoid "scalloping," leading to incomplete mixing or phase inversion (see Section 11.3); and liquid, low-viscosity additives that would cause first single-stage powder feed to agglomerate. Again, more than one port may be required for higher concentrations; abrasive solid additives, whereby the

molten first-stage polymer(s) provide lubrication protection to the machine; additional low density particulate feeds to achieve higher throughput if feed throat feeding capacity is exceeded; and finally, reactive liquid ingredients in low concentrations, which are introduced through a barrel tap fitted, small-diameter tube by a liquid-metering pump. The exit tip may extend into the melt if it is introduced in a rotating disk region (81) so that the reacting ingredient enters the bulk of the flowing melt to be distributively mixed. High pitch screw conveying elements (e.g., 2.0 D) are typically used in the feed zone. For low bulk-density feed, TSE manufacturers have transformed self-wiping feed screw element profiles into square-channel profiles, allowing for up to 40% increase in free volume and powder conveying capacity (75).

Melting in Co-rotating Twin Screw Extruders

Melting in Co-TSEs takes place primarily and most commonly in kneading elements that are full of compacted particulates because of a flow restriction, such as reverse kneading or screw elements; the restriction creates a certain filled length and generates the needed pressurization for the melt (or partially molten polymer) to flow through the restriction. The evolution of melting in such filled kneading-element channels was studied experimentally by Kim (82) and Gogos et al. (17) utilizing carcass analysis, and is shown schematically in Fig. 5.14. Their conclusions as to the genesis and evolution of melting appear as comments in that figure. They found that interparticle FED, defined by Eq. 5.9-1 with evidence of it shown in Fig. 5.15, takes place early and does not require full compaction. At full compaction, PED, defined by Eqs. 5.9-2 and 5.9-3, becomes a *dominant* melting mechanism. It is caused by the "mandatory" and repetitive compressive/squeezing deformations brought about by the kneading elements (see Fig. 5.16).

Kim (82) estimated PED from compressive experiments on molded disks of a number of materials, as shown in Fig. 5.17. High modulus, yielding, amorphous polymers such as PS dissipate a large amount of mechanical energy, compared to lower modulus, polycrystalline polymers, as shown again in Fig. 5.17. Iso-PED and corresponding iso-ΔT_{adiab} contours can be obtained from a number of cylindrical specimens compressed to various strains at various initial temperatures, as shown in Fig. 5.18(a) and 5.18(b). From such plots, the expected ΔT_{adiab} from one or more successive ε_i deformations can be obtained, as shown in Fig. 5.19, for PS compressed to successive $\varepsilon_0 = 1$ deformations.

The experimental work of Kim (82) and later on of Gogos, Qian, Todd, and Kim (83–86) demonstrated the dominant role of PED, *not only in initiating but also appreciably advancing* melting almost to completion for high modulus, yielding under compression polymers, such as PS. Thus, they created a simplified but physically reasonable model for predicting the course of melting, by assuming that the compacted particulate assembly can be reasonably represented as a "solids continuum" undergoing *repeated* and *spatially uniform* deformations and deformation rates determined by geometric and process variables, and getting heated/melted in the fashion shown in Fig. 5.19. With this approach, they were able to make good engineering estimates of the actual melting length in full Co-TSE kneading elements. This simple model is as follows:

1. First, the average "transit time," $t_{transit}$, needed by the charge to go over one lobe is calculated

$$t_{transit} = \frac{V_{avail}}{\dot{m}/\rho_b} \tag{10.3-1}$$

where

$$V_{\text{avail}} = 3.08 HDL_{\text{lobe}} \qquad (10.3\text{-}2)$$

and where $D = $ OD of the bilobal element, $\dot{m}$ is the mass flow rate, and H is the maximum channel depth, that is, the difference between OD and ID of the kneading element. Thus,

$$t_{\text{transit}} = 3.08 H \cdot D \cdot L_{\text{lobe}} \rho_b / \dot{m} \qquad (10.3\text{-}3)$$

2. Second, the number of rotations that takes place during the transit time of the charge over one lobe, N_R, is given as

3.
$$N_R = t_{\text{transit}} RPS \qquad (10.3\text{-}4)$$

where RPS is the operating rotational speed (rev/s).

4. With the preceding, the number of compressions experienced by the charge during its entire transit over one lobe, N_C, is

$$\begin{aligned}
N_C &= \frac{4}{3} N_R \\
&= \frac{4}{3} \cdot t_{\text{transit}} \cdot RPS \\
&= \frac{4}{3} \times 3.08 HDL_{\text{lobe}} \rho_b RPS / \dot{m} \\
&= 4.1 HDL_{\text{lobe}} \rho_b RPS / \dot{m}
\end{aligned} \qquad (10.3\text{-}5)$$

Thus, the number of PED-producing, kneading element pair compressions that the particulate charge is subjected to during its transit time over one lobe decreases with increasing mass flow rate and increases with increasing rotational speeds, increasing bulk density (degree of compaction), increasing diameter and maximum channel depth (related to (OD/ID)) and finally, it increases with increasing lobe length. There is another effect caused by increasing the lobe length L_{lobe}, which is shown schematically in Fig. 10.58. As the axial length (width) of the lobe is increased, the edge effects of reduced pressure generated become less important and the wide lobe becomes a more effective compressive "device."

The effectiveness of PED to melt PS is shown in Fig. 10.59 as the melting evolution of the carcass of PS being melted by *two forward* wide-lobe kneading sequences $2 \times [45/5/42]$, followed by *one reverse* narrow-lobe sequence 45/5/14 (R) at 180°C, 180 rpm and 6.9 kg/h. The Co-TSE used was the Twin Screw Mixing Element Evaluator (TSMEE®) developed by the Polymer Mixing Study of PPI, which has the Coperion Werner and Pfleiderer ZSK 30 design parameters: 30.65-mm barrel diameter, 21.0-mm screw-root diameter, 26.2-mm centerline distance, and length of one lobe of 8.4 mm. Under these processing conditions, PS undergoes three compressions during its transit time over one lobe. Experimentally, practically complete melting is observed in one lobe, Fig. 10.59(a).

Figure 10.59(b) indicates that as few as three $\varepsilon = 1$, spatially uniform compressions of PS are capable of heating it past its T_g. Thus, there is good agreement between the

Broad   **Narrow**

Lobal pool capture   **Melt division**
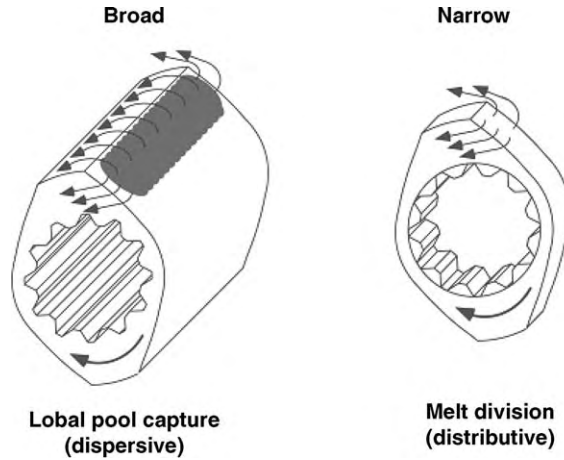**(dispersive)**   **(distributive)**

Fig. 10.58   The effect of increasing kneading-lobe length on its compressive and squeezing capabilities. [Courtesy of C. Martin, American Leistritz Corp.]

experimental and simple PED model results. Kim and Gogos (85) conducted a number of carcass analysis, PP melting experiments at varying barrel temperature, mass flow rate, rotational speed, and width of the lobe. The results are shown in Table 10.7. The agreement between experimental carcass analysis results and those calculated by the PED model is good. The observed melting lengths are either the same or shorter than the predicted ones.
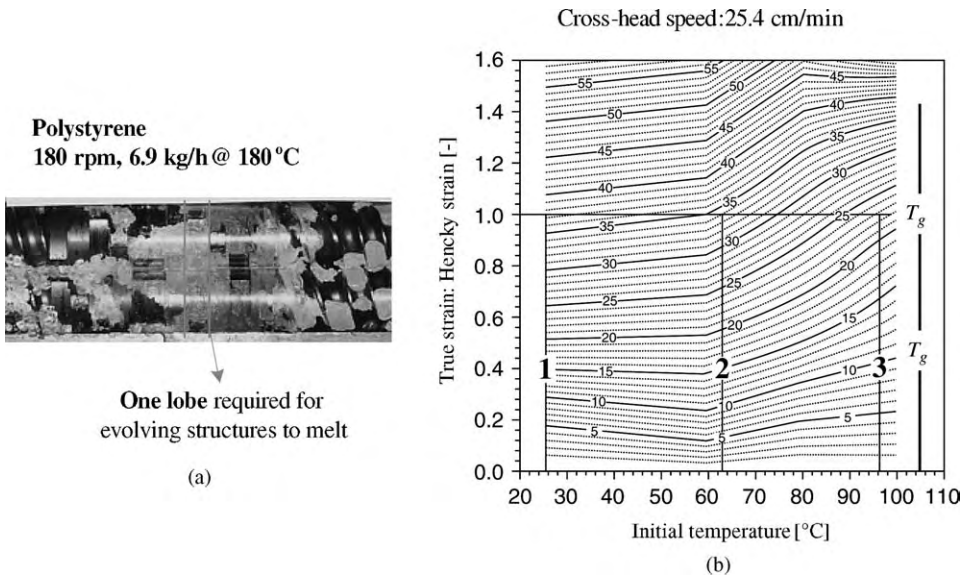
Fig. 10.59 (a) Picture of the carcass of the compressed PS pellet bed in the melting region of the TSMEE, indicating that PS reaches T_g in one lobe axial distance. (b) Iso-adiabatic temperature increases during compressive deformation experiments on cylindrical PS samples at various initial temperatures, indicating that three $\varepsilon = 1$ compressions can bring PS to its glass transition temperature. [Reprinetd by permission from M. H. Kim, Ph.D Dissertation, Department of Chemical Engineering, Stevens Institute of Technology, Hoboken, NJ, 1999.]

TABLE 10.7   Comparison of the Experimentally Obtained Melting Lengths with those Calculated by the Simple PED Model of Kim and Gogos (86)

Experimental Conditions $T_b/\dot{m}$/rpm/screw type	Melt Temperature °C	Solid-Plug Velocity	Holding Time per Lobe	Predicted Number of Lobes	Observed Number of Lobes
150/5/60/s1	163	0.14	5.93	3	3
140/10/60/s1	166	0.28	2.96	6	4
180/10/60/s1	185	0.28	2.96	6	4
140/10/120/s1	187	0.28	2.96	3	2
180/10/120/s1	195	0.28	2.96	3	3
140/40/240/s1	187	1.13	0.74	6	4
180/40/240/s1	190	1.13	0.74	6	5
140/5/60/s2	174	0.14	2.82	6	4
180/5/60/s2	185	0.14	2.82	6	5
140/40/240/s2	197	1.13	0.35	13	10
180/40/240/s2	199	1.13	0.35	13	12

Note: Basel PP 6523 (MFI = 4), $L_1 = 8.4$ mm, $L_2 = 40$ mm kneading lobe lengths.

The reason for this discrepancy is that the PED model does not include the melting mechanism of VED, which, as shown in Fig. 5.14, takes place primarily in the melt-rich suspension stage of melting. Kim et al. found that their PED model works very well with polystyrene (PS) which, because of its tough ductile behavior under compression, generates very high PED values; Fig. 5.17 indicates a bulk temperature increase of around 30°C for a single $\varepsilon = 1$ compression. Furthermore, as seen in Fig. 5.1, the specific enthalpy needed to heat PS to $T = T_g$ is about 100 kJ/kg. Under these conditions, with only a few compressive deformations needed to plasticate (bring to a temperature above T_g) PS, VED cannot establish itself as a contributing melting mechanism; it does, however, above the glass transition temperature.

The physical reality is very different for PP: its melting temperature range is around 165°C, and the specific enthalpy needed to melt it is about 500 kJ/kg, five times that needed for PS to reach T_g (Fig. 5.1). Furthermore, as indicated in Fig. 5.17, the adiabatic temperature increase for a single $\varepsilon = 1$ compression of a room temperature cylindrical sample is only 8–10°C. Thus, a larger number of compressions is needed, at least an order of magnitude higher, to melt PP. Under these conditions, soon after some initial PED heating and local melt generation, VED contributes to melting in a significant way, becoming dominant at the melt-rich stage. Recently Wetzel et al. (87,88), working with a well-instrument 34-mm Co-TSE, filled with a glass window, attempted to separate the contributions of FED, PED, and VED during the evolution of melting, by introducing pulsed increases in the feed rate. Their results are preliminary, but represent a promising experimental technique to understand the relative roles of these dissipative melting mechanisms, which will aid in the development of a comprehensive model for melting in full kneading elements.

Qian et al. (18) have recently studied the evolution of melting of polymer blends composed of an amorphous high modulus (PS) component and a semicrystalline low modulus (LLDPE) component in Co-TSE full kneading elements. They observed that over a concentration range of 10–50%, the weaker modulus LLDPE melts faster than the higher modulus PS. Furthermore, when the semicrystalline component has a low melt
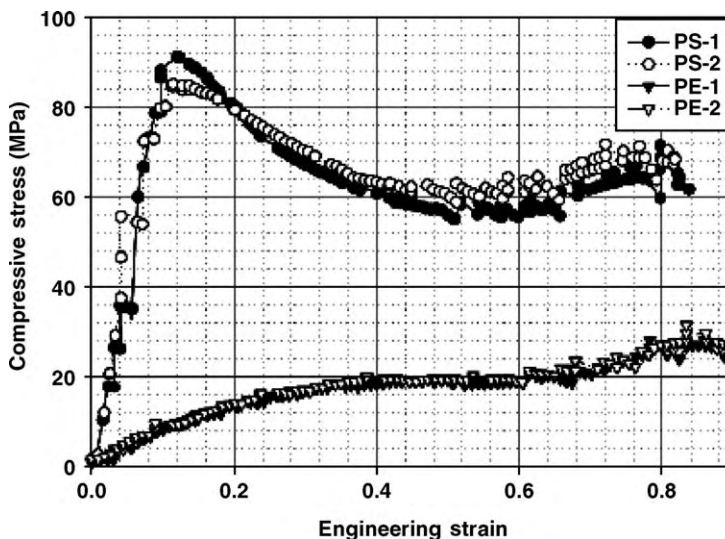
Fig. 10.60   Compressive stress–strain behavior of PS and LLDPE at 25°C and crosshead speed of 25.4 mm/min. At a compressive stress level of 20 MPa the deformation of the soft LLDPE is large, in the dissipative region and nearly twenty times the PS deformation, which is of the order of 0.04, in the elastic nondissipative range. [Reprinted by permission from B. Qian, D. B. Todd, and C. G. Gogos, "Plastic Energy Dissipation (PED) and its Role in Heating/Melting of Single Component Polymers and Multi-component Polymer Blends," *Adv. Polym. Techn.*, **22**, 85–95 (2003).]

viscosity, the amorphous component has very good chances of transiting the kneading-element melting zone without being completely melted. Of course, as noted earlier, when melting each of the individual components alone, PS melts faster, over a smaller full kneading element length than semicrystalline polymers, due to the very strong PED contribution to melting, as shown on Fig. 10.60, which depicts the individual stress–strain curves of PS and LLDPE. Examining this figure, we note that, if the two materials were stacked as two identical disks, one on top of the other, and a compressive deformation were applied on the stacked pair, then by the time a compressive stress level of 20 MPa was reached, under the conditions indicated, the deformation of LLDPE would be about twenty times larger than that of PS. Furthermore, at this stress level, the small PS deformation is in the "elastic" nondissipative range, while that of the LLDPE is past the yield point, dissipative, and giving rise to PED heating. Under such stacked-disk conditions, the LLDPE component will heat up and melt first, before the PS. In kneading elements full of a mixture of PS and LLDPE pellets we do not have a simple two-disk stack of the two components. Nevertheless, the forced cross-sectional area reduction resulting from the kneading element corotation will compress the randomly packed blend and, as stresses increase, the weaker LLDPE will deform much more than PS, resulting to the observed earlier melting of LLDPE.

   Potente and Melish (89), Bawiskar and White (90,91), Zhu, Narh, and Geng (92) and Vergnes et al. (93) have developed one-dimensional melting simulation models that are based on viscous energy dissipation and conduction being responsible for the rapid melting in Co-TSE's. The polymer charge being melted is a suspension of pellets, whose concentration diminishes with the evolution of melting. We deal briefly here with the work
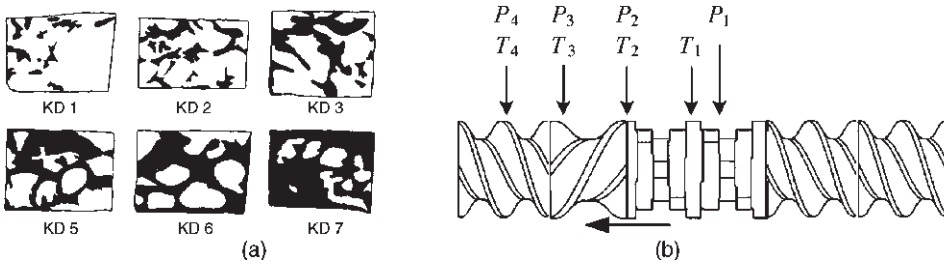
Fig. 10.61 (a) Evolution of the packed solids/melt mixtures obtained by carcass analysis during melting of PP in the 90° stagger kneading block shown in (b). The Co-TSE used was Clextral 45 mm running at 300 rpm and 100 kg/h. Polypropylene Solvay Eltex HL 001 750 μm beads. [Reprinted by permission from B. Vergnes, G. Souveton, M. L. Deacour, and A. Ainser, "Experimental and Theoretical Study of Polymer Melting in a Co-TSE," *Int. Polym. Process.*, **16**, 351 (2001).]

of Vergnes et al., which makes good use of experimental carcass analysis results. First, they discuss and accept, but disregard the "genesis" of the initial heating of pellets and the initial melt formation brought about by PED. Then they treat the initial, highly concentrated and inhomogeneous solids/melt mixture, Fig. 10.61(a), as a concentrated suspension, that is, an idealized "continuum" fluid suspension, shown in Fig. 10.62. The melting model of Vergnes et al. assumes that this idealized uniform suspension is characterized simply by a solid, concentration-dependent viscosity, which has the general form valid for monodispersed size spheres (94–97)

$$\frac{\eta_{\text{susp}}}{\eta_{\text{pol}}} = (1 + \alpha\phi)^{\beta} \tag{10.3-6}$$

where $\alpha = 1/\phi_m$ and ϕ_m is the maximum packing, and β is a particle-to-particle interaction parameter.

The flow on the suspension visualized and simplified in the model just discussed generates VED and heats the pellets, but *does not* deform them. Thus, they do not include the dissipative mix-melting (DMM) melting mechanism, only VED. However, with the proper parameter adjustments, they are able to make fair predictions of the overall melting
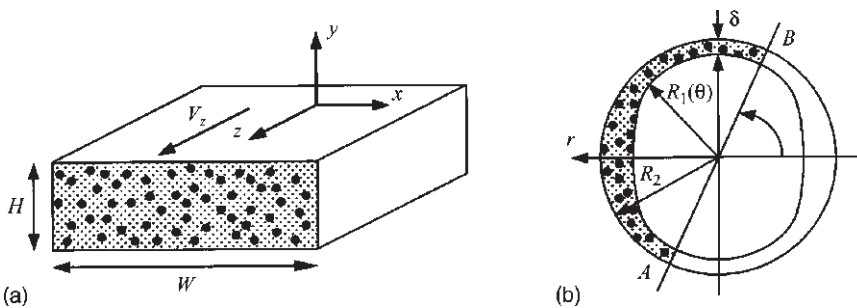

Fig. 10.62 Schematic description of (a) the solid/liquid mixture in the screw channel, and (b) around a kneading disk (93).

lengths. Their model first computes the number of uniform-sized solid particulate spheres of radius R_0, corresponding to the initial volume fraction of particulates, ϕ_0:

$$M = \frac{3\phi_0 \Delta V}{4\pi R_0^3} \qquad (10.3\text{-}7)$$

where $\Delta V = A_f \cdot \Delta z$ and A_f is the available cross-sectional area between a pair of kneading elements. The radius of the spheres decreases as they are heated by the flowing suspension exhibiting VED, via convective heat transfer. The sphere radii become zero at complete melting. What is needed to complete the model is, first, an evaluation of the relative viscosity as a function of f; second, the flow field and expressions for the average shear rate, $\dot{\gamma}$, and $VED = \eta_{rel}(\phi)\bar{\dot{\gamma}}^2 = W(z)$; third, the average melt temperature increase over Δz; and fourth, the reduction of the pellet radii because of convection heat transfer.

It is worth noting that the method used by Vergnes et al. in experimentally obtaining the relative viscosity equation parameters, α and β in Eq. 10.3-6. They worked with two almost identical PP homopolymers, one in 4-mm mean pellet diameter form, and the other in the form of small, 750-μm-diameter beads (Solvay Eltex HL 101). A 21-mm Co-TSE was fitted with a rheometric slit of length $L = 52$ mm, width $w = 28$ mm, and an adjustable gap spacing $1.5 \leq h \leq 2.5$ mm. The polypropylene in pellet form was fed at the feed throat and melted. Just before the die, a second feed port introduced the PP in bead form at various rates, resulting in different effective ϕ values. Two pressure transducers at the die were used to record the slit pressure drop $\Delta P(\phi)$. The relative viscosity was then expressed as

$$\eta_{rel} = \frac{\eta(\phi)}{\eta 0} \qquad (10.3\text{-}8)$$

The main assumption made in the preceding relative viscosity evaluation is that no PP bead size reduction and no shape change took place in the slit. This is reasonable only if the heating characteristic time R_o^2/α_{th} is small compared to the average residence time in the slit. Here, α_{th} is the thermal diffusivity, which is in the range of 10^{-3} cm^2/s. The heating time for the 750-μm-diameter beads is then around 1.5 s. Thus, for their assumption of rigid spheres going through the slit rheometer to hold, the average slit velocities must be greater than 5 mm/s. Their experimental results yielded values for the suspension rheological parameters $\alpha = -1.11$ and $\beta = -0.51$. The velocity field in the kneading elements is approximated by that around one isolated kneading disk in the manner developed by Werner (98). The results obtained with such a model are shown in Fig. 10.63, and for the screw and kneading element sequence in Fig. 10.61(b). It is evident that neither the PED model of Kim and Gogos nor the VED model of Vergnes et al. not other investigators are physically *fully* exhaustive in that they are incapable of describing the evolution of melting in full kneading elements in terms of all the melting mechanisms taking place alone and in parallel until all particulates melt.

Jung and White (99) expressed PED in the following interesting way: They considered a bed of compacted pellets with material points inside the pellets. They then applied the energy equation applicable for this system (100)

$$\rho c_p \left[\frac{\partial T}{\partial t} + (\mathbf{v} \cdot \boldsymbol{\nabla})T \right] = -\boldsymbol{\nabla} \cdot \mathbf{q} + \sum_i \sum_j \sigma_{ij} \frac{\partial v_i}{\partial x_j} \qquad (10.3\text{-}9)$$
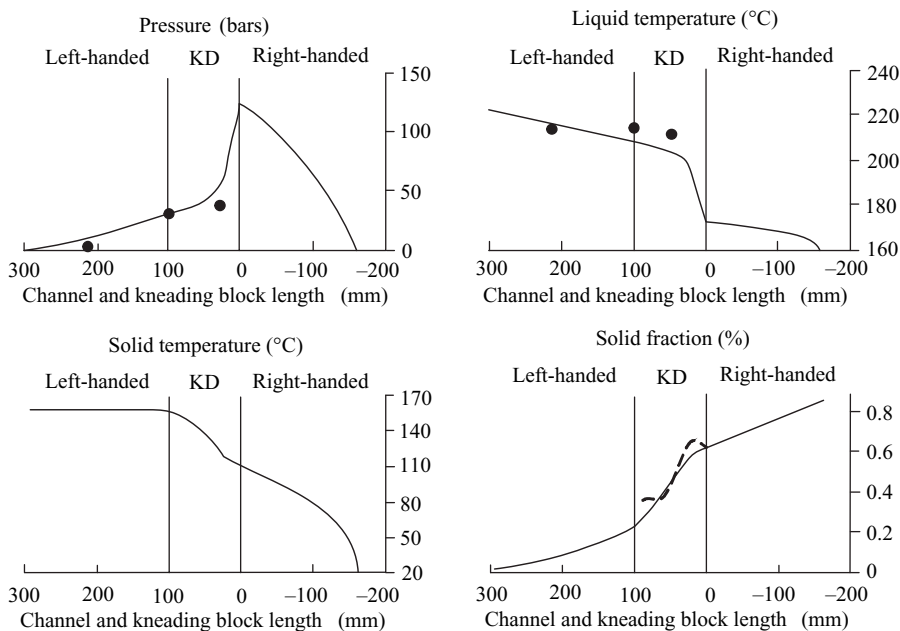
Fig. 10.63 Computation of melting process (screw sequence in Fig. 10.61(b), $N = 300\,\text{min}^{-1}, Q = 100\text{kg/h}$); dotted line and black symbols are experimental values. [Reprinted by permission from B. Vergnes, G. Souveton, M. L. Deacour, and A. Ainser, "Experimental and Theoretical study of Polymer Melting in a Co-TSE," *Int. Polym. Process.*, **16**, 351 (2001).]

and integrated it over the pellet, so that it applies to a moving pellet with diameter D, resulting in

$$\rho c_p V_p \frac{d\bar{T}_p}{dt} = hA_p\left(\bar{T}_p - T_s\right) + \sum_{ij} \bar{\sigma}_{ij} \frac{dv_i}{dx_j} V_p \qquad (10.3\text{-}10)$$

where V_p and A_p are the volume and surface area of the pellet, $\bar{T}_p$ is the mean pellet temperature, h is the heat transfer coefficient, and T_s is the surface temperature. The last term on the right side is PED, or what they call "bulk interior melting." They then neglected the convective heat transfer term and assumed that the deformation the pellet undergoes is *uniaxial extension*, although in the processing machines pellets undergo compressive deformation, a difference that is very important if one considers PS, which is brittle in tension and tough ductile in compression. Under these assumptions

$$\frac{d\bar{T}_p}{dt} = \frac{1}{\rho c_p}\left(\frac{F}{A_p'}\right)\frac{1}{L_p}\left(\frac{dL_p}{dt}\right) \qquad (10.3\text{-}11)$$

$$\bar{T}_p(t) - \bar{T}_p(0) = \int_0^t \frac{1}{\rho c_p}\left(\frac{F}{A_p'}\right)\frac{1}{L_p}\left(\frac{dL_p}{dt'}\right) dt' \qquad (10.3\text{-}12)$$

where (F/A_p') is taken to be the *tensile yield stress*, shown for LLDPE in Fig. 10.64, and A_p' and L_p are the deformed cross-sectional area and length of the pellet.
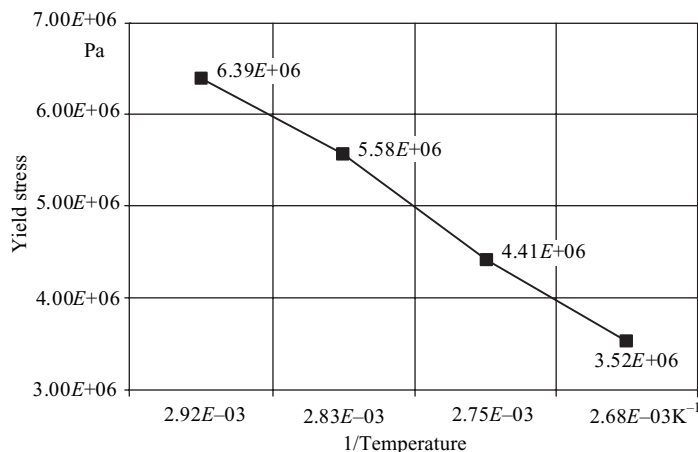
Fig. 10.64   The temperature dependent tensile yield stress for LLDPE (Dow, Dowlex 2045) obtained at Instron crosshead speed of 20 in/min. [Reprinted by permission from H. Jung and J. L White, "Investigation of Melting Phenomena in Modular Co-TSEs," *Int. Polym. Process.*, **18**, 127 (2003).]

The temperature increase of a pellet by this rather simplified treatment can be calculated knowing ρ, c_p, estimating dL_p/dt, and thus A'_p, and evaluating experimentally $(F/A'_p)(\bar{T}_p)$. This treatment is similar to that of Kim and Gogos in its ability to estimate pellet heating by PED in a simple fashion, needing only the experimental evaluation of the large deformation mechanical behavior of polymer solids.

Flow and Pressurization in Co-rotating Twin Screw Extruders

We now turn to flow and pressurization affected by Co-TSE full-screw and kneading-conveying elements. In Section 6.8 we noted the simple flow rate expressions for isothermal flow of Newtonian fluids in full Co-TSE conveying screw channels, similar in form to those in single screw, full-melt pumps, but containing in both the pressure and drag flow terms, shape factors to account for the channel contour and for the presence of the transition space between the screws where drag flow vanishes, because of the opposing sense of rotation of the screws there (see Eqs. 6.8-12 to 6.8-14). Todd (101) presents calculated values for the drag flow A_t and pressure flow B_t parameters in the flow rate expression

$$Q = A_t N - B_t \Delta P/\eta L \tag{10.3-13}$$

which are listed in Table 10.8 for both kneading and screw elements. They provide *qualitative engineering estimates*.

Considerable work in the three-dimensional simulation of flow in the full conveying screw and kneading elements has been carried out since 1990, when Gotsis et al. (102) treated a Newtonian fluid, isothermal flow, and the problem of time dependence of the geometry of the channels by constructing a three-dimensional mesh covering the entire space inside the barrel, which could be occupied either by the melt or the kneading disks or screws, checking at each step for the space occupied by melt. Lawal and Kalyon (103) extended this work to calculate the intensity of segregation using particle tracers. Wang et al. (104) used FEM for Power Law fluids flowing isothermally, in a number of Coperion

TABLE 10.8   Drag and Pressure Flow Constants for a 50.8-mm Twin Screw Extruder (78)

Bilobal Kneading-paddles Configurations			
Offset Angle	Paddle Width	A_t (cm^3)	B_t (cm^4)
30	12.7	51.5	0.53
45	6.3	18.7	0.19
45	12.7	31.1	0.34
45	25.4	36.4	0.60
60	6.3	5.7	0.23
60	12.7	17.9	0.36
60	25.4	22.9	0.49
90	12.7	0.0	0.43

Screw Configurations		
HELIX ANGLE	A_t	B_t
6.1	12.4	0.021
18	41	0.118

elements. Kiani et al. (105,106) used a spectral-element method for a three-dimensional, quasi–steady-state solution of the continuity and motion equations, using periodic boundary conditions. Yang (107) and Cheng and Manas-Zlowczower (108) addressed the transient nature of the flow by reasonably assuming creeping flow, thus approximating the transient flow as a sequence of steady flows at intermediate times. Experimental results of the dynamic pressure profiles by McCullough and Hilton (109) and Christiano and Lindenfelzer (110) reinforced the importance of the intermeshing region and the three-dimensional velocity field there, including strong intermeshing, regional axial squeeze flows. They provided the impetus for intensified investigations by a number of researchers. The first to address the need to compare three dimensional FEM full kneading-element computational results with experimentally obtained dynamic pressure profiles was the group of Hrymak, Bravo et al. (111) and Jaffer et al. (112). The numerical results hold for a quasi–steady-state solution of isothermal full kneading-channels flow of a Carreau model melt.

McCullough and Hilton equipped the ZSK 30 barrel with five evenly spaced ports every 30 mm along the top and bottom of the center apex region, and three ports along the sides, spaced every 60 mm. The twin screw assembly was mounted on a movable lathe bed, allowing the barrel and ports to be moved wherever needed along the screw elements to obtain the dynamic pressure data. The transducer locations and kneading element block used are shown in Fig. 10.65. The transducers were capable of responding quickly at 800 MPa/s. Experimentally, it was found that pressure fluctuated as much as 160 MPa/s.

The numerical determination of pressures at the apex and side was as follows: Nine calculated pressure points (see Fig. 10.66), were interpolated in a cross pattern to cover a 1-mm-diameter circle, which corresponds to the exposed area to the transducer.

Figure 10.67(a) and 10.67(b) depict the experimental and simulation pressure profiles at the apex region and the side port of kneading element 5 of the 45/5/20 kneading block, respectively [see Fig. 10.65(b)]. In both cases, of course, it is the motion of the rotors that generate the pressure profiles. The side port fluctuations are of the same nature as those of the flight tip in the CMs and calenders, essentially converging/diverging geometry
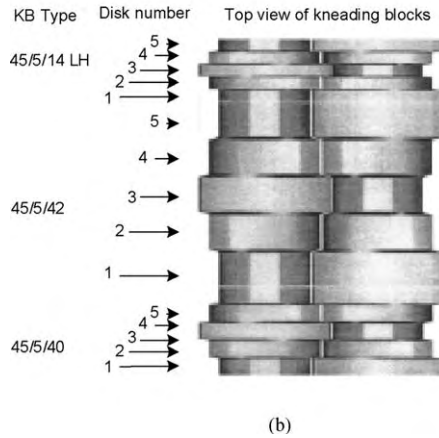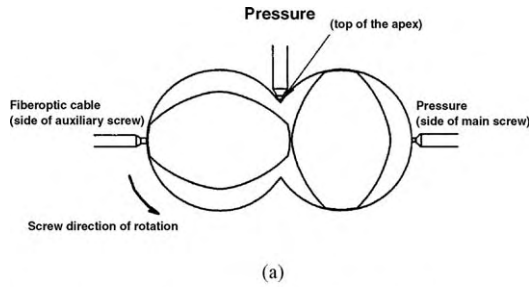
(a)

(b)

Fig. 10.65 Experimental apparatus used by McCullough and Hilton (109). (a) Transducer circumferential locations, (b) kneading block used for the ZSK 30 barrel. [Reprinted by permission from V. L. Bravo, A. N. Hrymak, and J. D. Wright, "Numerical Simulation of Pressure and Velocity Profiles in Kneading Elements of a Co-TSE," *Polym. Eng. Sci.*, **40**, 525–541 (2000).]
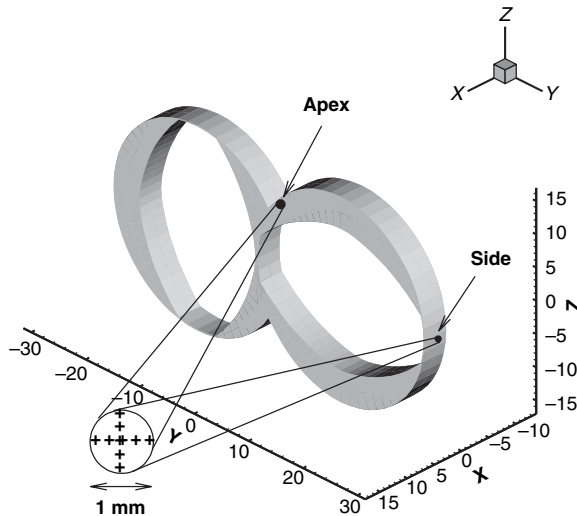

Fig. 10.66 Schematic representation of the mode of numerical determination of pressure at the apex and side pressure port. [Reprinted by permission from V. L. Bravo, A. N. Hrymak, and J. D. Wright, "Numerical Simulation of Pressure and Velocity Profiles in Kneading Elements of a Co-TSE," *Polym. Eng. Sci.*, **40**, 525–541 (2000).]
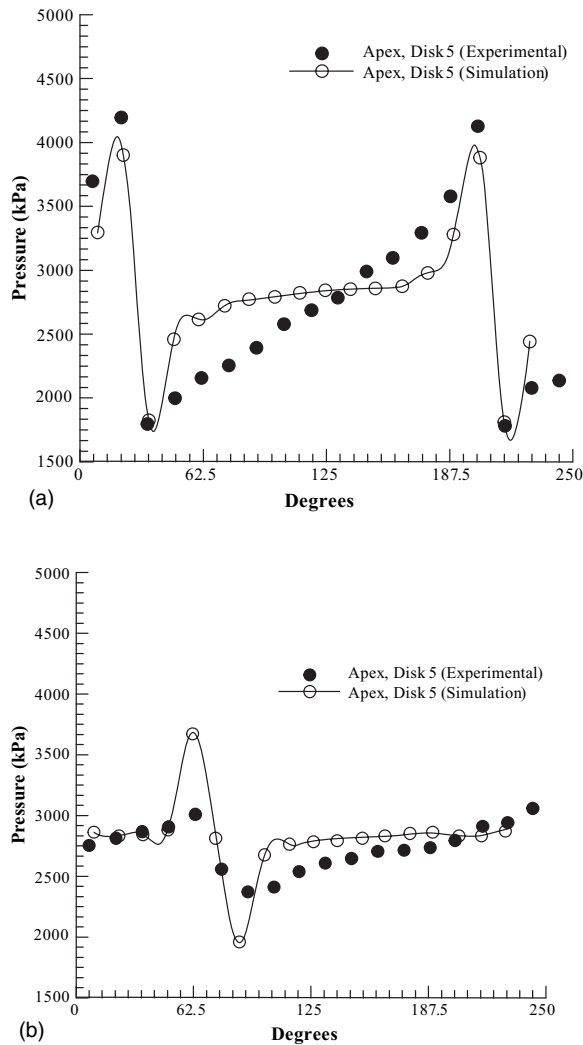
Fig. 10.67   Experimental and simulated pressure profiles obtained with kneading disk 5 of the 45/5/20 element sequence shown in Fig. 10.65(b). (a) Apex region and transducer; (b) wide channel region and side port. [Reprinted by permission from V. L. Bravo, A. N. Hrymak, and J. D. Wright, "Numerical Simulation of Pressure and Velocity Profiles in Kneading Elements of a Co-TSE," *Polym. Eng. Sci.*, **40**, 525-541 (2000).]

resulting in drag flow pressurization. The experimental extremes are 3 and 2.3 MPa, while the calculated are 3.7 and 1.8 MPa, clearly overestimated. In the wider gap region, the agreement is quite good. Turning to the much higher pressure, fluctuations at the apex region originate from the encounter of the two kneading elements, as shown in Fig. 10.68. A small chamber is created and then reduced in size until it disappears, another small chamber appears again and increases in size until it communicates with the wide channels of both sides of the chamber, creating low pressure, which draws melt into it, since pressure "valleys" of one pair coincide with pressure peaks in the up- and downstream neighbors, generating axial backflows. These expansions and contractions, like those
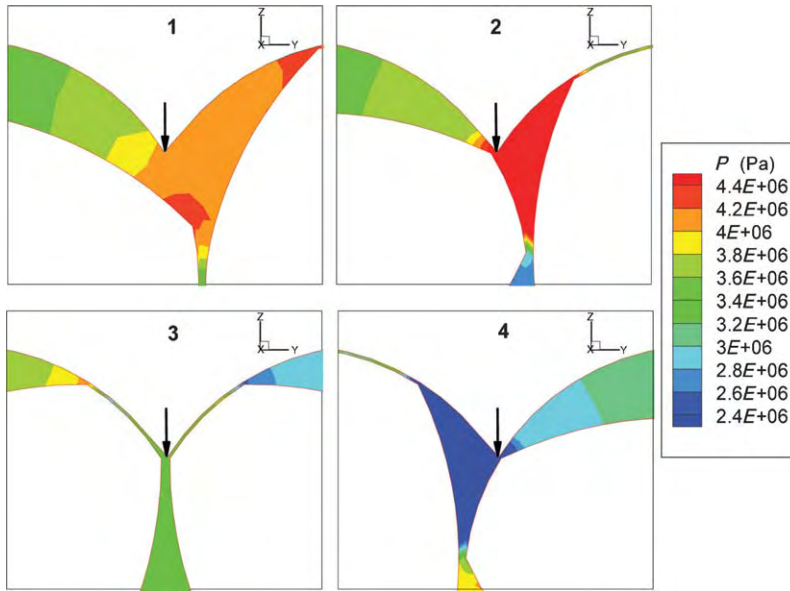
Fig. 10.68 The available expansion–contraction area in the apex region responsible for the dynamic pressure generated at the apex port. [Reprinted by permission from V. L. Bravo, A. N. Hrymak and J. D. Wright, ''Numerical Simulation of Pressure and Velocity Profiles in Kneading Elements of a Co-TSE,'' *Polym. Eng. Sci.*, **40**, 525–541 (2000).]

causing PED in kneading elements full of particulate solids, now cause effective distributive mixing. As with our PED discussion, the width of the kneading disks is expected to generate stronger backflows. Although the model predictions by Bravo et al. (111) are close to those experimentally obtained, the authors attribute these discrepancies to noninclusion of transient terms in their quasi-steady state three-dimensional FEM, and nonisothermicities present in the experiments give lower pressure drops. Furthermore, the neglect of extensional viscosities is also significant in view of the presence of strong compressive extensional flows.

In 2000 Ishikawa et al. (113) of the Funatsu group conducted three-dimensional FEM nonisothermal simulations for full Co-TSE kneading-and screw-element blocks, without making use of the quasi-steady state assumption. Their results were also compared with those obtained experimentally using a Japan Steel Works TEX 30 (30 mm) machine with 90° stagger angle, bilobal kneading disks. The polymer used was PP, whose rheological behavior fitted with a nonisothermal Carreau model. The pressure and temperature were measured at the circumferential and axial locations shown in Fig. 10.69. The pressure profile 90° away from the apex indicating converging–diverging plate-drag pressurization, shown in Fig. 10.70, is similar to the one obtained by Bravo et al., Fig. 10.67(b), but with better agreement between computed and experimental values, as is expected; nonisothermal and transient flow effects are included in this work. The pressure contours at the cross-sections A–A′, B–B′, and C–C′, with A–A′ being the upstream one, are depicted in Fig. 10.71 and are in line with the results in Fig. 10.70. Furthermore, the dP/dz axial pressure gradients change at a fixed circumferential position with the axial position. For example, in the region behind the upper right tip, the $(P|_{A-A'}P|_{B-B'})$ value is negative, while $(P|_{B-B'}P|_{C-C'})$ is positive. On the other hand, in front of the right tip, the
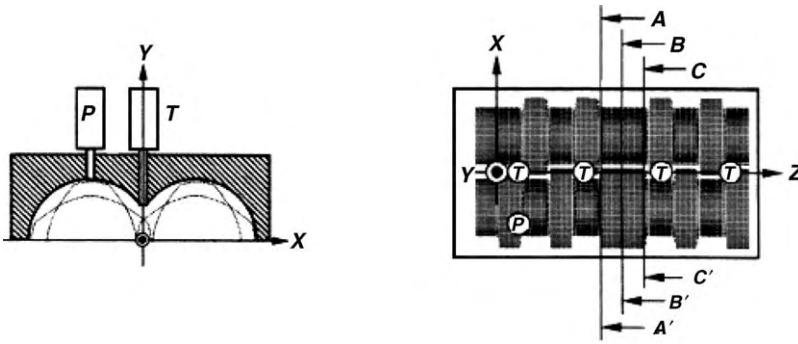
Fig. 10.69   Locations of the thermocouple and pressure transducers used by Ishikawa et al. (113). Numerical velocity, pressure, and temperature field at cross-sections A–A′, B–B′, and C–C′. [Reprinted by permission from T. Ishikawa, S. I. Kihara, and K. Funatsu, "3-D Numerical Simulations of Nonisothermal Flow in Co-Rotating Twin Screw Extruders," *Polym. Eng. Sci.*, **40**, 357 (2000).]

pressure gradient is positive between A–A′ and B–B′, while it is negative from B–B′ to C–C′. These pressure gradients attest to the presence at various circumferential locations of forward and backward axial flows, which are the hallmark of the screw-to-screw interactive effects, and are of large importance to rapid chaotic mixing. The circumferential velocities are an order of magnitude larger than the axial velocities. The directions of the calculated axial velocities correspond to the calculated pressure gradients, since axial flows are pressure driven. Typical temperature contours are shown in Fig. 10.72 at cross-section B–B′ obtained at 200 rpm. The calculated intermesh region values are the highest, higher than those in flight-gap regions. Nevertheless, the temperature field is rather flat, with a maximum
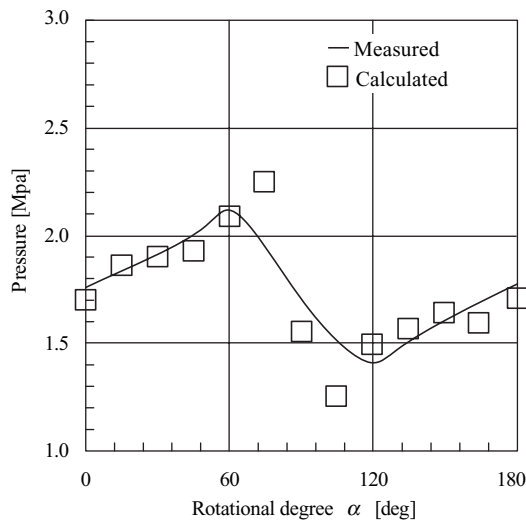

Fig. 10.70   Comparison between experimental and computational pressure profile results. [Reprinted by permission from T. Ishikawa, S. I. Kihara, and K. Funatsu, "3-D Numerical Simulations of Nonisothermal Flow in Co-Rotating Twin Screw Extruders," *Polym. Eng. Sci.*, **40**, 357 (2000).]
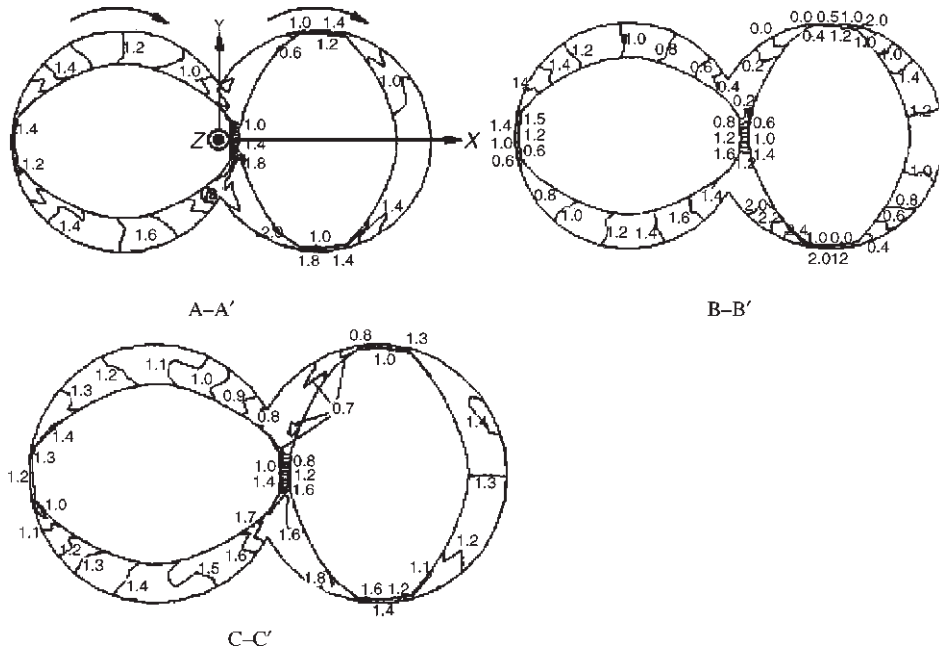
Fig. 10.71   Pressure contours computed at the three axial cross sections A–A′ (upstream), B-B′, and C-C′ (downstream). [Reprinted by permission from T. Ishikawa, S. I. Kihara, and K. Funatsu, "3-D Numerical Simulations of Nonisothermal Flow in Co-Rotating Twin Screw Extruders," *Polym. Eng. Sci.*, **40**, 357 (2000).]

temperature difference of 7°C. The total experimentally obtained axial difference, see Fig. 10.69, is only around 8–10°C. Non–isothermicities in the range of 20°C were measured and calculated for 400 rpm. Since 2000, Funatsu et al. have continued their extensive three-dimensional FEM simulations of nonisothermal flow of shear thinning, Carreau model polymer melts flowing in the following full channels, with screw geometrical and operational variables indicated in Table 10.9 (114).

Fig. 10.72   Temperature field at cross section obtained by Ishikawa at 200 rpm. [Reprinted by permission from T. Ishikawa, S. I. Kihara, and K. Funatsu, "3-D Numerical Simulations of Nonisothermal Flow in Co-Rotating Twin Screw Extruders," *Polym. Eng. Sci.*, **40**, 357 (2000).]
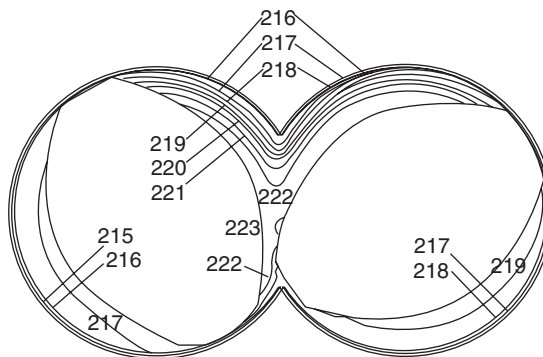
TABLE 10.9 Twin Rotor, Screw, and Kneading Element Configurations and Typical Dimensions and Operating Conditions Used for Full Channel Three-dimensional FEM Flow Analysis by Funatsu et al. (114)

Subjects	[Unit]	Full-Flighted Screw Elements				Mixing Elements				
		Single Flighted Rectangle		Self-cleaning		Rotors		Kneading Blocks		Shielding Disks (Blister rings)
		Counterrotating	Co-rotating	Single-flighted	Double-flighted	Discontinuous	Continuous	Two-tip	Three-tip	
Geometry Number		I	II III	IV	V	VI	VII	VIII	IX	X
Geometry										
Barrel radius	R_B [mm]	20.0	20.0	20.0	20.0~36.5	20.0		15.0~23.5	20.0	30.0~90.0
Flight radius	R_F [mm]	—	19.5	—	19.5~36.0	18.75~19.75		14.6~22.3	19.5	29.0~88.9
Screw root radius	R_S [mm]	15.0	15.0	10.0	12.5~23.5	12.5		10.5~23.0	16.0	18.0~55.0
Flight width (disk width)	W [mm]	10.0	2.0~5.3	0.8,2.7	—	4.15		7.8~10.0	10.0	11.0~33.0
Flight (tip) clearance	δ_s [mm]	10.0	0.2~3.5	—	—			0.4~0.7	0.5	1.0~1.7
Calender gap	δ_c [mm]	0.5	0.5~1.0	1.0	0.5~2.0	0.75		0.7~1.0	1.0	1.2~2.1
Pitch	P [mm]	40.0	11.0	10.0	30.0~56.0	—	40.0	45.0~50.0	50.0	—
Forward screw length	L_F [mm]	—	—	—	—	40.0		—	—	—
Backward screw length	L_B [mm]	—	—	—	—	40.0		—	—	—
Intermediate length	L_M [mm]	—	—	—	—	0.0	0.8	—	—	—
Disk gap	δ [mm]	—	—	—	—			0.1~1.5	0.1	1.0—4.5
Stagger angle	ψ [deg]	—	—	—	—			30~90	30~90	—
Rotational speed	N [rpm]	60.0	60.0	60.0	60.0~1300.0	60.0		60.0~1300.00	60.0	86.0~150.0

TABLE 10.10 Computational Capabilities (•) and Possible Simulations (○) of the Full Twin Rotor, Screw, and Kneading Element Channels of Funatsu et al. (114)

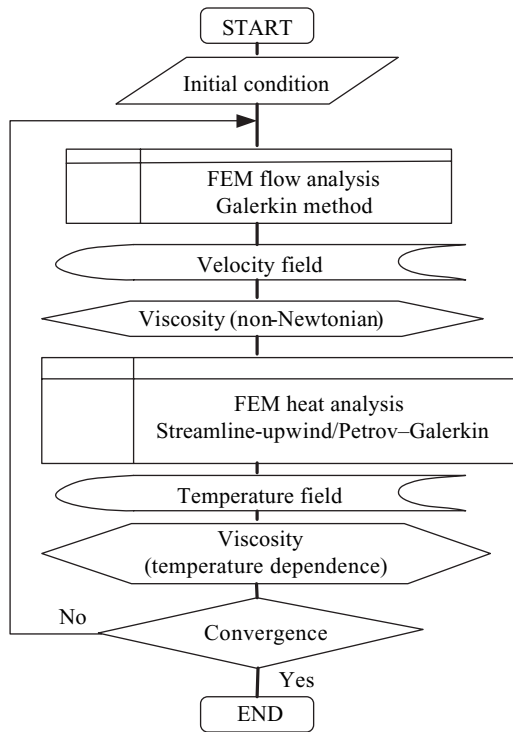| Twin-screw Element	Geometric Configurations	Velocity Distr.	Leakage Flows	Shear Stress Distr.	Pressure Drop	Residence Time Distr.	Marker Tracking Animation	Temperature Distr.	Reaction	Cited Refs
1 Single-flighted (SF)	Rectangular channel	•	•	•	•	•	○	○	○	(117)
	Self-cleaning	•	•	•	•	•	○	○	○	(118)
2 Double-flighted (DF)	Self-cleaning	•	•	•	•	•	•	○	○	(119)
3 Rotor	Continuous	•	•	•	•	○	○	•	○	(73)
	Discontinuous	•	•	•	•	○	○	○	○	
4 Kneading blocks (KB)	Two-tip Right-handed (R) stagger angle	•	•	•	•	•	•	•	•	
	Neutral (N) stagger angle	•	•	•	•	•	•	•	•	(113)
	Left-handed (L) stagger angle	•	•	•	•	•	•	•	•	
	Three-tip Right-handed (R) stagger angle	•	•	•	•	•	•	○	○	
	Neutral (N) stagger angle	•	•	•	•	•	•	○	○	(115)
	Left-handed (L) stagger angle	•	•	•	•	•	•	○	○	
5 Disk	Shielding disks (Blister rings)	•	•	•	•	•	•	○	○	(120)
	3 pitches (EA3-R, N, L) DF/R + KB/R + DF/R DF/R + KB/N + DF/R DF/R + KB/L + DF/R	•	•	•	•	•	•	•	○	In press
6 Element assembly (EA)	4 pitches (EA4-NL, LL, NR, LR) DF/R + KB/N + DF/L + DF/R DF/R + KB/L + DF/L + DF/R DF/R + KB/N + DF/R + DF/R DF/R + KB/L + DF/R + DF/R	•	•	•	•	•	•	○	○	(114)
	10 pitches (EA 10) 2DF/R + 3KB/R + 2KB/N + KB/L + 2DF/R	•	•	•	•	•	•	○	○	(121)

Fig. 10.73 Schematic of the three-dimensional FEM nonisothermal flow analysis flow diagram employed by the Ishikawa et al. (113). [Reprinted by permission from T. Ishikawa, S. I. Kihara and K. Funatsu, "3-D Numerical Simulations of Nonisothermal Flow in Co-Rotating Twin Screw Extruders," *Polym. Eng. Sci.*, **40**, 365 (2000).]

The computational capabilities of the Funatsu et al. modeling are listed in Table 10.10 with reference to the publication reporting their computational work. Some of the following are evident from the Tables 10.9 and 10.10. All common twin-rotor polymer processing equipment and screw-, rotor-, or kneading-element types, as well as element sequences have been treated:

1. Much computational effort has been devoted to the *full-channel* Co-TSE kneading-element and element sequences.

2. The majority of simulations deal with *isothermal* flows, though the computational format of this computational group is shown in Fig. 10.73.

3. There is more attention paid to examining the *distributive mixing* abilities of each of the full-channel geometries examined, through marker tracking computational animation (114–116).

4. Finally, reactive processing in full nonisothermal, twin-rotor channel flows has not been solved for all but full bilobal kneading-disk sequences and screw-mixing elements (SME) (116).

It is certain that, in the near future, as is partially true at present, polymer processing engineers who are involved in the design of twin-rotor processing equipment and process

results analysis will be aided by CFM simulation packages, which will shed light on the melt mixing and reactive processing capabilities of such equipment

REFERENCES

1. J. L. White, *Twin Screw Extrusion*, Hanser, Munich, 1990.

2. K. Eise, H. Herrmann, S. Jakopin, U. Burkhardt, and H. Werner, "An Analysis of Twin Screw Extruder Mechanisms," *Adv. Polym. Tech.*, **1** (2), 18–39 (1981).

3. D. B. Todd, "Introduction to Compounding," in *Plastics Compounding–Equipment and Processing*, D. B. Todd, Ed., Hanser, Munich, 1998.

4. R. C. Kowalski, "Case Histories of Industrial Studies of Extruder Reactions," in *Reactive Extrusion, Principles and Practices*, M. Xanthos, Ed., Hanser, Munich, 1992.

5. Z. Tadmor and C. G. Gogos, *Principles of Polymer Processing*, Wiley-Interscience, New York, 1979, Chapter 10.

6. D. Smith, P. Stoughton, C. Morgan, and G. Hovis, in *The SPE Guide on Extrusion Technology and Troubleshooting*, J. Vlachopoulos and J. R. Wagner, Jr., SPE, Danbury, CT, 2001, Chapter 5.

7. W. C. Thiele, "Counter-rotating Intermeshing Twin Screw Extruders," in *Plastics Compounding– Equipment and Processing*, D. B. Todd, Ed., Hanser, Munich, 1998.

8. E. H. Ahlefeld, A. J. Baldwin, P. Hold, W. A. Rapetski, and H. R. Scharer, U.S. Patent 3,154,808 (1964); U.S. Patent 3,239,878.

9. E. L. Canedo and L. N. Valsamis, "Selecting Compounding Equipment Based on Process Considerations," *Int. Polym. Process.*, **9**, 225 (1994); in *Plastics Compounding–Equipment and Processing*, D. B. Todd, Ed., Hanser, Munich, 1998.

10. R. Erdmenger, German Patent 813,154 (1951); U. S. Patent 2,670,188 (1954).

11. P. G. Andersen, "The Werner and Pfleiderer Twin-Screw Corotating Extruder System," in *Plastics Compounding—Equipment and Processing*, D. B. Todd, Ed., Hanser, Munich, 1998.

12. D. B. Todd, "Compounding in Twin Screw Extruders," in *Two-phase Polymer Systems*, L. A. Utracki, Ed., Hanser, Munich, 1991.

13. D. B. Todd, U.S. Patent 4,136,968 to Baker Perkins (1979); also, D. B. Todd, "Energy Dissipated in Twin Screw Extruders," *SPE ANTEC Tech. Papers*, **26**, 220 (1980).

14. H. Herrmann, H. J. Nettelnbrecker, and A. Dreiblatt, "Quality Assurance and Improvement in On-line Controlled Compounding," *SPE ANTEC Tech. Papers*, **33**, 157 (1987).

15. D. B. Todd, "Drag and Pressure Flow in Twin Screw Extruders," *SPE ANTEC Tech. Papers*, **35**, 168 (1989); also, D. B. Todd, "Drag and Pressure Flow in Twin Screw Extruders," *Int. Polym. Process.*, **6**, 143 (1991).

16. K. Funatsu, S.-I. Kihara, M. Miyazaki, S. Katsuki, and T. Kajiguara, "3-D Numerical Analysis on the Mixing Performance for Assemblies with Filled Zone of Right-handed and Left-handed Double-flighted Screws and Kneading Blocks in Twin-screw Extruders," *Polym. Eng. Sci.*, **42**, 707–723 (2002).

17. C. G. Gogos, Z. Tadmor, and M.-H. Kim, "Melting Phenomena and Mechanisms in Polymer Processing Equipment," *Adv. Polym. Technol.*, **17,** 285–305 (1998).

18. B. Qian, D. B. Todd, and C. G. Gogos, "Plastic Energy Dissipation and its Role on Heating/ Melting of Single-component Polymers and Multi-component Polymer Blends," *Adv. Polym. Technol.*, **22**, 85–95 (2003).

19. U. Sundararaj and C. W. Macosko, R. J. Rolando, and H. T. Chan, "Morphology Development in Polymer Blends," *Polym. Eng. Sci.*, **32**, 1814–1832 (1992).

20. S. Bawiskar and J. L. White, ''Melting Model for Modular Self Wiping Co-rotating Twin Screw Extruders,'' *Polym. Eng. Sci.*, **38**, 727–740 (1998).

21. B. Vergnes, G. Souveton, M. L. Delacour, and A. Ainser, ''Experimental and Theoretical Study of Polymer Melting in a Co-rotating Twin Screw Extruder,'' *Int. Polym. Process.*, **16**, 351–362 (2001).

22. D. M. Anderson, G. B. McFadden, and A. A. Wheeler, ''Diffuse-interface Methods in Fluid Mechanics,'' *Annu. Rev. Fluid Mech.*, **30**, 139 (1998).

23. P. D. Anderson, O. S. Galaktionov, G. W. M. Peters, F. N. Van de Vosse, and H. E. H. Meijer, ''Mixing of Non-Newtonian Fluids in Time-periodic Cavity Flows ,'' *J. Non-Newtonian Fluid Mech.*, **93**, 265–280 (2000).

24. L. P. B. M. Janssen, *Twin Screw Extrusion*, Elsevier Scientific, Amsterdam, 1978.

25. S. Lim and J. L. White, ''Flow Mechanisms, Material Distribution and Phase Morphology Development in a Modular Intermeshing Counterrotating Twin Screw Extruder of Leistritz Design,'' *Int. Polym. Process.*, **9**, 33–45 (1994).

26. J. W. Cho and J. L. White, ''Melting and Blending in a Modular Corotating/Counter-rotating Twin Screw Extruder,'' *Int. Polym. Process.*, **11**, 21–28 (1996).

27. K. Wilczynski and J. L. White, ''Experimental Study of Melting in an Intermeshing Counter-Rotation Twin Screw,'' *Int. Polym. Process.*, **16**, 257–262 (2001).

28. L. P. B. M. Janssen and J. M. Smith, *Kunststoffe*, **66**, 724 (1976).

29. A. J. van der Goot, O. Poorter, and L. P. B. M. Janssen, ''Determination of the Degree of Fill in a Counterrotating Twin Screw Extruder,'' *Polym. Eng. Sci.*, **38**, 1193–1198 (1998).

30. J. A. Speur, H. Mavridis, J. Vlachopoulos, and L. P. B. M. Janssen, ''Flow Patterns in the Calender Gap of a Counterrotating Twin Screw Extruder,'' *Adv. Polym. Technol.*, **7**, 39–48 (1987).

31. T. Li and I. Manas-Zloczower, ''A Study of Distributive Mixing in Counter-rotating Twin Screw Extruders,'' *Int. Polym. Process.*, **10**, 314–320 (1995).

32. T. Katziguara, Y. Nagashima, Y. Nakano, and K. Funatsu, ''Numerical Study of Twin-screw Extruders by Three-dimensional Flow Analysis–Development of Analysis Technique and Evaluation of Mixing Performance for Full Flight Screws,'' *Polym. Eng. Sci.*, **36**, 2142–2152 (1996).

33. T. Sakai and N. Hashimoto, ''Application of Novel Counter-rotating Intermeshed Twin Extruder for Degassing Operation,'' *SPE ANTEC Tech. Papers*, **32**, 860–863 (1986); also T. Sakai, N. Hashimoto, and N. Kobayashi, ''Experimental Comparison between Counter-rotation and Co-rotation on the Twin Screw Extrusion Performance,'' *SPE ANTEC Tech. Papers*, **33**, 146–151 (1987).

34. S. K. Dey and J. A. Biesenberger, ''Reactive Extrusion of Methyl Methacrylate,'' *SPE ANTEC Tech. Papers*, **33**, 133 (1987).

35. K. J. Gadzenveld and L. P. B. M. Janssen, ''Scale-up of Counter-rotating Closely Intermeshing Twin Screw Extruders without and with Reactions,'' *Polym. Eng. Sci.*, **30**, 1529–1536 (1990).

36. K. J. Gadzenveld and L. P. B. M. Janssen, ''A Mixing Model for Multicomponent Reactions in Twin Screw Extruders Applied to the Polymerization of Urethanes,'' *Polym. Eng. Sci.*, **32**, 457–466 (1992).

37. K. J. Gadzenveld and L. P. B. M. Janssen, ''The Grafting of Maleic Anhydride on High Density Polyethylene in an Extruder,'' *Polym. Eng. Sci.*, **32**, 467–474 (1992).

38. K. J. Gadzenveld and L. P. B. M. Janssen, ''Twin Screw Extruders as Polymerization Reactors for a Free Radical Homo Polymerization,'' *Can. J. Chem. Eng.*, **71**, 411–418 (1993).

39. K. J. Gadzenveld, J. E. Capel, D. J. van der Wal, and L. P. B. M. Janssen, ''The Modeling of Counterrotating Twin Screw Extruders as Reactors for Single-component Reactions,'' *Chem. Eng. Sci.*, **49**, 1639–1649 (1994).

40. H. A. Jongbloed, R. K. S. Mulder and L. P. B. M. Janssen, "The Co-polymerization of Methacrylates in a Counterrotating Twin Screw Extruder," *Polym. Eng. Sci.*, **35**, 588 (1995).

41. J. A. Speur, Ph.D. Thesis, Department of Chemical Engineering, University of Groningen, Groningen, The Netherlands, 1988.

42. N. P. Stuber, Ph.D. Thesis, Department of Chemical Engineering, University of Minnesota, Minneapolis 1986.

43. E. Trommsdorff, H. Holle, and P. Lagally, *Macromol. Chem.*, **1**, 280 (1947).

44. F. L. Marten and A. E. Hamielec, "High Conversion Diffusion-controlled Polymerization," *ACS SYMP. SER.*, (10), 34–70 (1979).

45. K. J. Gadzenvelt, Ph.D. Thesis, Department of Chemical Engineering, University of Groningen, Groningen, The Netherlands, 1992.

46. L. J. Fuller, U.S. Patent 2,441,222 (1948).

47. L. J. Fuller, U.S. Patent 2,615,199 (1952).

48. L. F. Street, U.S. Patent 2,733,051 (1956).

49. L. F. Street, U.S. Patent 3,078,511 (1963).

50. R. H. Skidmore, U.S. Patent 3,985,348 (1976).

51. R. J. Nichols and F. Kher-adi, "Melting in CRT Twin Screw Extruders," *Mod. Plast*, **16** (2), 70 (1984).

52. S. Satija and C. S. Tucker, "Effect of Screw Root Profile on PMMA Melting in Counter-rotating Non-intermeshing Twin Screw Extruder," *SPE ANTEC Tech. Papers*, **40**, 248–255 (1994).

53. A. Kaplan and Z. Tadmor, "Theoretical Model for Non-intermeshing Twin Screw Extruders," *Polym. Eng. Sci.*, **14**, 58–66 (1974).

54. R. J. Nichols, "Pumping Characteristics of Counterrotating Tangential Twin Screw Extruders," *SPE ANTEC Tech. Papers*, **29**, 130–133 (1983).

55. R. J. Nichols, "Modeling Performance Characteristics of Counterrotating Tangential Twin Screw Extruders," *SPE ANTEC Tech. Papers*, **30**, 6–9 (1984).

56. K. Nguyen and J. Lindt, "Finite Element Modeling of a Counterrotating, Non-intermeshing Twin Screw Extruder," *Polym. Eng. Sci.*, **29**, 709–714 (1989).

57. D. S. Bang, M. H. Hong, and J. L. White, "Modular Tangential Counterrotating Twin Screw Extrusion: Determination of Screw Pumping Characteristics of Modules and Composite Machine Behavior," *Polym. Eng. Sci.*, **38**, 485–498 (1998).

58. C. Martin, "Counterrotating Twin Screw Extruders", in *Extrusion Toolbox*, Society of Plastics Engineers, Danbury, CT, (2004).

59. L. N. Valsamis and E. L. Canedo, "Mixing in the Continuous Farrel Mixer," in *Mixing and Compounding of Polymers*, I. Manas-Zloczower and Z. Tadmor, Eds., Hanser, Munich (1994).

60. L. N. Valsamis and E. L. Canedo, "Effect of Rotor Geometry and Operating Conditions on Mixing Performance in Continuous Mixers: An Experimental Study," *SPE ANTEC Tech. Papers*, **37**, 629–632 (1991).

61. W. R. Bolen and R. E. Colwell, *SPE J.*, **14** (3), 24 (1958).

62. J. T. Bergen, "Mixing and Dispersive Processes," in *Processing of Thermoplastic Materials*, E. C. Bernhardt, Ed., Reinhold, New York (1959).

63. K. Meissner and E. O. Reher, *Plaste Kautsch.*, **26**, 272 (1979).

64. K. Meissner, J, Bergmann, and E. O. Reher, *Plaste Kautsch.*, **27**, 147 (1980).

65. U. Wagenknecht, K. Meissner, E. O. Reher, and B. Polsterdorf, *Plaste Kautch.*, **35**, 175 (1988).

66. M. H. Kim and J. L.White, ''Simulation of Flow in a Farrel Continuous Mixer,'' *Int. Polym. Process.*, **7**, 15–19 (1992).

67. J. J. Cheng and I. Masas-Zloczower, ''Hydrodynamic Analysis of a Banbury Mixer 2-D Flow Simulations for the Entire Mixing Chamber,'' *Polym. Eng. Sci.*, **29**, 1059–1065 (1989).

68. J. J. Cheng and I. Manas-Zloczower, ''Flow Field Characterization in a Banbury Mixer,'' *Int. Polym. Process.*, **5**, 178–183 (1990).

69. T. W. Wong and I. Manas-Zloczower, ''Numerical Studies of the Flow Field in Partially Filled Mixing Equipment,'' *SPE ANTEC Tech. Papers*, **38**, 1788–1793 (1992).

70. E. L. Canedo and L. N. Valsamis, ''Non-Newtonian, Non-isothermal Flow between Non-parallel Plates in Relative Motion. Applications to Mixer Design,'' *SPE ANTEC Tech. Papers*, **36**, 164–167 (1990).

71. R. B. Bird, R. C. Armstrong, and O. Hassager, *Dynamics of Polymeric Liquids*, Vol. 1, *Fluid Mechanics*, Second Edition, Wiley, New York, 1987.

72. C. H. Yao and I. Manas-Zloczower, ''Influence of Design on Dispersive Mixing Performance in an Axial Discharge Continuous Mixer–LCMAX 40,'' *Polym. Eng. Sci.*, **38**, 936–946 (1998).

73. T. Ishikawa, S. Kihara, K. Funatsu, T. Amaiwa, and K. Yano, ''3-D Numerical Simulations and Nonisothermal Flow in Co-rotating Twin Screw Extruders,'' *Polym. Eng. Sci.*, **40**, 357–364 (2000).

74. P. G. Andersen, ''Mixing Practices in Co-rotating Twin Screw Extruders,'' in *Mixing and Compounding of Polymers*, I. Manas-Zloczower and Z. Tadmor, Eds., Hanser, Munich (1994).

75. P. G. Andersen, ''The Werner and Pfleiderer Twin Screw Co-rotating Extruder System,'' in *Plastics Compounding*, D. B. Todd, Ed., Hanser, Munich (1998).

76. T. Sakai, ''Intermeshing Twin Screw Extruders,'' in *Mixing and Compounding of Polymers*, I. Manas-Zloczower and Z. Tadmor, Eds., Hanser, Munich (1994).

77. T. Sakai, ''Intermeshed TEX Twin Screw Extruder: JSW Compounding System,'' in *Plastics Compounding*, D. B. Todd, Ed., Hanser, Munich (1998).

78. D. B. Todd, ''APV (Baker Perkins) Systems,'' in *Plastics Compounding*, D. B. Todd, Ed., Hanser, Munich (1998).

79. M. Mack, ''Co-rotating Intermeshing Twin Screw Extruder: Berstorff's System,'' in *Plastics Compounding*, D. B. Todd, Ed., Hanser, Munich (1998).

80. P. Heidemeyer, German Patent Application 195,36289.6 (1995).

81. R. Potluri, D. B. Todd, and C. G. Gogos, *Proc. 11th Polymer Mixing Study Semi-annual Meeting*, Polymer Processing Institute, Hoboken, NJ (1995).

82. M. H. Kim, Ph.D. Dissertation, Department of Chemical Engineering, Stevens Institute of Technology, Hoboken, NJ (1999).

83. B. Qian and C. G. Gogos, ''The Importance of Plastic Energy Dissipation (PED) to the Heating and Melting of Polymer Particulates in Intermeshing Co-rotating Twin Screw Extruders,'' *Adv. Polym. Tech.*, **19**, 287–299 (2000).

84. C. G. Gogos, B. Qian, D. B. Todd, and M. H. Kim, ''A Predictive Melting Model for Polymer Particulates in Co-rotating Twin Screw Extruders,'' *SPE ANTEC Tech. Papers*, **47**, 134–138 (2001).

85. M. H. Kim and C. G. Gogos, ''Melting Phenomena and Mechanism in Co-rotating Twin Screw Extruder,'' *SPE ANTEC Tech. Papers*, **47**, 145–149 (2001).

86. C. G. Gogos and B. Qian, ''Plastic Energy Dissipation during Compressive Deformation of Individual Polymer Pellets and Polymer Particulate Assemblies,'' *Adv. Polym. Tech.*, **21**, 287–298 (2002).

87. M. D. Wetzel, C. K. Shih, D. A. Denelsbek, and S. L. Latimer, ''Quantification of Melting using the Pulse Perturbation Technique, Part I,'' *SPE ANTEC Tech. Papers*, **51**, 347 (2005).

88. M. D. Wetzel, C. K. Shih, D. A. Denelsbek, and S. L. Latimer, ''Quantification of Melting using the Pulse Perturbation Technique Part II,'' *SPE ANTEC Tech. Papers*, **51**, 354 (2005).

89. H. Potente and U. Melish, ''Theoretical and Experimental Investigations of the Melting of Pellets in Co-rotating Twin Screw Extruders,'' *Int. Polym. Process.*, **11**, 101 (1996).

90. S. Bawiskar and J. L. White, ''A Composite Model for Solid Conveying, Melting, Pressure and Fill Factor Profiles in Modular Co-rotating Twin Screw Extruders,'' *Int. Polym. Process.*, **12**, 331 (1997).

91. S. Bawiskar and J. L. White, ''Melting Model for Modular Self Wiping Co-rotating Twin Screw Extruders,'' *Polym. Eng. Sci.*, **38**, 727–740 (1998).

92. L. Zhu, K. A. Nahr, and X. Geng, ''Modeling of Particle-dispersed Melting Mechanism and Its Application in Corotating Twin Screw Extrusion,'' *J. Polym. Sci. Part B: Polym. Phys.*, **39**, 2461–2468 (2001).

93. B. Vergnes, G. Souveton, M. L. Deacour, and A. Ainser, ''Experimental and Theoretical Study of Polymer Melting in a Co-rotating Twin Screw Extruder,'' *Int. Polym. Process.*, **16**, 351–362 (2001).

94. J. Mewis and C. W. Macosko, *Rheology: Principles, Measurements and Applications*, C. W. Macosko, Ed. Wiley, New York (1994).

95. P. J. Carreau, D. C. R. DeKee, and R. P. Chabra, *Rheology of Polymeric Systems: Principles and Applications*, Hanser, Munich (1997).

96. I. M. Krieger and T. J. Dougherty, ''A Mechanism for Non-Newtonian Flow in Suspensions of Rigid Spheres,'' *Trans. Soc. Rheol.*, **3**, 137–152 (1959).

97. R. Roscoe, in *Flow Properties of Dispersed Systems*, J. J. Hermans, Ed., Interscience, New York (1953).

98. H. Werner, Ph.D. Thesis, University of Munich, Munich, Germany (1976).

99. H. Jung and J. L. White, ''Investigation of Melting Phenomena in Modular Co-rotating Twin Screw Extrusion,'' *Int. Polym. Process.*, **18**, 127–132 (2003).

100. C. Truesdell and R. A. Tupin, ''The Classical Field Theories,'' in *Handuch der Physik*, Springer-Verlag, Berlin (1960).

101. D. B. Todd, ''Drag and Pressure Flow in Twin Screw Extruders,'' *Int. Polym. Process.*, **6**, 143–147 (1991).

102. A. D. Gotsis, Z. Ji, and D. M. Kalyon, ''3-D Analysis of the Flow in Co-rotating Twin Screw Extruders,'' *SPE ANTEC Tech. Papers*, **36**, 139–142 (1990).

103. A. Lawal and D. M. Kalyon, ''Mechanisms of Mixing in Single and Co-rotating Twin Screw Extruders,'' *Polym. Eng. Sci.*, **35**, 1325–1338 (1995).

104. Y. Wang, J. L. White, and W. Szydlowski, ''Flow in a Modular Intermeshing Co-rotating Twin Screw Extruder,'' *Int. Polym. Process.*, **4**, 262–269 (1989).

105. A. Kiani and H. J. Samann, ''The Influence of Curvature on the Simulation of Flow in a Tangential Counter-rotating Twin Screw Extruder,'' *SPE ANTEC Tech. Papers*, **39**, 2758 (1993).

106. A. Kiani, P. Heidemeyer, and R. Pallas, ''Study of Flow and RTD in a ZSK Twin Screw Extruder,'' *SPE ANTEC Tech. Papers*, **43**, 94–99 (1997).

107. H. H. Yang, Ph.D. Thesis, Chemical Engineering Department, Case-Western Reserve University, Cleveland (1993).

108. J. J. Cheng and I. Manas-Zloczower, ''Hydrodynamic Analysis of a Banbury Mixer 2-D Flow Simulations for the Entire Mixing Chamber,'' *Polym. Eng. Sci.*, **29**, 1059–1065 (1989).

109. T. W. McCullough and B. T. Hilton, ''The Extrusion Performance of Co-rotating, Intermeshing Twin Screw Extruder Screw Elements–An Experimental Investigation,'' *SPE ANTEC Tech. Papers*, **39**, 3372–3379 (1993).

110. J. P. Christiano and M. Lindenfelzer, "Investigation of Mixing Patterns in Co-rotating Fully Intermeshing Twin Screw Extruders Mixing Elements Using Dynamic Pressure Distributions," *SPE ANTEC Tech. Papers*, **43**, 78–83 (1997).

111. V. L. Bravo, A. N. Hrymak, and J. D. Wright, "Numerical Simulation of Pressure and Velocity Profiles in Kneading Elements of a Co-rotating Twin Screw Extruder," *Polym. Eng. Sci.*, **40**, 525–541 (2000).

112. S. A. Jaffer, V. L. Bravo, P. E. Wood, A. N. Hrymak, and J. D. Wright, "Experimental Validation of Numerical Simulations of the Kneading Disc Section in a Twin Screw Extruder," *Polym. Eng. Sci.*, **40**, 892–901 (2000).

113. T. Ishikawa, S. I. Kihara, and K. Funatsu, "3-D Numerical Simulations of Nonisothermal Flow in Co-rotating Twin Screw Extruders," *Polym. Eng. Sci.*, **40**, 357–364 (2000).

114. K. Funatsu, S. I. Kihara, M. Miyazaki, S. Katsuki, and T. Kajiwara, "3-D Numerical Analysis on the Mixing Performance for Assemblies with Filled Zone of Right-handed and Left-handed Double-flighted Screws and Kneading Blocks in Twin Screw Extruders," *Polym. Eng. Sci.*, **42**, 707–723 (2002).

115. M. Yoshinaga, S. Katsuki, M. Miyazaki, L. Liu, S. I. Kihara and K. Funatsu, "Mixing Mechanism of Three-tip Kneading Block in Twin Screw Extruders," *Polym. Eng. Sci.*, **40**, 168–178 (2000).

116. T. Ishikawa, T. Amano, S. I. Kihara, and K. Funatsu, "Flow Patterns and Mixing Mechanisms in the Screw Mixing Element of a Corotating Twin-screw Extruder," *Polym. Eng. Sci.*, **42**, 925–939 (2002).

117. T. Kajiwara, Y. Nagashima, Y. Nakano, and K. Funatsu, "Numerical Study of Twin-screw Extruders by Three-dimensional Flow Analysis–development of Analysis Technique and Evaluation of Mixing Performance for Full Flight Screws," *Polym. Eng. Sci.*, **36**, 2142–2152 (1996).

118. L. Liu, H. Higashi, Y. Nagashima, T. Kajiwara, and K. Funatsu, *Seikei-Kakou*, **9**, 169 (1997).

119. L. Liu, M. Yoshinaga, S. Kihara, and K. Funatsu, *Seikei-Kakou*, **11**, 250 (1999).

120. M. Miyazaki, M. Yamaura, T. Takayama, S. Kihara, and K. Funatsu, "3-D Flow Simulation of Shielding Disk in Twin Screw Extruders," *Proc. 16th Ann. Meet. Polym. Process. Soc.*, Shanghai, China, 2000, pp. 268–269.

121. K. Funatsu, S. Katsuki, and S. Kihara, *J. Soc. Chem. Eng.*, *31st Ann. Meet.*, Vol. II, (in Japanese) Yonezawa, Japan, 1998, p. 272.

PROBLEMS

10.1 *Engineering Estimates of the Drag- and Pressure-Flow Terms of the "Screw Characteristic Lines" of Co-TSE Conveying Screws and Kneading Elements* Todd[*] presents the calculated values of the A_t and B_t geometric parameters for conveying screw and kneading elements of Co-TSEs needed for engineering estimates of "screw characteristic lines," Eq. 10.3-13, also listed on Table 10.8

$$Q = A_t N - B_t \Delta P / \eta L$$

Examine the assumptions, carry out two sample calculations, one for kneading- and another for conveying-screw elements, and discuss the range of applicability and limitations of these engineering estimates.

---

[*] D. B. Todd, "Drag and Pressure Flow in Twin Screw Extruders," *Int. Polym. Process.*, **6**, 143 (1991).

10.2 *Comparison of Melting Rates of Polypropylene in Single and Twin Screw Extruders*   Polypropylene was melted in both a single- and a co-rotating intermeshing twin-screw extruder. The experimental conditions and the results analysis of the carcasses by screw pulling to determine the axial lengths in which melting takes place are as follows:

(a) SSE: 2.5-in D, square pitch, 26.5 *L/D* with 12.5 turns of feed section 0.37 in deep, a 9.5-turn transition section, and a 4.5-turn metering section 0.127 in deep. Melting was carried out at 96.8 lb/h at 60 rpm with $T_{barrel} = 450°$ F and a die pressure of 3000 psi. The melting process starts at turn 7 and ends at turn 24 (see Fig. 9.21).

(b) TSE: 30-mm D, $D_o - D_i = 4.7$ mm, $L_{lobe} = 8.4$ mm operating at 10 kg/h, 60 rpm, and $T_{barrel} = 140°$C. The observed melting length was approximately $4 \times L_{lobe} \sim 30 - 35$ mm; second row of Table 10.7.

(1) Calculate the time it takes to melt PP in both the single- and twin-screw extruders, under the condition, indicated.

(2) Based on the observed total number of lobes needed for melting of PP under the conditions stated in part (b), what is the total number of compressions needed for complete melting of PP?

(3) Comment on the difference between the estimated and observed number of lobes, 6 vs. 4 for Exp 4, Table 10.7, second row of Table 10.7.

10.3 *PED-Based Melting Estimates in a ZSK-30 and a ZSK 300*   The PED-based melting model was discussed in Section 10.3. The model was used by Qian and Gogos to calculate the melting capabilities, under typical operating conditions, of two Coperion Co-TSEs: the laboratory-scale 30-mm ZSK 30 and the large production-scale ZSK-300 (Fig. 10.56). Their results appear on the following table:

Number of Compacted Particulate Compressions Occurring during the Passage over a 1(*L/D*) Kneading Block

	ZSK-30	ZSK-300
Barrel diameter (*D*, mm)	30	300
Channel depth (*H*, mm)	4.7	40.75
Mass flow rate (kg/h)	20	35,000
Bulk density (g/cm^3)	1	1
Screw speed (rpm)	300	300
Average $t_{transit}$ to go over one (*L/D*) (s)	2.3	1.2
Number of rotations per one (*L/D*) transit	11.7	5.8
Number of compressions per one (*L/D*) transit	15.7	7.7

(a) Verify the results of these calculations using Eqs. 10.3-1 to 10.3-5. (b) In which of the two Co-TSEs is the assumption that melting arises totally from PED and not conductive melting from the barrel? (c) Specify the operating conditions at which the ZSK-30 must be operated, for the melting results to be scalable to the 300 Megacompounder. (d) Does the PED model provide an explanation for the extraordinary melting capabilities of the 300 Megacompounder for melting such

high throughput of PE within the 10–20 of residence time? Estimate whether VED alone can provide enough mechanical energy dissipation to enable this melting rate.

10.4 *Throughput Rate Calculations for a Solids Single Screw Feeder Feeding a Co-TSE*   A single-screw feeder is used for controlled feed rate of a 30-mm Co-TSE. The experimentally obtained feed rates with LDPE pellets at different screw speeds are give in the following table:

Screw Speed (rpm)	Throughput (kg/h)
9.27	3.80
19.44	7.60
48	18.76
96	37.51
144	56.72
192	75.02
207	80.89

Calculate the feeding screw throughput rate capacity assuming plug-flow and LDPE pellet bulk density of 0.45 g/cc. The geometrical variables of the feeder screw are: barrel diameter, $D_1 = 1.66$ in; screw root diameter, $D_2 = 0.325$ in; and lead, $L = 1.2$ in. Examine and discuss the difference between the observed and calculated throughput rate feeder capabilities, as it relates to the "plug" velocity assumption.

10.5 *Estimation of the Order of Magnitude of the FED Generated during a Single Pass of a Compacted Particulate Solid Bed over the Rotor Wing-Tip Clearance of a CM*   In Example 10.1, the *local* interparticle mechanical power dissipated into heat $\dot{W}_{\text{FED}}$ (watts) by FED during the passage of a compressed polymer particulates bed over the rotor wing-tip clearance region, is estimated by Eq. E10.1-2

$$\dot{W}_{\text{FED}} \sim \pi D_{\text{max}} N (d_p/h) f \cdot F_N$$

where $D_{\text{max}} = 300$ mm; $h = 7.5$ mm; wing-tip width $w = 25$ mm; particulate size $d_p = 300$ microns; $f = 0.5$; and a barrel transducer pressure recording during the passage of the rotor wing tip of $P = 10^7$ Pa. Calculate the FED power dissipated per unit during a single pass over the wing tip just downstream the feed section of the FCM, Fig. 10.6(b)

10.6 *VED-Based Estimate of the Mixing Zone Power Requirements of a CM*   Engineering estimates of the power requirement for the mixing section of CMs are difficult to make, even with 3D FEM fluid mechanical models, because CMs operate partially full, a physical state with free boundaries, which cannot be handled by such simulations. Thus, often such estimates are based on the power consumed during the flow of the polymer melt in the wing-tip region, making a parallel-plate approximation. The rationale behind this estimate is the realization that this region creates the highest shear-rate flows, due to the small clearance h between the rotor lip and the barrel. Calculate (a) the mechanical energy dissipated per pass per unit wing-tip length for a polyethylene melt with effective Newtonian viscosity

$\mu_{eff} = 300$ Pa·s flowing in isothermal flow in the wing-tip region of $h = 7.5$ mm, $W = 25$ mm, $D_{max} = 300$ mm at a rotor speed $N = 300$ rpm.

10.7 ***Effects of the Co-TSE Kneading-Disk Sequence Stagger Angle and Disk Width on Melt Distributive and Dispersive Mixing***   Andersen (75) presents the effects of the stagger angle in a sequence of forwarding kneading disks, as well as the effect of their width using the two schematic representations in the accompanying figure.
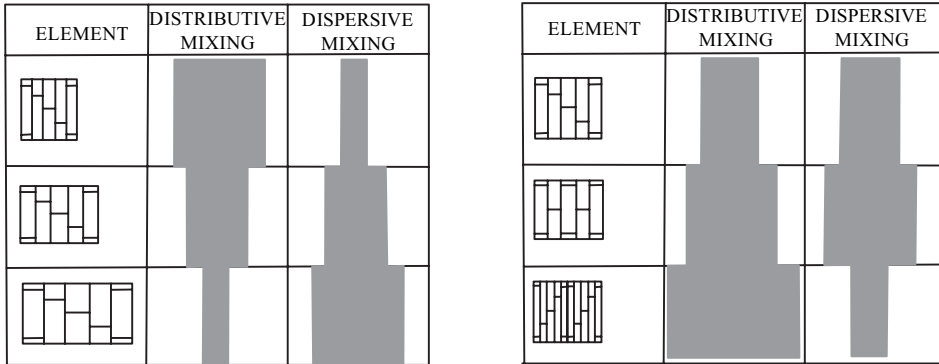
Effect of disk width on
distributive mixing

Effect of disk sequence stagger on
distributive and dispersive mixing

Discuss the validity and usefulness of the preceding qualitative figures in terms of Fig. 10.11 and this chapter's discussion on melt flow, pressurization and chaotic mixing in Co-TSEs.

10.8 ***Vent-Port Staging Analysis of a 42% polychloroprene – 58% CCl₄ Undergoing Devolatilization in a JSW TEX 65 Counter-TSE***   Examine the experimental results obtained by Sakai et al. (33), shown on Fig. 10.27 in terms of equilibrium stage analysis. The results indicate that the incoming 58% CCl₄ stream concentration is reduced to just above 7000 ppm after the second vent port downstream of the feed port. What does vent port equilibrium analysis?

(a) What does equilibrium stage analysis preset for this system?

(b) Are there any problems associated with the fact that the feed stream in a rubber slurring with a high CCl₄ concentration of 58%, requiring high amounts of CCl₄ to be removed in the first stage?